Structural, Electronic and Switching Properties of Metalloporphyrin Molecules on Metal Surfaces

A Combined STM and AFM Study

Xianwen Chen

Im Fachbereich Physik
der Freien Universität Berlin
eingereichte Dissertation

08.10.2015

Diese Arbeit entstand in der Arbeitsgruppe von Prof. Dr. Katharina J. Franke am Fachbereich Physik der Freien Universität Berlin.

Erstgutachterin: Prof. Dr. Katharina J. Franke
Zweitgutachterin: Prof. Dr. Stephanie Reich
Drittgutachter: Prof. Dr. Joachim Heberle

Datum der Disputation: 10.11.2015

Kurzfassung

Als eine Prototyp-Spezies sind Metalloporphyrin-Moleküle ideale Kandidaten um Eigenschaften Metallorganischer Verbindungen für potentielle Anwendung in zukünftigen Anwendungen molekularer Elektronik zu erforschen. In dieser Arbeit wurden die strukturellen, elektronischen und magnetischen Eigenschaften dreier verschiedener Metalloporphyrine mit Hilfe von kombinierter Rastertunnel- und Rasterkraftmikroskopie untersucht.

Wir untersuchten die Adsorption und Selbstorganisation von ManganTetraPyridinPorphyrin (Mn-TPyP) auf einer Cu(111)-Oberfläche. Die Mn-TPyP-Moleküle ordnen sich entlang er <110>-Richtung in linearen Ketten. Abhängig von der Pärparationstemperatur und der molekularen Bedeckung wurden drei Typen von Molekülketten mit zwei verschiedenen molekularen Konformeren gefunden, welche sich in planaren bzw. rotierten Pyridin-Gruppen voneinander unterscheiden. In den Ketten unterscheiden sich Moleküle mit planaren Pyridingruppen durch die Anzahl ihrer Koordinationsbindungen zu Cu-Adatomen. Rastertunnelspektroskopie zeigt breite molekulare Orbitalresonanzen auf den Molekülen mit planaren Pyridin-Gruppen und deutet damit auf eine starke Molekül-Oberflächen-Wechselwirkung hin, während schmalere Resonanzen auf den Molekülen mit rotierten Pyridin-Gruppen auf eine schwächere Wechselwirkung hindeuten. Weiterhin konnten sowohl reversible als auch irreversible Rotationen der Pyridin-Gruppen von Molekülen innerhalb der Ketten induziert werden, welche vermutlich durch resonantes Elektronentunneln durch das Molekulare Orbital bei +2.7 eV aktiviert wurden.

Magnetische Eigenschaften von EisenOctaEthylPorphyrin-Chlorid (FeOEP-Cl) und EisenOctaethylPorphyrin (FeOEP) auf Au(111)-Oberflächen wurden durch die Wechselwirkung mit Au-Spitzen und Chlor-funktionalisierten Spitzen gezielt verändert. Simultane Messungen von Kraft und (differentieller) Leitfähigkeit zeigen, dass die kurzreichweitige repulsive Kraft zwischen Au-Spitze und einem FeOEP-Cl-Molekül das Fe-Zentrum näher an die Au-Oberfläche drückt, was zu stärkerer Fe-Oberflächen-Hybridisierung und damit einer Kondo-Resonanz bei E_F führt. Die repulsive Wechselwirkung zwischen Cl-terminierten Spitzen und FeOEP-Molekülen ändert deren Spinzustand (Oxidationszustand) von S=1 (+2) in S=5/2 (+3), wie sich aus einer in Tunnelspektren aufkommenden Kondo-Resonanz schließen lässt. Auch die attraktiven und repulsiven Wechselwirkungen zwischen Au-Spitzen und FeOEP können Spin-Anregungen bzw. den Kondo-Effekt auf den Molekülen verstärken. Xenon-funktionalisierte Spitzen ändern durch attraktive Wechselwirkung die asymmetrische Dip-Form von Tunnel-Spektren auf FeOEP in symmetrische Spin-Anregungs-Stufen. Weiterhin konnte mit Hilfe von dynamischer Rasterkraftmikroskopie die chemische Struktur von Eisen-TetraBenzoPorphyrin, dem Produkt einer temperaturinduzierten Ringschlussreaktion von FeOEP auf Au(111), abgebildet und damit bestätigt werden.

Die magnetischen Eigenschaften individueller ManganTetraPhenylTertButylPorphyrin-Moleküle (Mn-TPTBP) auf der Au(111)-Oberfläche verändern sich durch die Koordination des Mn(II)-Zentrums zu darauf adsorbierten CO-Molekülen. Tunnelspektren zeigen, dass sich die asymmetrische Kondo-Resonanz von Mn-TPTBP nach der Komplexbildung zu MnTPTBP-CO in eine Zero-Bias-Anomalie verändert, bestehend aus der Überlagerung eines Peaks und eines Dips. Basierend auf Dichtefunktionaltheorie-Simulationen schließen wir darauf, dass das CO-Molekül den Spin der Mn-TPTBP von S=5/2 auf S=1/2 ändert. Das neue spektroskopische Merkmal von Mn-TPTBP-CO stammt wahrscheinlich von einem gemischten Valenzzustand des Mn-Atoms und Vibrationen des Moleküls. Der ursprüngliche magnetische Zustand von Mn-TPTBP kann durch gezielte Desorption der CO-Moleküle vom CO-Mn-TPTBP-Komplex wiederhergestellt werden.

Abstract

As a prototype species, metalloporphyrin molecules are ideal candidates for studying organic/metal interface properties for the sake of future applications of molecular electronics and spintronics. In this thesis, combined scanning tunneling microscopy (STM) and atomic force microscopy (AFM) techniques are utilized for investigating the structural, electronic and magnetic properties of three different metalloporphyrins on noble metal surfaces.

We studied the adsorption and self-assembly behavior of manganese-tetra-pyridine-porphyrin (Mn-TPyP) molecules on a Cu(111) surface. The Mn-TPyP molecules align along the <110> directions and arrange into linear chains. Depending on the annealing temperature of Mn-TPyP/Cu(111) samples and their molecular coverage, three types of molecular chains containing two different molecular conformers with respectively flat and tilted pyridine groups are found on the surface. Within these chains, the molecules with flat pyridine groups are discerned by the number of their coordination bonds to Cu adatoms. Scanning tunneling spectroscopy reveals broad orbital resonances for molecules having flat pyridine groups, indicating strong molecule-surface coupling. In contrast, the molecules with tilted pyridine groups show narrower orbital features due to weaker coupling to the surface. Furthermore, we found both, irreversible and reversible rotation of the pyridine groups of molecules in chains, which is likely activated by resonant electron tunneling through the molecular orbital at +2.7 eV.

Magnetic properties of iron octaethylporphyrin chloride (FeOEP-Cl) and iron octaethylporphyrin (FeOEP) molecules on Au(111) surface are tuned by their interaction with Au tips and chlorine (Cl) functionalized tips, respectively. Simultaneously force and (differential) conductance measurements show that the short range repulsive force between a Au tip and a FeOEP-Cl molecule pushes the Fe center toward the Au surface and enhances the Fe-surface hybridization, thus giving rise to a new Kondo peak at the Fermi energy. The repulsive interaction between Cl-terminated tips and FeOEP molecules changes the molecular spin state (oxidation state) from S = 1 (+2) into S = 5/2 (+3), indicated by the Kondo resonance in differential conductance (dI/dV) spectra. The attractive and repulsive interaction between Au tips and FeOEPs can enhance spin excitation and Kondo effect for the molecules, respectively. Xenon (Xe) functionalized tips change the asymmetric dip shape of the dI/dV spectra of FeOEP into spin excitation related step features due to the attractive tip-molecule interaction. Moreover, we confirm the chemical structure of iron tetrabenzoporphyrin generated by temperature induced ring closure reaction of FeOEP on Au(111) surface by NC-AFM measurement.

The magnetic state of individual manganese-tetra-phenyl-tert-butyl-porphyrin (Mn-TPTBP) molecules on a Au(111) surface is modified when the Mn(II) center coordinates to CO molecules adsorbed on top. dI/dV spectra show that the asymmetric Kondo peak of Mn-TPTBP changes into a zero-bias anomaly with a superposed line shape consisting of a peak and a dip when the CO-Mn-TPTBP complex is formed. Based on density functional calculation we conclude that the CO molecule reduces the spin of the adsorbed Mn-TPTBP from S = 5/2 to S = 1/2. The new spectral feature on Mn-TPTBP-CO is probably originating from a mixed-valence state of the Mn atom and a vibration of the molecule. The original magnetic state of Mn-TPTBP can be recovered by selective desorption of individual CO molecules from the CO-Mn-TPTBP complex.

Contents

Introduction

With the rising demand for higher computing power and data storage densities, the size of device components in information processing and storage technology was gradually decreased over the past decades. Nowadays, inorganic semiconductor-based industry uses top-down methods allowing parallel fabrication of devices at large-scale. In order to further decrease the size of single transistors and thus increase chip integration level, intensive work is done for developing new fabrication techniques (like electron-beam lithography) in semiconductor industry. However, signal fluctuations due to quantum tunneling effects and tremendous power dissipation are expected to severely degrade the device functions at circuit widths below 20 nm [1].

Introducing new materials and fabrication methods is helpful to overcome the limitation mentioned above. As firstly proposed by Richard Feynman in 1959 [2], single atoms or molecules can be used as building blocks for novel type of electronic devices and thus signal processing, i.e. molecular wires, molecular switches, or molecular diodes. Progresses in chemical synthesis offer almost infinite possibilities for molecular structures and functionalities. To date, a single atom transistor [3] or molecule transistor [4] have been demonstrated. Nevertheless, the real industry application is still a long way to go. In this prospect a key issue is the growth of molecular electronic devices or materials on surfaces. While it is difficult for the top-down methods fabricating nanostructures with atomic-precision, bottom-up approaches can be used.

Development of scanning tunneling microscopy (STM) [5] and atomic force microscopy (AFM) [6] make the imaging and manipulation of single atoms and molecules accessible. The rapid progress of scanning probe techniques allows today the creation of nanostructures atom by atom [7], [8], [9] or molecule by molecule [10]. However, this method is time consuming and not suitable for large scale fabrication. An alternative bottom-up method called molecular self-assembly is widely used for supramolecular structures on surfaces. In this approach, organic molecules can form extended and ordered nanostructures via intermolecular van der Waals forces [11], hydrogen-bonds [12] and even covalent bonds [[13], [14]]. Moreover, coordination bonding allows for combination of molecules with metal atoms in well-defined networks [15], which offers fascinating perspectives for electronic and magnetic devices [16], [17].

Another essential aspect of molecular assemblies on surfaces is the molecule-surface

interactions. First of all, the surface may act as a template. The symmetry of the surface can lead to a preferred adsorption at certain sites of the surface and can be used to direct molecular growth processes [18]. On the other hand, adsorbates tend to adsorb at surface sites with a high chemical reactivity and high adsorption energy [19], imposing steric constraints that decrease the molecular conformation freedom. Furthermore, alignment of electronic levels [20], [21] or screening effects [22] can take place leading to a change of the electronic properties of the adsorbed molecules. Competition between molecule-substrate and intermolecular interactions determines structural properties of the assemblies. A microscopic understanding of the molecular geometry upon assembly on surfaces is crucial for the design and application of organic electronics. Non-contact atomic force microscopy (NC-AFM) [23] is an ideal instrument for resolving molecular chemical structure with atomic resolution in real space [24], [25]].

Metalloporphyrin (metal = Mn, Fe, Co, Ni and Cu) is a particular interesting class of materials and widely used in various fields of science and technology, such as life process [26], heterogeneous catalysis [27], molecular electronics [28] and opto-electronics. Metalloporphyrins are well established molecular building blocks in surface-based nanoscale systems due to their inherent functionality [29]. Previous researches had already shown the conformational flexibility of the metalloporphyrin molecules adsorbed on surfaces, which can be used as a switching unit in molecular electronics [30]. Moreover, the magnetic properties of the transition metal atoms incorporated in metalloporphyrins can be tuned by the contacted metal surfaces [31], the STM tip [32] or ligated diatomic species like carbon monoxide (CO) [33] and nitric oxide (NO) [34]. This makes the manipulation of a single spin at the atomic level possible, which is a critical issue for spintronics and magnetic storage application.

In this thesis, we study the structural, electronic and magnetic properties of three different meso-substituted metalloporphyrin molecules adsorbed on Cu(111) and Au(111) surfaces, respectively. The molecule/surface systems are investigated by a combined STM and AFM technique. For STM, it can provide high spatial resolution image and high energy resolution scanning tunneling spectroscopy (STS) of molecular systems on surfaces. Additional NC-AFM measurements are utilized to explore the intramolecular structures and atomic force between tip and sample. The outline of the thesis is listed as follows:

In chapter 1, we give a brief introduction to the theoretical fundamental of STM/AFM and the experimental setup.

In chapter 2, the properties of surface-anchored magnetic metalloporphyrin molecules like magnetism and Kondo effect are discussed.

In chapter 3, we study the self-assemblies of Mn-TPyP molecules on a Cu(111) surface. The bonding characters of molecules in linear chains are deduced from

intermolecular distances and high resolution STM images. The geometries of dark and bright molecules in chains are resolved by frequency shift (Δf) images taken by NC-AFM at varied tip-molecule distances with a CO functionalized tip. The orbital features of molecules in chains and their spatial distributions are characterized by differential conductance (dI/dV) spectra and maps, respectively. The rotation of the pyridine end groups in different molecular species is induced by the tunneling electrons.

In chapter 4, we investigate the force and conductance for the Au(111) surface anchored FeOEP-Cl and FeOEP molecules contacted respectively by Au tips and Cl functionalized tips, which induces a novel Kondo peak in the dI/dV spectra of both molecular species. The force and conductance between tip and molecule are extracted from the NC-AFM recorded Δf-ΔZ curve and the STM recorded I_t-ΔZ curve by deconvoluting the oscillating tip effect. Au tips and Xe-terminated tips are also used for tuning the magnetism of FeOEPs. Moreover, the chemical structure of the iron tetrabenzoporphyrin originated from the ring-closure reaction of FeOEP is resolved by NC-AFM with intramolecular contrast.

In chapter 5, we focus on the electronic and magnetic properties of Mn-TPTBP molecules and CO molecule coordinated Mn-TPTBP complex on Au(111) surface. The Mn-TPTBP molecules show an asymmetric Kondo peak, which is verified by temperature-dependent measurements of dI/dV spectra. The CO-Mn-TPTBP complexes exhibit a novel line feature consisting of a dip on top of a peak in their dI/dV spectra. We demonstrate a reversible spin state manipulation between S = 5/2 and S = 1/2 of the Mn ion uncoordinated or coordinated by a single CO ligand.

In chapter 6, we summarize the results presented in this thesis.

1 Theory and Experimental Techniques

Since the invention of the scanning tunneling microscope (STM) in 1981, it has turned out to be an invaluable and widespread instrument for both scientific research and industrial inspection. Due to the outstanding work by presenting the first working STM, G. Binnig and H. Rohrer [5], [35] were honored with the Nobel prize in physics in 1986.

The STM provides new insight into the physics at the nanoscale in real space, compared to other methods (like LEED) presenting average information over large sample area in reciprocal space. The high spatial resolution allows STM investigating the physical and chemical properties of samples on sub-angstrom scale. Besides the imaging ability, STM can also inspect the electronic properties of samples and manipulate single atoms and molecules on the surface with its tip [7].

Although there is enormous success of the STM, it suffers from a serious limitation that STM studies can only be carried out for conductive samples since the tunneling current flowing between the tip and the sample is used as the imaging signal. Moreover, the contrast in STM images depends on both the topography and the detailed electronic structure of the sample, making the interpretation of STM images not straightforward.

These limitations have been overcome with the atomic force microscope (AFM), developed and first introduced by G. Binnig et al. in 1986 [6]. With the AFM operating in contact mode, atomic resolution had been achieved already in 1987 [36]. The development of non-contact atomic force microscopy (NC-AFM), based on a tip attached to a lever oscillating with its resonance frequency, promoted the realization of the atomic resolution on reactive surfaces under UHV conditions [37]. Attachment of a conductive tip to the stiff force sensor like tuning forks [38], [39] allows simultaneous detection of tunneling current and short-range atomic forces at sub-nanometer oscillation amplitudes, integrating the advantages of STM and AFM in one experimental setup.

In this chapter we will introduce the theory and working principles of STM and AFM (section 1.1, 1.2) and a description of the used low-temperature STM/AFM system will be given (section 1.3). We will mainly focus on the aspects that are relevant for this thesis.

1.1 Scanning Tunneling Microscopy

The working principle of a STM is based on the quantum mechanical tunneling effect. As shown in Figure 1.1 a), a sharp metallic tip is positioned a few angstroms above a conductive surface with a narrow potential barrier, forming a STM junction. When a bias voltage in the range of a few volts is applied between the tip and surface, electrons can tunnel through the vacuum barrier with a finite probability and a net current flow I_t is detectable. The tunneling current I_t shows an exponential dependence on the tip-surface distance z: $I_\mathrm{t} \propto \exp(-\mathrm{A}\Phi^{1/2}z)$, where A is a constant and Φ is the work function. A rule of thumb says that the tunneling current increases (decreases) by one order of magnitude when the vacuum gap between the tip and the sample is decreased (increased) by 1 Å. Therefore, the tunneling current can serve as feedback signal for controlling the tip-sample distance precisely, which is realized by varying the voltages applied to the piezos holding the tip due to piezoelectric effect. Nowadays, the widely used piezo tube scanners [40] in scanning probe instruments can easily achieve subnanometer positioning accuracy with sufficient damping of external vibrations. The highly sensitive dependence of tunneling current on tip-sample distance and high accuracy of piezo scanners for controlling tip motion, bring STM into real application with subnanometer resolution.

There are two scanning modes to obtain topographic image of the surfaces: the constant current mode and constant height mode (Figure 1.1 b). In constant current mode, the tip-sample distance is regulated by a feedback loop to keep the tunneling current constant over the surface and the tip height at every scanning point composes a topography image of the surface. In contrast, in the constant height mode the feedback is switched off and the tip scans over the surface at a predefined height. Accordingly, the recorded image reflects the variations in the tunneling current I_t. Constant-height mode scanning can only be performed on atomically flat surfaces under the condition of a low drift rate and good vibration separation to prevent the tip from crashing into the sample.

1.1.1 Theory of Scanning Tunneling Microscopy

In 1983, Tersoff and Hamann presented the first quantitative model based on first-order perturbation theory for explaining the working principle of STM [43]. They treated the tunneling junction as a locally spherical tip in proximity to a flat surface. In the limit of low bias voltage and temperature, the tunneling current between tip and sample can be written as:

$$I_\mathrm{t} = (2\pi/\hbar)\mathrm{e}^2 V \sum_{\mu\nu} |M_{\mu\nu}|^2 \delta(E_\nu - E_\mathrm{F})\delta(E_\mu - E_\mathrm{F}) \tag{1.1}$$

where $\hbar$ is the Dirac constant, e is the elementary charge, V is the applied sample voltage, E_ν and E_μ are the respect energy of surface state ϕ_ν and tip state ϕ_μ, E_F is the Fermi energy, and $|M_{\mu\nu}|$ is the tunneling matrix element between states ϕ_ν of the

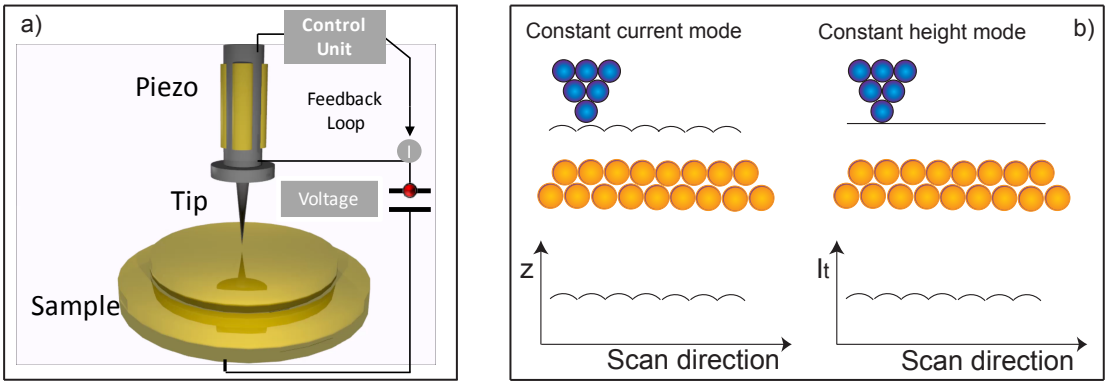

Figure 1.1: a) Scheme of the working principle of a STM [41]. A bias voltage is applied to the sample and the tunneling current I_t between tip and sample is recorded. The surface is imaged by moving the tip precisely with the piezo regulated by the control unit. **b)** Schematic illustration of constant current and constant height scanning modes [42].

surface and ϕ_μ of the tip. According to Bardeen's transfer Hamiltonian approach [44], $M_{\mu\nu}$ is given by:

$$M_{\mu\nu} = -(\hbar^2/2m) \int d\vec{S}(\phi^*_\mu \nabla\phi_\nu - \phi_\nu \nabla\phi^*_\mu) \tag{1.2}$$

where m is the effective electron mass and the integral is over the surface $\vec{S}$ lying between the tip and surface electrodes.

To evaluate the matrix element $M_{\mu\nu}$ (equation 1.2), Tersoff and Hamann expanded the surface wave function in the way that parallel to the surface it is described by Bloch's theorem while perpendicular it decays exponentially into the vacuum. The wave functions of the tip were chosen to be asymptotic spherical form. For simplicity they assumed the same work function Φ for both the tip and the surface. Then the tunneling current becomes:

$$I_\mathrm{t} = 32\pi^3\hbar^{-1}\mathrm{e}^2 V\Phi^2\rho_\mathrm{t}(E_\mathrm{F})R^2k^{-4}e^{2kR}\sum_\nu |\phi_\nu(\vec{r_0})|^2\delta(E_\nu - E_\mathrm{F}) \tag{1.3}$$

where $\rho_\mathrm{t}(E_\mathrm{F})$ is the tip density of states (DOS) per unit volume, R is the radius of curvature of the tip centered at $\vec{r_0}$ and $k = \hbar^{-1}(2m\varphi)^{1/2}$ is the inverse decay length for the wave functions in vacuum. The sum term $\sum_\nu |\phi_\nu(\vec{r_0})|^2\delta(E_\nu - E_\mathrm{F})$ represents the density of states of the surface located at the position of the probe tip and with energy of E_F. Assuming that the DOS of the tip is constant in the corresponding energy window, the tunneling current is proportional to the LDOS of the surface.

However, above derivation of I_t is based on the assumption of low bias voltage (around 10 mV). In real experiment, finite bias voltages (typical $\pm$ 3 V) are applied to the STM junction, which leads to a shift of the Fermi energies of tip and sample with respect to each other. To take the contribution of the states within the finite

voltage range for the tunneling current into account, a more general formula of I_t is given by the Wentzel–Kramers–Brillouin (WKB) approximation solution [45], [46]:

$$I_{\mathrm{t}} = (4\pi \mathrm{e}/\hbar) \int_{E_{\mathrm{F}}}^{E_{\mathrm{F}}+\mathrm{e}V} \rho_{\mathrm{t}}(E_{\mathrm{F}} - \mathrm{e}V)\rho_{\mathrm{s}}(E)|M_{\mathrm{st}}(E,V,z)|^2 dE \tag{1.4}$$

Here, the tunneling current is represented by a simple convolution of the density of states of the tip ρ_{t} and the surface ρ_{s} using the tunneling probability $T(E,V,z) = |M_{\mathrm{st}}(E,V,z)|^2$. The tunneling probability is determined by the tip-surface distance, the work functions of the sample Φ_{s} and tip Φ_{t} and the bias voltage:

$$T(E,V,z) = exp\left[-\frac{2z\sqrt{2m}}{\hbar}\sqrt{\frac{\Phi_{\mathrm{s}}+\Phi_{\mathrm{t}}}{2} + \frac{\mathrm{e}V}{2} - E}\right] \tag{1.5}$$

When positive bias voltages is applied to the sample (Figure 1.2 a), electrons tunnel from the tip into the unoccupied states at the surface. By reversing the sample bias to negative values (Figure 1.2 b), electrons will tunnel from the sample into the unoccupied state of the tip. The sample states at higher energies have higher tunneling probabilities, indicated by the length of the blue color arrows. Assuming constant tip density of states ρ_{t} and tunneling probability $T(E,V,z)$ in the bias window of interest, the tunneling current I_t is proportional to the integration of the sample density of states ρ_{s} in the energy window $[E_{\mathrm{F}}, E_{\mathrm{F}} + eV]$.

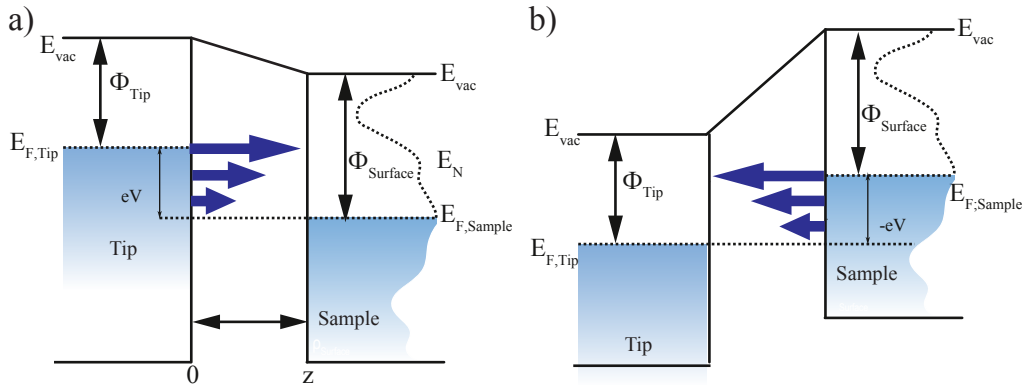

Figure 1.2: Energy level diagram of the STM junction (adapted from [41]). **a)** At positive sample bias, electrons tunnel from occupied electronic states of the tip into unoccupied electronic states of the sample. **b)** At negative sample bias, electrons go from the sample to the tip electrode.

1.1.2 Scanning Tunneling Spectroscopy

Scanning tunneling spectroscopy (STS) is an extension of STM, which can be used to characterize the electronic properties of metallic substrates and adsorbed molecules. Following equation 1.4, the tunneling between tip and sample is determined by three

interconnected parameters: the tunneling current I_t, the bias voltage V and the tip-sample distance z. In STS measurements, one of these three parameters is recorded as a function of a second one while the third one is fixed. Hence, there are three modes for taking spectroscopy: i) in I-z mode, dependence of the current on the tip-sample distance is resolved at a constant voltage V, which allows determination of the sample local work function [35], [47]; ii) in I-V mode, a I-V curve is recorded by sweeping the sample voltage while z is unchanged, and iii) in z-V mode, current is kept constant and the variations in z are measured for different voltage values.

I-V characteristic are the most widely used spectroscopy technique in STM community. For recording the I-V curves, the STM tip is positioned at a desired height with a open feedback loop and the current is measured when ramping the bias in a predefined range. While taking the I-V curves, differential conductance dI/dV can be obtained by using a lock-in amplifier through adding a small sinusoidal modulation signal $V_{ac} = V_{mod}\sin(\omega t)$ to the sample bias voltage. The derivation of equation 1.4 with respect to the bias voltage V give the expression as:

$$\begin{aligned}\frac{\mathrm{d}I}{\mathrm{d}V} \propto\ & \rho_{\mathrm{t}}(E_{\mathrm{F}})\rho_{\mathrm{s}}(E_{\mathrm{F}}+\mathrm{e}V)T(E_{\mathrm{F}}+\mathrm{e}V,\mathrm{e}V,z) \\ &+ \int_{E_{\mathrm{F}}}^{E_{\mathrm{F}}+\mathrm{e}V} \rho_{\mathrm{t}}(E-\mathrm{e}V)\rho_{\mathrm{s}}(E)\frac{\mathrm{d}T(E,\mathrm{e}V,z)}{\mathrm{d}V}dE \\ &+ \int_{E_{\mathrm{F}}}^{E_{\mathrm{F}}+\mathrm{e}V} \rho_{\mathrm{s}}(E)\frac{\mathrm{d}\rho_{\mathrm{t}}(E-\mathrm{e}V)}{\mathrm{d}V}T(E,\mathrm{e}V,z)dE \end{aligned} \tag{1.6}$$

Assuming that the tip density of states and the tunneling probability are constant at low sample biases, the last two integral terms equal zero and equation 1.6 is simplified to:

$$\frac{\mathrm{d}I}{\mathrm{d}V} \propto \rho_{\mathrm{s}}(E_{\mathrm{F}}+eV) \tag{1.7}$$

Hence, the dI/dV signal is proportional to the LDOS of the sample $\rho_s(E_{\mathrm{F}}+eV)$ at the energy $E_{\mathrm{F}}+eV$. In general, the dI/dV signal is a good approximation to the LDOS of the sample at an energy value eV, being V the bias voltage applied between the sample and the tip. However, for high sample bias voltages the exponential increase of the tunneling probability $T(E,V,z)$ has to be taken into account [48].

For z-V mode spectroscopy, the dI/dV spectrum can also be measured by the lock-in amplifier. This method can prevent the molecules from being destroyed by the high tunneling current, and it can also enhance the LDOS intensity at low bias voltages. Compared to I-V mode spectroscopy, the z-V mode dI/dV is less closely related to the sample states when considering the dependence of the tunneling probability $T(E,V,z)$ on the barrier width z [49], [50]. A general trend is that the LDOS peaks in dI/dV are slightly shifted to lower energy in z-V mode [50].

When extending the spectroscopy measurement from a single point to a sample area, the dI/dV mapping technique provides a method for characterizing the spatial

variation of sample density of state at certain energies. Accordingly, two mapping modes can be used by either fixing the tip-sample distance z (constant height mode) or the current I (constant current mode). While planar molecules is preferred to be investigated under constant height mode, the constant current mode is usually utilized for mapping three dimensional objects.

1.1.3 Elastic and Inelastic Electron Tunneling Spectroscopy

Upon adsorption on metallic substrates, the discrete electronic states of atoms and molecules are shifted in energy and broadened due to the their hybridization with the electronic bands of the electrodes (Figure 1.3 a). For a STM junction, electrons from an occupied state on the tip tunnel into an unoccupied state of the sample, giving rise to a resonance in the dI/dV spectrum (Figure 1.3 c). This is an energy-conserved process, namely elastic tunneling. Additionally, tunneling electrons can excite vibrational [51], [52] and spin degrees of freedom [53], which are inelastic tunneling process and have energy loss (Figure 1.3 b). The inelastic excitation opens a new transport channel for the conductance, indicated by symmetric steps at the energy of $\pm\Delta$ in the dI/dV spectrum (Figure 1.3 d).

Tunneling electrons may excite a single molecular vibrations when their energy exceeds the energy of the corresponding vibrational mode $\hbar\omega$, with ω the vibronic frequency. This excitation originates from electron-phonon coupling, thus is rather weak. In the case of molecular vibrations excited by tunneling electrons, the change of conductance $\Delta G/G$ is generally in the order of 10% [54], [55]. Since inelastic electron tunneling spectroscopy (IETS) is able to spatially resolve vibrational intensity with sub-angstrom resolution in single molecules, it can be used to identify the molecular species confined inside STM junctions [56].

It is more efficient for tunneling electrons interacting with single and isolated spins due to the strong electron-spin coupling. For spin excitation, the energy barrier for single spin induced by magnetic anisotropy has to be surpassed by the tunneling electrons and a new conductance channel opens. Spin-excitations can lead to a much larger change for the conductance $\Delta G/G$ than molecular vibration, which probably reach up to 100% or more [57]. Due to strong electron-spin coupling, cascaded spin excitations from lower to higher energy levels can be realized by the tunneling electrons in the case of high current densities and long spin lifetimes, which is spin-pumping [58].

1.2 Atomic Force Microscopy

In AFM measurement, the force between the scanning tunneling tip and the sample is used as the imaging signal. Therefore, the AFM can not only measure conductive samples but also insulators. A key component in AFM is the cantilever, which

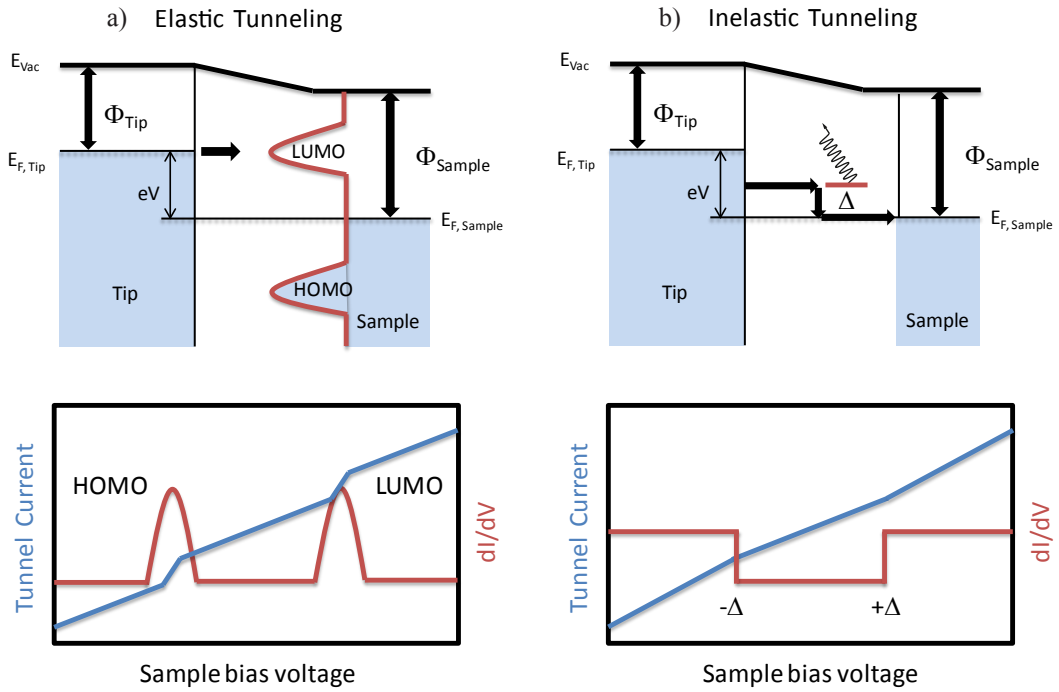

Figure 1.3: Elastic and inelastic electron tunneling process. **a)** Electrons from an occupied electronic state of the tip tunnel into an unoccupied state of the sample with positive sample bias, giving rise to a orbital resonance in dI/dV spectrum. The tunneling through a orbital is a elastic process without energy loss. **b)** Electrons tunnel through the energy barrier and induce a vibration or spin excitation of the adsorbate, open a new transport channel reflected as steps in dI/dV spectrum. Energies of the excitations is given by the tunneling electrons, thus corresponding to a inelastic process.

can sense the tip-sample force by its deflection. Because the tip-sample force has a nonmonotonic distance dependence, it brings complexity for tip height controlling in AFM measurement and for interpretation of the obtained results.

In AFM, two basic operation modes namely the static (contact) mode and the dynamic (non-contact) mode are available. In static mode, the imaging signal is given by the cantilever deflection $q = F/k$ induced by the tip-sample force, where k is the cantilever spring constant. During scanning, the constant force map $z(x, y, F_{ts} = Const.)$ can be acquired by fixing the q to a certain value with a feedback loop. In the dynamic mode, a mechanical actuator is used to deliberately drive the cantilever and keep it oscillating at its eigenfrequency f_0, and the oscillation amplitude or frequency can serve as feedback signal. Hence, there are two alternative modulation methods for operating dynamic AFM, i.e., the amplitude modulation (AM) [59] or frequency modulation (FM) [60]. In AM-AFM, the cantilever is stimulated at fixed frequency with fixed amplitude. When the tip is close to the sample, the change of the cantilever oscillation amplitude caused by the tip-sample interaction is recorded by the feedback loop as imaging signal. Alternatively, the change of

frequency $\Delta f = f - f_0$ induced by the tip-sample force acts as the imaging signal in FM-AFM when keeping the cantilever oscillation amplitude constant.

In our experiment setup, we extend a pure STM to a combined STM/AFM system by attaching a tungsten tip to a tuning fork (TF) sensor, which works in the frequency modulation dynamic mode (Figure 1.4). For tuning fork sensor, piezoelectric effect is employed for reading its deflection. High stiffness of the tuning fork ($k = 1800$ N/m) enables stable operation with small amplitude down to 0.1 Å without tip-sample contact. The small amplitude guarantees that during the oscillation cycle of the force sensor, the tip is always stay in the tunneling regime. Therefore, both the tunneling current and the AFM parameters like the frequency shift (Δf), oscillation amplitude (A_0) and driving amplitude (A_D) can be measured simultaneously. The working principle, relation between frequency shift and force, dissipation and various force contributions in FM-AFM will be discussed in the following.

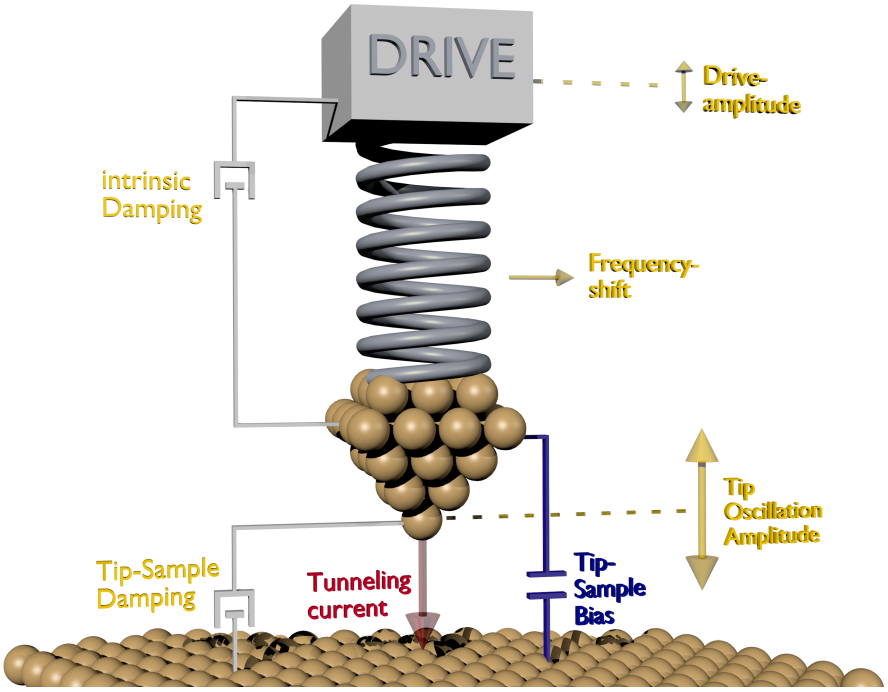

Figure 1.4: Scheme of the dynamic STM-AFM (adapted from [61]). The amplitude, frequency shift and damping (labeled in yellow color) are main physical observables in the AFM part of the experimental setup.

1.2.1 Model for Dynamic AFM: A Harmonic Oscillator

The free oscillating tuning fork can be considered as a harmonic oscillator with a periodic motion perpendicular to the sample surface. There are three degrees of freedom for a oscillating tuning fork: the amplitude, the frequency, and the phase difference between excitation and oscillation. The motion of a damped harmonic

oscillator with driving signal can be described by the equation as [62]:

$$m\ddot{x} - \frac{m\omega_0}{Q}\dot{x} + k_0 x = F_D \cos(\omega t) \tag{1.8}$$

where k_0 is the spring constant of the oscillator, $\omega_0 = \sqrt{k_0/m}$ and related to the resonant frequency f_0 by $\omega_0 = 2\pi f_0$, the quality factor Q is a measure of the oscillation energy loss and relevant to the damping constant via $2\gamma = \omega_0/Q$, and the periodic driving force with amplitude F_D provides a driving amplitude A_D for the oscillator with a frequency ω according to $F_D = k \cdot A_D$.

The solution gives the formula of amplitude as a function of the driving frequency:

$$A(\omega) = \frac{k_0}{m}\frac{A_D}{\sqrt{4\gamma^2\omega_0^2 + ({\omega_0}^2 - \omega^2)^2}} \tag{1.9}$$

which corresponds to the resonance curve. In the case that the excitation frequency is equal to the resonant frequency of the undamped cantilever $\omega = \omega_0$, equation 1.9 can be simiplified into:

$$A(\omega_0) = A_D \cdot Q \tag{1.10}$$

To maintain a 50 pm oscillation at ω_0 for a tuning fork sensor with $Q = 10000$ in ultra-high vacuum, only a small driving amplitude as 5×10^{-15} m is needed.

1.2.2 Force Spectroscopy in FM-AFM

In the dynamic AFM, the free oscillating tuning fork can be perturbed by the tip-sample force (F_{ts}) when tip and sample are close to each other. With a much smaller oscillation amplitude compared to tip–sample distance z, the spring constant k_0 of the free oscillator will be changed into the effective spring constant as $k^* = k_0 - \partial F_{\mathrm{ts}}/\partial z$ [63]. Based on the assumption that the tip-sample force gradient $\partial F_{\mathrm{ts}}/\partial z$ is smaller than k_0, the frequency shift can be approximated as [63]:

$$\Delta f = -\frac{f_0}{2k_0}\frac{\partial F_{\mathrm{ts}}}{\partial z} \tag{1.11}$$

which indicates that the imaging signal in FM-AFM, the frequency shift (Δf), is proportional to the tip-sample force gradient.

Small oscillation amplitude of the tuning fork is helpful for probing the short-range tip-sample forces, which can give rise to atomic resolution. Nevertheless, larger amplitudes are used in many AFM studies. A more general expression of the frequency shift for arbitrary oscillation amplitude is derived from first-order perturbation theory in the Hamilton-Jacobi approach [63]:

$$\Delta f = -\frac{f_0}{\pi A_0 k_0}\int_{-1}^{1} F_{\mathrm{ts}}(d + A_0(1+u))\frac{u}{\sqrt{1-u^2}}du \tag{1.12}$$

where d is the closest distance between the tip and sample during the oscillation cycle. Since the $\Delta f(z)$ spectroscopy is directly recorded in FM-AFM measurement, the force and energy between tip and sample can be calculated. From equation 1.12, Sader and Jarvis proposed an analytic expression for extracting forces from $\Delta f(z)$ by deconvoluting the tip oscillation effect [64]:

$$F(z) = \frac{2k_0}{f_0}\int_z^\infty \left\{\left(1+\frac{\sqrt{A_0}}{8\sqrt{\pi(t-z)}}\right)\Delta f(t) - \frac{A_0^{3/2}}{\sqrt{2(t-z)}}\frac{\partial \Delta f(t)}{\partial t}\right\} dt \qquad (1.13)$$

The method is very accurate for force calculation with a maximum error of less than 5% at midrange oscillation amplitudes for the cantilever. Figure 1.5 shows a typical $\Delta f(z)$ curve of a chlorine functionlized tip approaching on a iron octaethylporphyrin (FeOEP) molecule and its corresponding force curve deconvoluted by using equation 1.13. The $\Delta f(z)$ curve and force curve have similar line shape, and both of them can be divided into three sections. As indicating by the vertical dashed red lines, the force curve are separated into long-range attraction regime (I), attraction-repulsion transition regime (II) and short-range repulsion regime (III). The $\Delta f(z)$ curve also has these three corresponding regimes, although it shifts slightly by 0.2 Å with respect to the force curve. This provides the information for interpreting $\Delta f(z)$ images at different tip-sample distances with approach of the tip toward samples. When tip is far away from the sample (attractive force regime), negative Δf signal is to be obtained and the higher sample gives rise to more negative values of Δf. With approach of the tip, the negative values of Δf will increase since the repulsive force between tip and sample arises and thus partially compensates the attractive force. When further reducing the tip height, the tip-sample repulsion dominates their interaction and induces positive Δf values in the images. Therefore, a contrast inversion is visible in Δf images when tip-sample interaction goes through attraction into repulsion.

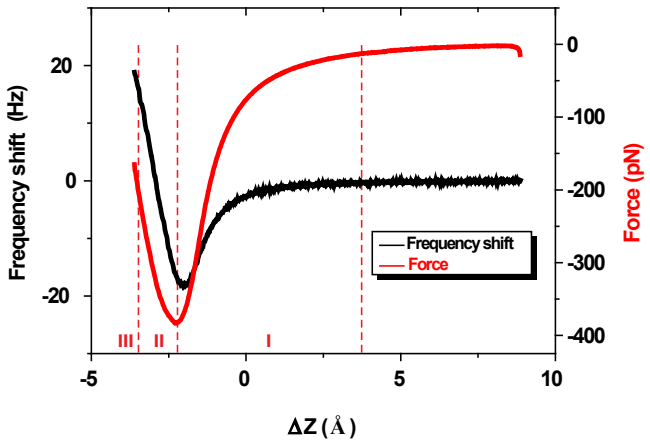

Figure 1.5: A typical $\Delta f(z)$ curve and its deconvoluted force curve. Oscillation amplitude of 50 pm is used for acquiring the $\Delta f(z)$ signal.

1.2.3 Dissipation in Dynamic AFM

In FM-AFM, conservative tip-sample forces can be deduced from the frequency shift signal when the oscillation amplitude is constant. Additionally, non-conservative interactions can also exist in real AFM measurements, e.g. repeating bond formation and breaking during the tip oscillation cycles. In this case, extra damping effect except the intrinsic damping of the tuning fork has to be taken into account, which would change the effective quality factor Q_{eff} and affect the oscillation amplitude as:

$$A(f_0) = A_D \cdot Q_{eff} = A_D \cdot (Q - \frac{\pi f_0}{\gamma_{ts}}) \tag{1.14}$$

where γ_{ts} is the damping constant of the dissipative tip-sample interaction.

In order to realize effective measurement of the tip-sample force, an amplitude feedback controller is used to adjusts the driving amplitude and keep the oscillation amplitude constant. This method also allows to measure and quantify the tip-sample dissipation. When the tip is far away from the sample, we determine the quality factor Q and the driving amplitude A_D needed to maintain a constant oscillation amplitude A_{osc} for the free oscillating tuning fork. The intrinsic damping induced energy dissipation in every oscillation cycle for the free tunning fork is given by:

$$D_0 = \frac{2\pi E_0}{Q} \tag{1.15}$$

where $E_0 = k \cdot {A_0}^2/2$ is the energy stored in the motion of the oscillating cantilever.

In the experiments the tip oscillates close to the sample, additional damping occurs and the driving signal A_D is increased by the amplitude controller to A'_D in order to keep the same oscillation amplitude A_{osc} as the free tuning fork constantly. Then the energy dissipated per oscillation cycle due to tip-sample interactions becomes a simple linear relation [23]:

$$D_{ts} = D_0(\frac{A'_D}{A_D} - 1) \tag{1.16}$$

For a typical qPlus sensor with $f_0 = 20$ kHz, $Q = 10000$, $k = 1800$ N/m and an oscillation amplitude of $A_{osc} = 50$ pm, the energy stored in its motion is $E_0 = 14.04$ eV and the intrinsic energy dissipation is $D_0 = 8.82$ meV for each oscillation period. This allows us to characterize dissipation effects in the energy scale of millielectronvolts per oscillation cycle.

1.2.4 Forces in Atomic Force Microscope

In AFM measurements, the total force acting on the AFM tip consists of different types of forces, which have varied physical sources and distinguished distance dependent behaviors. In our UHV experiments, the chemical force, the van der Waals (vdW) force and the electrostatic force are the main contributions.

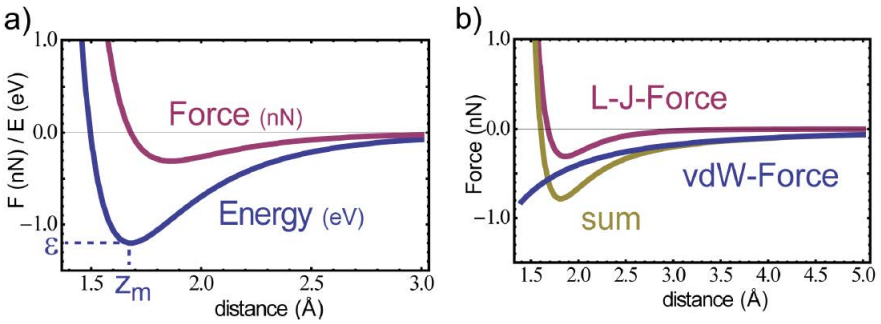

Figure 1.6: [61] **a)** Modeled Lennard-Jones potential and the relevant Lennard-Jones force as a function of the distance between two atoms. Z_{m} and ϵ are the bond distance and the binding energy, respectively. **b)** Lennard-Jones force derived from **a)**, modeled van der Waals force (Hamaker approach) and the sum of them.

The Chemical Force

The short-range chemical force arises with the overlap of electron wave functions from the probe tip and sample, when a subnanometer distance exists between them (In this range the tunneling current is detectable). Depending on tip-sample distance z, the chemical force can be attractive or repulsive. It is empirically modeled by the Lennard-Jones potential [65]:

$$E_{\mathrm{LJ}}(z) = \epsilon \left[\left(\frac{\mathrm{Z_m}}{z} \right)^{12} - 2 \left(\frac{\mathrm{Z_m}}{z} \right)^{6} \right] \tag{1.17}$$

where ϵ is the bonding energy at the equilibrium distance $\mathrm{Z_m}$. The $(1/z)^{12}$ term stands for a repulsive force acting only at very short distance, originating from the Pauli repulsion. The Pauli principle prohibits occupation of the same quantum states by two electrons from tip and sample and force electrons to fill higher energy levels, hence increasing the whole system energy and inducing repulsion force. In contrast, the $(1/z)^6$ term represents an attractive interaction resulted from the van der Walls force, which will be discussed later.

The chemical force is given by the differentiation of the Lennard-Jones potential:

$$F_{\mathrm{LJ}}(z) = -\frac{\partial E_{\mathrm{LJ}}(z)}{\partial z} = 12 \frac{\epsilon}{\mathrm{Z_m}} \left[\left(\frac{\mathrm{Z_m}}{z} \right)^{13} - \left(\frac{\mathrm{Z_m}}{z} \right)^{7} \right] \tag{1.18}$$

Figure 1.6 a) shows the modeled Lennard-Jones potential and force by using parameters of ϵ = -1.2 eV and $\mathrm{Z_m}$ = 1.68 Å.

The van der Waals Force

The attractive van der Waals (vdW) force is induced by mutual interactions of fluctuating dipole moments in nearby atoms and molecules. The vdW potential for

two atoms separated by a distance z can be described as:

$$E_{\mathrm{vdW}}(z) \propto -\left(\frac{1}{z}\right)^6 \tag{1.19}$$

which is one part of the chemical potential (equation 1.17) since it is of relative short range and weak. However, it can be quite large between macroscopic objects due to its additivity. In AFM experiment, the long range vdW forces can be significant because of the macroscopic tip. For a spherical tip with radius R next to a flat surface, the van der Waals force can be modeled with the Hamaker approach as [66]:

$$F_{\mathrm{vdW,ts}}(z) = -\frac{HR}{6z^2} \tag{1.20}$$

where H is the material dependent Hamaker constant and z is the distance between the plane connecting the centers of surface atoms and the center of the closest tip atom. The modeled van der Waals force with $R = 20$ Å and $H = 3$ eV together with the Lennard-Jones force and their sum are plotted in Figure 1.6 b). As one can see, the van der Waals force acts as a strongly attractive background at larger tip-sample distance, while the chemical force dominates when the distance is minimized.

It is also worthwhile to note that a sharp tip is helpful for decreasing the vdW force when taking $\Delta f(z)$ spectroscopy. For the sake of acquiring the short-range force between the tip apex atom and a sample from $\Delta f(z)$ spectra, irrespective of the macroscopic tip shape, a background correction of the force is necessary. Usually, the force between the tip apex and the adsorbates on surfaces is extracted from the force curve taken on the adsorbates by subtracting the reference spectra taken on the substrate [24],[67]. Since the atomic resolution in AFM images originates from the short-range chemical force, a sharp tip is highly desirable for entering the repulsive tip-sample interaction regime.

The Electrostatic Force

Long-range electrostatic interaction arises when a potential (work function) difference exists between a conductive tip and sample. In this way, the tip-sample system can be described as a capacitor with varying capacitance $C(z)$ depending on tip-sample distance z. The electrostatic force is then given by:

$$F_{\mathrm{el,ts}} = \frac{1}{2}\frac{\partial C}{\partial z}(V - V_{\mathrm{CPD}})^2 \tag{1.21}$$

where V is the applied sample voltage and V_{CPD} is the contact potential difference (CPD) between the tip and sample, thus $(V - V_{\mathrm{CPD}})$ is the effective electrostatic potential. The electrostatic force is always attractive since the tip-geometry dependent term $\partial C/\partial z$ is negative all the time. By choosing a sample bias $V = V_{\mathrm{CPD}}$, the contact potential difference can be compensated and the electrostatic forces are minimized. This method allows determination of the CPD value experimentally [68]. We should also pay attention to the short-range electrostatic the forces in case of ionic crystal surfaces [69] or polar surfaces like CuN_2 [70].

1.3 Experimental Setup

All the measurements presented in this thesis were performed in a combined STM-AFM working at low temperature and in ultra high vacuum (UHV), following the design of Dr. Gerhard Meyer and SPS-Createc GmbH [71]. A briefly introduction about the main features of the STM/AFM system will be given in this section.

1.3.1 UHV Chamber

The photo of our STM/AFM system is shown in Figure 1.7 a), which is supported by four air damping feet for decreasing the low frequency mechanical vibrations. The whole system consists of a preparation chamber and a STM/AFM chamber, separated by a gate valve. This valve prevents the SPM chamber from being contaminated by undesired molecules and sputter gas. The preparation chamber is connected to a small loadlock chamber equipped with turbo pump, which allows attachment and detachment of molecule/metal evaporators, sample holder and tuning fork sensor transfer tools without breaking the vacuum in the preparation chamber. A base pressure around 2.0×10^{-10} mbar is routinely maintained in the preparation chamber with a an ion getter pump and titanium sublimation pump. A quadrupole mass spectrometer is equipped for the preparation chamber for monitoring the residual gas components. For sample preparation, a ion sputter gun and leak valve for filling Ne gas into the chamber can be used for getting clean metal surfaces. The single-crystal metal samples are mounted onto small resistive button heaters incorporated on the standard sample holder, with a k-type thermocouple attached for controlling the sample temperature. Sample transfer between the preparation and the SPM chamber is accomplished with a rotatable manipulator with high precision in all three directions. Moreover, the manipulator can be cooled down with liquid helium. This makes the sample temperature adjustable over a wide range from 100 K to $\sim$ 900 K. A sample parking stage inside the preparation chamber can store up to four samples, which is necessary for changing samples by the manipulator.

1.3.2 STM/AFM Head

Figure 1.7 b) shows the structure of the SPM head based on the Besocke beetle design [72], [73]. In this setup the sample holder with sample is clamped against a baseplate, on which three outer (coarse) piezos are mounted. Each of these three piezos has a glued sapphire sphere on top, supporting a threefold copper ramp. The central (main) piezo, which is fixed at the center of the ramp, holds the tuning fork sensor with two magnets. The ramp can be rotated around its center by applying sawtooth-shaped voltage pulses to the quadrature electrodes of the coarse piezos. Since the copper ramp has three slightly inclined planes on its bottom side, the motion of the ramp is used for controlling coarse approach or retraction of the tip. An aluminum ring around the ramp allows for lateral movement for changing

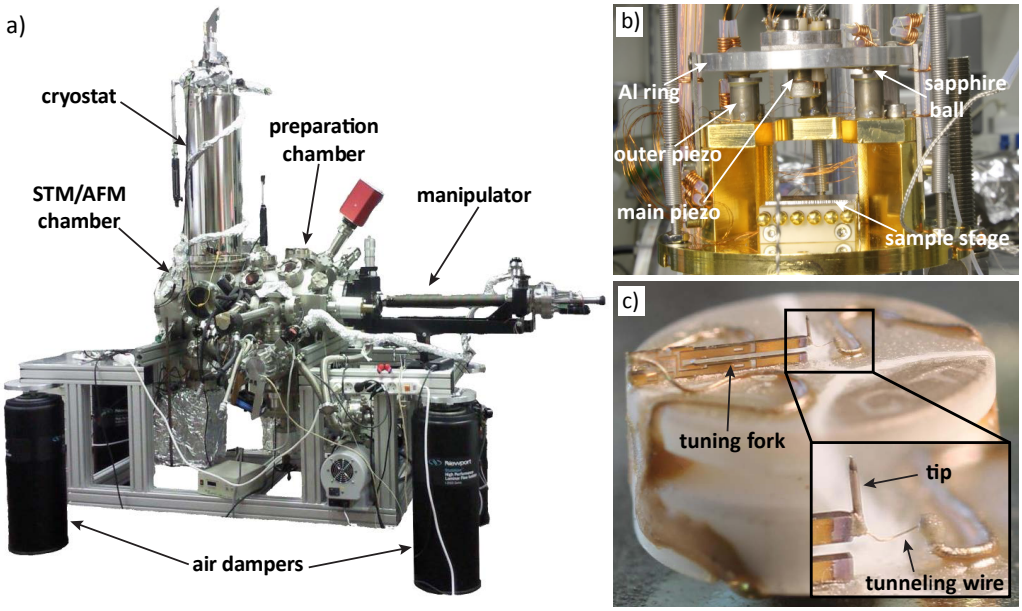

Figure 1.7: Experimental setup. **a)** Photo of the LT UHV STM/AFM chamber. **b)** Enlarged view of the STM/AFM head. **c)** Zoom-in photographs of the tuning fork dynamic force sensor. Inset shows the SPM tip and its connected wire for tunneling current.

scanning area over the sample, and also protects the ramp from falling off the piezo-sapphires.

The structure of the sensor is shown in Figure 1.7 c). The commercially available quartz tuning forks are standard ones (like they are used in e.g. wristwatches), with oscillation frequency 32.768 kHz and theoretical spring constant 1800 N/m. Following the qPlus design [39], one prong of the tuning fork is firmly glued on an insulated ceramic base, while the other prong remains free to oscillate perpendicularly to the sample surface. A piece of 25 μm tungsten wire is attached to the apex of the free prong to serve as the STM/AFM tip. To avoid crosstalk between the STM and AFM channels, a separate 12.5 μm Au tip wire is connected to the bottom of the tungsten tip wire to measure the tunneling current independently of the tuning fork electrodes used for deflection detection. There are three electrical contacts between the copper ramp and sensor: two for the tuning fork piezoelectric AC current and one for the tunneling current. The tuning fork oscillation is excited mechanically by applying an AC voltage to the central piezo. During measurement, the whole SPM head with clamped sample is isolated from mechanical vibrations via stainless steel springs and an eddy current damping system.

The STM/AFM scanner head is covered by two thermal radiation shields and cooled down with a bath cryostat consisting of a liquid helium tank and a liquid nitrogen tank. The inner shield is thermally connected to the helium tank and the outer one is connected to the surrounding liquid nitrogen tank. This cooling design can

maintain the STM/AFM stage around 4.5 K for more than 48 hours in our machine without refilling of helium and nitrogen.

The measurement data is acquired by the PSTMAFM software from SPS-Createc GmbH. STS spectra are recorded with an external commercial Stanford Research SR830 lock-in amplifier, which can output processed data with low noise level. For AFM measurements, an additional phase locked loop (PLL) controller from SPECS-Nanonis is utilized. For analysis of the experimental data, we use WSxM [74] and SpectraFox software [75].

1.4 Substrates and Molecules

1.4.1 Coinage Metal Surfaces

In this thesis, we investigated metal-organic molecules on two low-index coinage metal surfaces, namely Au(111) and Cu(111). Both gold and copper single crystals have a face centered cubic (fcc) structure with lattice constants of 2.88 Å and 2.55 Å, respectively. Metal atoms on the (111) lattice plane of fcc crystal arrange into hexagons, exhibiting a trigonal surface symmetry [76], as shown in figure 1.8 a).

In the STM image of a Au(111) surface (Figure 1.8 b), the most prominent feature is the parallel zigzag ridges, which is induced by the surface herringbone reconstruction but not the case for Cu(111) surface. Such reconstruction is formed by incorporating 23 surface atoms into 22 bulk lattice sites in the $[1\bar{1}0]$ direction [77], causing more stress and smaller interatomic distance between the atoms in the topmost layer. Therefore, a part of the Au atoms on the surface are pushed to occupy the energetically unfavorite hexagonal close-packed (hcp) or bridge sites along the $[11\bar{2}]$ orientation. The unit cell of the reconstructed Au(111) surface are separated by the soliton lines (bridge sites) into alternating fcc and hcp packing region with periodic length of 3.8 Å and 2.5 Å, respectively. The zigzag lines result from the reconstruction in three equivalent orientations rotated by 120° due to the trigonal symmetry of the Au(111) surface. The surface shows a corrugation with a height modulation of 0.2 Å caused by the reconstruction.

The coinage metals (like Au and Cu) have similar electronic properties and they all exhibit a partially filled Shockley surface state in (111) direction. Figure 1.8 c) shows the dI/dV spectrum of Au(111) surface, with a step-like feature around -500 mV corresponding to the onset of the surface state band edge [78]. Similarly, Cu(111) surface has a surface state located at -440 mV [7]. Furthermore, the reconstruction of Au(111) surface make it as an electronic superlattice, in which the hcp region has lower potential energy of 25 meV and a slightly higher local density of states (LDOS) compared to the fcc region [78]. Nevertheless, the fcc region is more energetically stable for adsorbates due to its low atomic density with respect to the hcp region [77]. Additionally, the elbows of soliton lines are preferential adsorption sites for

molecules and impurities because the potential energy is diminished there [79], [80].

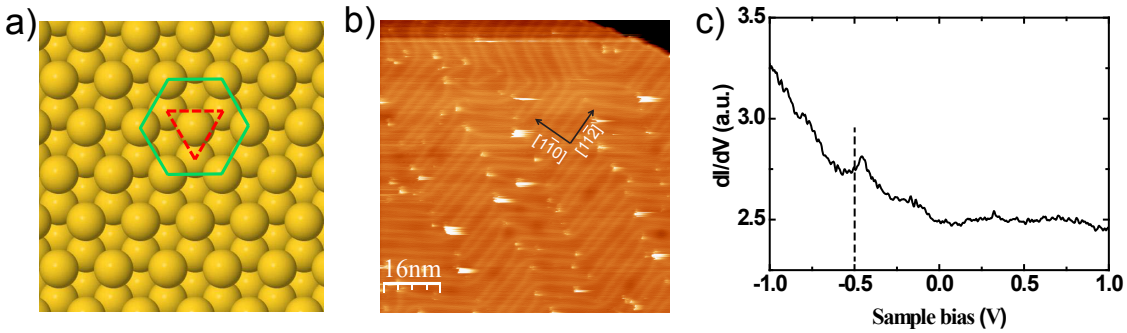

Figure 1.8: Coinage metal surfaces. **a)** Topview of the (111) lattice face of fcc single crystals. Surface atoms arrange into hexagon patterns (green) and the red triangle highlights the trigonal surface symmetry. **b)** STM image of Au(111) showing surface reconstruction (V = 1.0 V and I = 45 pA). **c)** dI/dV spectrum of a bare Au(111) surface, acquired with open feedback loop (setpoint: V = 1.0 V and I = 52 pA).

1.4.2 Metalloporphyrin Molecules

Metalloporphyrins have become an essential class of molecular components as functional devices in recent years, with applications ranging from molecular switches to supramolecular assembly and gas sensors. The central metal atom is four-fold coordinated by the inner nitrogen atoms of the four pyrrole rings connected by methine units, constituting the porphyrin macrocycle. The outer substitutes are attached to the meso-positions at the methine bridges, and bring various structure possibilities for the metalloporphyrins (Figure 1.9).

The functionality and self-assembly of metalloporphyrins on metal surfaces is based on three major properties: i) The metalloporphyrin macrocycle can host magnetic or nonmagnetic metal centers, which provide active sites for reversible ligation of axial adducts to form porphyrin-ligand complexes [81], [82]. ii) A wide range of meso-substituents can be attached to the metalloporphyrins. The peripheral groups determine molecular functionalities and make them as building blocks for metal-organic networks [83] and 2D molecular engineering [84], [85]. iii) Flexibility of the metalloporphyrin core and the rotation or bending freedom of the meso-groups permit conformational adaptation of the molecule to its local environment [86], [87], [88] and conformation manipulation [89], [90].

The flexibility of the macrocycles and variable dihedral angles of the substituents are crucial features of substituted metalloporphyrins and directly affect their electronic and magnetic properties. Attachment of axial ligand can alter the adsorption geometry and molecular orbital, thus affecting the spin state or oxidation state of metalloporphyrins. The magnetic properties of metalloporphyrin molecules will be presented in the second chapter of this thesis.

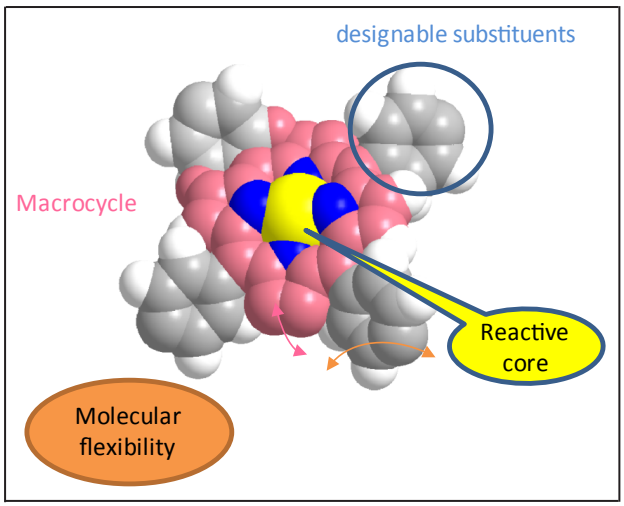

Figure 1.9: Main properties of metalloporphyrins [91]. The possibility for incorporating different metal center atoms (yellow), the programmable meso-substituents (here is phenyl ring) and the flexibility of the macrocycle (pinkish) and peripheral groups constitute the main functionalities of metalloporphyrin molecules.

1.4.3 Sample Preparation

Molecule systems	Mn-TPyP on Cu(111)	FeOEP-Cl on Au(111)	Mn-TPTBP on Cu(111)
Evaporator	415 °C	170 °C	310 °C
Substrate	RT	-30 °C	RT

Table 1.1: Temperatures of molecular evaporator and metal substrates for molecule deposition.

The Au(111) and Cu(111) single-crystal substrates are cleaned by repeated Ne^+ ion beam sputtering and subsequent annealing in the preparation chamber. For each cycle of cleaning, the metal substrates are kept at room temperature (RT) and sputtered for 30 minutes by ion with kinetic energies of ~ 1 keV, and then heated up to 800 K for a few minutes. This procedure can give rise to atomically flat terraces free of impurities, which are ideal platforms for the adsorption of molecules.

The molecules are thermally deposited onto the pretreated metal surfaces from a home-built Knudsen cell with cooling water. Molecular coverage is controlled by the evaporation time and temperature, and further monitored by a micro quartz-balance. The temperatures of the molecular evaporator and metal substrates for the preparations of the three inspected metalloporphyrin systems in this thesis are listed in Table 1.1. The Mn-TPyP and Mn-TPTBP molecules are deposited on the Cu(111) and Au(111) held at room temperature, while the FeOEP-Cl molecules are preferably dosed onto cold Au(111) surface ($\sim -30\,^{\circ}$C) to avoid the loss of the

Cl ligand. Afterwards, a post-annealing would be applied to the sample for getting regular molecular structures in some cases if necessary, and then the sample is cooled down by liquid helium and transferred into the STM chamber for measurement.

2 Properties of Magnetic Metalloporphyrin Molecules on Metal Surfaces

2.1 Magnetism of Metalloporphyrins

Coordination complexes like metalloporphyrin molecules incorporating $3d$ transition metal atoms (like Mn and Fe) with partially filled electron shells usually show magnetic moment originating from the unpaired spins. For the coordinated metal atoms, the energy scale and electron occupations of their $3d$ orbitals are determined by the surrounding ligands. In early days, the orbital characteristics of coordination complexes were described in the framework of crystal field theory (CFT), which can explain most of the experimental results quite well. However, molecular orbital (MO) theory is highly appealing with crystal field theory for corroborating some properties of the coordination complexes like their colors etc, thus evolve into a more comprehensive model called ligand field theory (LFT).

2.1.1 Crystal Field Theory

Pure crystal field theory assumes that the only interaction between the metal ion and the ligands is an electrostatic one with the ligands being regraded as negative point charges. If a spherically symmetric field of negative charges is placed around the metal, the orbitals will remain degenerated, but all of them will be raised in energy as a result of the repulsion between the negative field and the negative electrons in the orbitals. Considering a non-spherical electric field caused by the real ligands for metal atoms in coordination complexes, degeneracy of the d orbitals will be removed. The additional electrostatic potential of the crystal field can be expressed as [92]:

$$H_{CF} = -\sum_i e \cdot V(x_i, y_i, z_i) \tag{2.1}$$

where $V(x_i, y_i, z_i)$ is the electrostatic potential representing the Coulomb interaction between the electrons of the magnetic atom and the neighboring ligand charges and depends on the crystal field symmetry.

For easy understanding of the d orbital splitting, an octahedral complex which is formed by a metal atom surrounded by six identical ligands is illustrated here (Figure

2.1 b). The ligands are symmetrically positioned along the Cartesian coordinate axes. In this octahedral field, energies of the d orbitals will be raised because of negative charge repulsion. However, the energy increases for d orbitals are supposed to be not the same due to the relative spatial arrangements of the orbitals to the ligands. The orbitals lying along the axes (the d_{z^2} and the $d_{x^2-y^2}$) will feel stronger repulsion than the orbitals with lobes lying between the axes (d_{xy}, d_{xz}, d_{yz}), resulting in higher energy for the d_{z^2} and $d_{x^2-y^2}$ orbitals than the other three. Therefore, the d orbitals split into two sets of orbitals labeled as t_{2g} and e_g with an energy difference of Δ, namely the crystal field splitting.

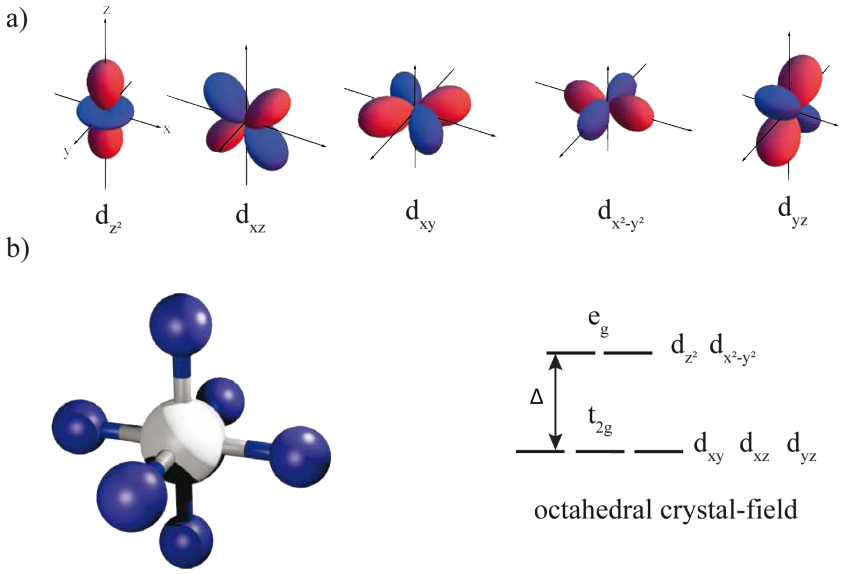

Figure 2.1: a) Schematic sketch of the $3d$ orbitals. **b)** In a octahedral crystal field, the atomic $3d$ orbital set splits into two energy level subsets labeled as e_g and t_{2g}. Graphs are adapted from [41].

2.1.2 Ligand Field Theory

Although the crystal field theory adequately accounts for large quantity of data on transition metal complexes, experimental and theoretical researches presented arguments against the assumption that the d orbitals splitting of metal atoms is a result of a purely ionic interaction without considering the covalent bonding character between metal and ligand. Ligand field theory results from combining the principles laid out in molecular orbital theory and crystal field theory, which describes the removing of degeneracy of metal d orbitals in transition metal complexes. The d orbitals of the metal ion are allowed interacting with a linear combination of the ligand orbitals in the case of same orbital symmetries between them.

Similar as crystal field theory for an octahedral complex, the five d orbitals lose their degeneracy to form e_g (d_{z^2} and $d_{x^2-y^2}$) and t_{2g} (d_{xy}, d_{xz} and d_{yz}) sets (Figure 2.1).

The e_g orbitals of the metal ion and ligands will overlap with each other and form bonding and antibonding σ orbitals, labeled as e_g and e_g^* respectively. Likewise, The t_{2g} orbitals of the metal ion can readily form π bonding (t_{2g}) and antibonding (t_{2g}^*) state with ligand orbitals of matching symmetry. On the other hand, the spatial distribution of e_g and t_{2g} orbitals restrict them to a nonbonding status in a π-only or σ-only system. The ligand field theory accounts for magnetic properties of octahedral complexes based on two sets of orbitals separated by an energy gap Δ between t_{2g} and e_g^*. If the energy gap is larger than the spin pairing energy U, low spin complexes will be formed. Reversely, if the energy needed to pair electrons is greater than Δ, high spin complexes will result.

The ligand field theory is also applicable for metal-organic complexes with other types of symmetries. As an example, dependence of spin configuration of a (porphinato)iron(III) complex on the axial ligand field strength is depicted in Figure 2.2.

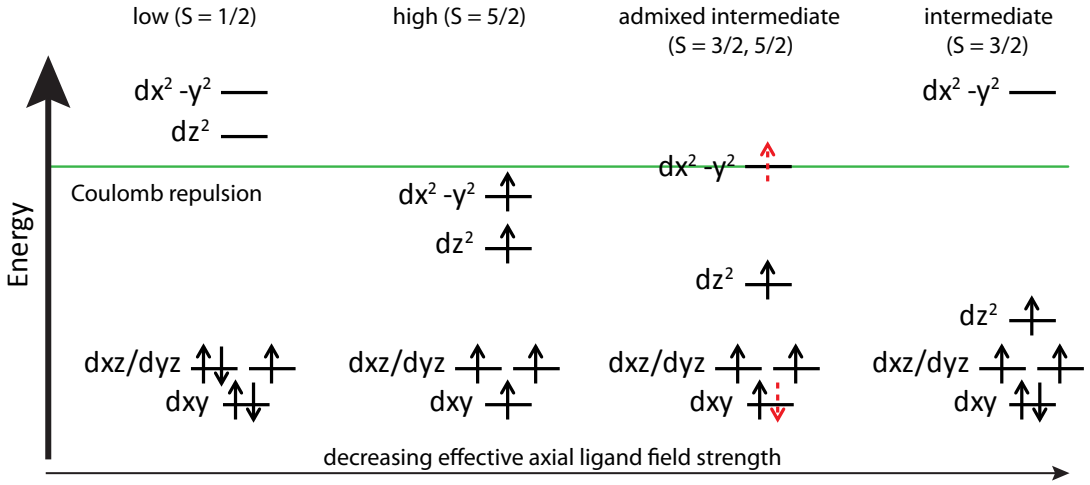

Figure 2.2: Spin configuration of a (porphinato)iron(III) complex with five valence electrons. Depending on the ligand field, the d sub-orbitals are splitted with different energies and electron occupations. The relative energy scale between orbital separation and Coulomb repulsion gives rise to S = 1/2 low-spin, S = 5/2 high-spin, S = 3/2 intermediate spin and admixed intermediate spin of S = 3/2 and S = 5/2 [93]. The green line represents the electron Coulomb repulsion energy U.

2.1.3 The spin-Hamiltonian Approach

The spin Hamiltonian approach is widely used for interpreting the magnetism of single $3d$ metal atoms [94], [95] or molecules including a magnetic metal center [96] without using fundamental theories. Based on the symmetry properties of the atoms or molecules, all the orbital coordinates have been replaced by the spin coordinates for defining the addressed systems. The spin Hamiltonian approach is built on the basis of two central approximations: i) the orbital moment L of the magnetic bricks

is essentially quenched and hence it can be treated as a perturbation; ii) the systems has orbitally non-degenerate ground states [97].

The effective spin-Hamiltonian of systems with singly occupied orbitals is based on Zeeman splitting and spin-orbit coupling [92], [98]:

$$\begin{aligned} H_{eff} &= \mu_B \vec{B} \cdot (\vec{L} + 2\vec{S}) + \lambda \vec{L} \cdot \vec{S} \\ &= g_{\parallel}\mu_B B_z S_z + g_{\perp}\mu_B (B_x S_x + B_y S_y) + D[S_z^2 - \frac{1}{3}S(S+1)] + E(S_x^2 - S_y^2) \end{aligned} \tag{2.2}$$

with

$$D = -\lambda^2(-\frac{1}{2}\Lambda_{xx} - \frac{1}{2}\Lambda_{yy} + \Lambda_{zz}), E = \frac{1}{2}\lambda^2(\Lambda_{xx} - \Lambda_{yy}) \tag{2.3}$$

λ is the spin-orbit coupling constant, and the matrix elements Λ_{ii} with $i = x, y, z$ are proportional to the projected unquenched angular momentum L_x, L_y, L_z as:

$$\Lambda_{ii} = \sum_n \frac{\left\langle \psi_0 \left| \widehat{L}_i \right| \psi_n \right\rangle^2}{E_n - E_0} \tag{2.4}$$

ψ_0 and ψ_n represent the ground state and excited states, respectively. E_0 and E_n are corresponding energy of these states. The D parameter represents the magnetic anisotropy between the parallel (along the z-axis) and perpendicular directions (along the x- or y-axis), and E stands for the anisotropy along the x- and y-directions. Both the axial and transverse magnetic anisotropy originate from the spin-orbit coupling. By convention, the axes are assigned in equation 2.3 to maximize $|D|$ and have $E > 0$ [94]. The axial anisotropy D can be either positive or negative, corresponding to an easy-plane or an easy-axis anisotropy respectively. The smallest $|m\rangle$ state of a magnetic center are lowest in energy with easy-plane anisotropy, while the largest $|m\rangle$ state is energetically most stable in easy-axis environment. The nonvanishing E term mixes states of different $|m\rangle$.

In the case of an axial symmetric crystal field with $E = 0$ and assuming that the g-factor is isotropic $g_{\parallel} = g_{\perp} = g$, the spin-Hamiltonian can be simplified into:

$$H_{eff} = g\mu_B \vec{B} \cdot \vec{S} + DS_z^2 - \frac{1}{3}DS(S+1) \tag{2.5}$$

Since $\frac{1}{3}DS(S+1)$ is a constant and only shift the energy levels of all electronic states without changing the physical mechanism, equation 2.5 can become more concise as:

$$H_{eff} = g\mu_B \vec{B} \cdot \vec{S} + DS_z^2 \tag{2.6}$$

In the absence of external magnetic field $\vec{B}$, the H_{eff} in equation 2.6 is accounted by the crystal filed splitting DS_z^2, which will split the $(2S+1)$ spin levels of the

S multiplet and remove degeneracy of the ground state. Therefore this effect is often called zero-field splitting (ZFS) [97]. For an intuitive impression, the ZFS diagram of S = 3/2 and S = 2 spin systems are shown in Figure 2.3. In IETS measurement, electron induced spin excitations between these states is permitted within the selection rule of $\Delta m = 0, \pm 1$.

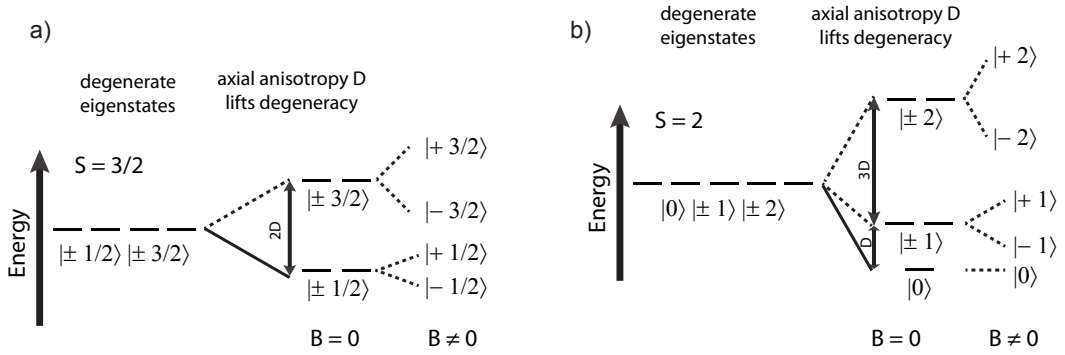

Figure 2.3: Schematic diagram of the zero-field-splitting for **a)** a S = 3/2 and **b)** a S = 2 spin system in a crystal field with axial symmetry and Zeeman splitting.

2.2 The Kondo Effect

The Kondo effect describes the anomalous resistance minimum of dilute magnetic alloy at low temperatures. At high temperatures, the electrical resistance of metals is determined by electron scattering with the lattice vibrations. Lower temperature suppresses the number of phonons involved in the scattering process and thus decreases the resistance. As a consequence, the electrical resistivity decreases monotonically in metals with reduced temperature. At low temperatures scattering at defects and impurities becomes dominant leading to a finite electrical resistance R. However, already in 1930s, Haas et al. found the resistance of a gold wire reached a minimum at a certain temperature (T_K) and then increased again at even decreased temperature [99]. It was recognized that magnetic impurities are responsible for the increasing electrical resistance at $T < T_K$ [100], but the underlying physical mechanism remained unclear for a long time. In 1968, J. Kondo presented a theoretical description [101] of the behavior of the electrical resistance at low temperatures of metals doped with magnetic impurities, which explained the experimental observations within a scattering model by considering the interaction of the localized spin of the magnetic impurities with the conduction electrons. This scattering process becomes dominant at low temperatures leading to a new many-body ground state. A short theoretical description of the Kondo effect based on the Anderson impurity model will be given in the following.

2.2.1 Anderson Single-Impurity Model

The Kondo effect defines the problem of single magnetic impurities interacting with conduction electrons of a nonmagnetic metal host at low temperatures. The Anderson impurity model simplifies the problem into an intuitive scenario by assuming the full electronic structure of the magnetic impurity to be a single orbital state with energy ϵ_d, which can be filled with maximum two electrons. Single occupation by an electron with spin $\sigma =\uparrow$ or $\sigma =\downarrow$ corresponds to a total energy $E = \epsilon_d$ and the related ground state exhibits a two-fold spin-degeneracy ($S = 1/2$) depending on weather the spin is up or down. To fill the orbital with two electrons with spin $\sigma =\uparrow$ and $\sigma =\downarrow$ one has to overcome the Coulomb energy U and the total energy of a doubly occupied system will be $E = 2\epsilon_d + U$. Hybridization between the electronic states in the magnetic impurities and metal host broadens the impurity levels by $\Delta = \rho_0|V|^2$, with ρ_0 as the DOS at E_F of the supporting metal and V as the hybridization matrix element (Figure 2.4 a from [102]).

The Anderson model has different regimes depending on the energy scale of the three parameters: the energy of the magnetic impurity state ϵ_d, the Coulomb repulsion U and the typical resonance width Δ. In the case of $\epsilon_d \sim \Delta$, $U \sim 2\Delta$, an orbital overlap would happen implying spin fluctuations between the single and double occupied state, and the system enters in the so-called mixed valence regime [103]. The Kondo regime only exists when the levels ϵ_d and $\epsilon_d + U$ do not overlap, that is $\epsilon_d \gg \Delta$, $U \gg 2\Delta$.

In the following we only consider the case of a local single occupied orbital, which lies below E_F and is separated by the Coulomb energy U from the double occupied configuration (as shown in Figure 2.4 a). At sufficiently low temperatures, the single spin of the adatom can be flipped by a bulk electron of opposite spin via process 1 or 2 in which the adatom's orbital is either doubly occupied (process 1) or empty (process 2) during the intermediate step (Figure 2.4 b). The spin-flip of electrons between the magnetic adatom and the metal surface form a new many-body ground state around E_F with increased density of states, i.e. the Kondo state.

Now we consider the antiferromagnetic exchange interaction between electrons of the localized magnetic state on the adatom and the metal host, which can be described with the Anderson Hamiltonian [104]:

$$H_A = \sum_\sigma \epsilon_d n_{d,\sigma} + U n_{d,\uparrow} n_{d,\downarrow} + \sum_{k,\sigma} \epsilon_k c^\dagger_{k,\sigma} c_{k,\sigma} + \sum_{k,\sigma} (V_k c^\dagger_{d,\sigma} c_{k,\sigma} + V^*_k c^\dagger_{k,\sigma} c_{d,\sigma}) \quad (2.7)$$

The first term describes the occupation of the impurity's electronic states with energy ϵ_d and occupation number $n_{d,\sigma}$. The second term is the Coulomb interaction U between the electrons with opposite spin $n_{d,\uparrow}$ and $n_{d,\downarrow}$ on the impurity site. In the third term, $c^\dagger_{k,\sigma}$ and $c_{k,\sigma}$ are creation and annihilation operators of wave vector k and spin component σ for the energy eigenvalue ϵ_k of the conduction electrons. The last term represents the hybridization between the impurity's electronic states

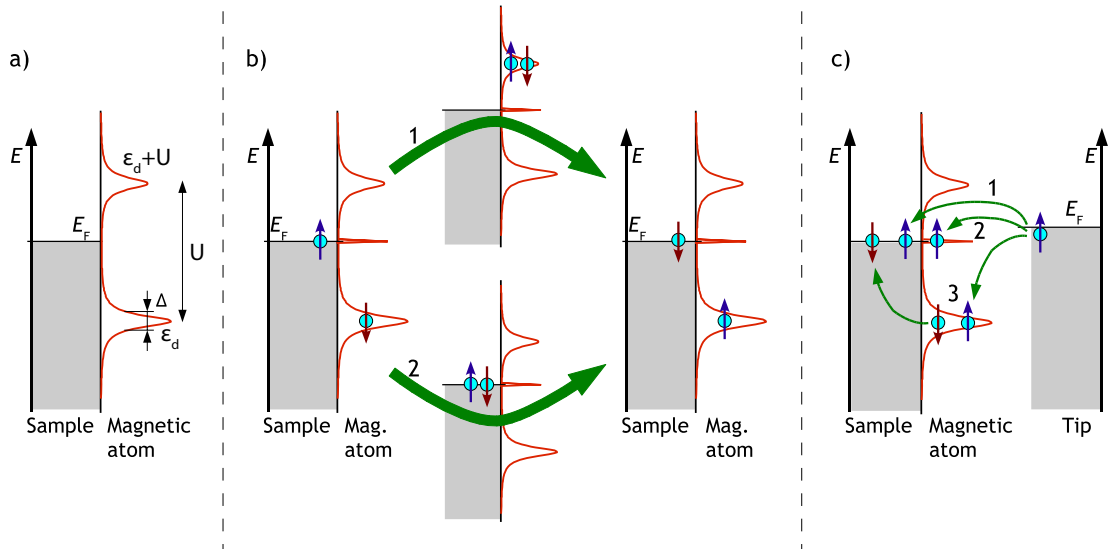

Figure 2.4: Schematic sketch of the Kondo effect. Simplified Anderson impurity model. **a)** The electronic structure of a magnetic adatom on a metal surface is represented by one orbital which could be filled with maximum two electrons. **b)** Two different processes for flipping the single local spin of the adatom by a bulk electron of opposite spin. In process 1 the adatom is doubly occupied during the intermediate step whereas in process 2 the state is empty. These processes form the Kondo resonance close to E_{F}. **c)** Three possible tunneling channels for STM probing electrons. They can either tunnel directly into the empty bulk states (1) or into the Kondo resonance (2), or into the orbital state of the magnetic adatom (3). Processes (1) and (2) conserve the spin while process (3) is an indirect transition via a spin-flip process (adapted from [102]).

and the conduction electrons including the hybridization matrix element V_k (V_k^*). This Hamiltonian defines the scenario of a singly occupied impurity orbital coupling to the bulk electrons. In order to get a more physical picture of the hybridization matrix V_k, the Anderson-Hamiltonian was transformed into the so called Kondo-Hamiltonian by J. R. Schrieffer and P. A. Wolff in 1966. This modification is done by projecting the Anderson Hamiltonian onto the subspace of the single occupied impurity state of the $s-d$ exchange model by a canonical transformation [105]:

$$H_K = \sum_{\sigma} \epsilon_d n_{d,\sigma} + \sum_{k,k'} J_{k,k'}(S^+ c^\dagger_{k,\downarrow} c_{k',\uparrow} + S^- c^\dagger_{k,\uparrow} c_{k',\downarrow} + S_z(c^\dagger_{k,\uparrow} c_{k',\uparrow} - c^\dagger_{k,\downarrow} c_{k',\downarrow})) \quad (2.8)$$

where S_z and $S^\pm = S_x \pm i S_y$ are the spin operators for a state of spin S. The first term again describes the occupation of the impurity state, the same as that in equation 2.7. The second term represents a Heisenberg exchange interaction between a local magnetic moment of the impurity and the conduction electrons with a coupling constant $J_{k,k'}$. Thus, the Hamiltonian describes spin-flip processes upon scattering events of the conduction electron spins with the local impurity electron spin, which can happen in two different pathways as shown in Figure 2.4 b). The Coulomb energy U has to be overcome for filling the impurity's orbital with two opposite

spins (pathway 1), and the energy of $E_{\mathrm{F}} - \epsilon_d$ is needed to fill the impurity's single spin into the bulk state at E_{F} (pathway 2). These processes can be accomplished on the time scale of femtoseconds due to Heisenberg uncertainty principle $\Delta t \sim \hbar/\Delta E$. The antiferromagnetic pairing of the single local impurity spin with electron spins of the bulk continuum forms a new nonmagnetic Kondo singlet state by screening the magnetic moment (as shown in Figure 2.5 a).

2.2.2 The Kondo Temperature

The screening effect of the magnetic impurities with the conduction electrons of the nonmagnetic metal host form a new many-body ground state around Fermi energy, called Kondo state. In order to characterize the binding energy between the unpaired spin localized at the resonance and the electrons in the metallic reservoir, the Kondo temperature T_K is defined as $E_{Bin}^{Kondo} = K_B \cdot T_K$. The Kondo effect can only arise at temperatures lower than T_K, otherwise the screening of the impurity breaks down with thermal fluctuation. T_K can be related to the effective exchange coupling between the localized single spin and the conduction electrons as [104]:

$$T_k \propto D\sqrt{\rho J}\exp(\frac{-1}{\rho J}) \tag{2.9}$$

with D the bandwidth of the substrate electrons. T_K can also be expressed with the parameters of the Anderson model as following [106]:

$$T_k = \frac{1}{2}\sqrt{\Delta \cdot U}\exp[\pi\epsilon_d(\frac{\epsilon_d + U}{\Delta \cdot U})] \tag{2.10}$$

where Δ is the width of the hybridized impurity's energy level with the surface, U is the Coulomb repulsion energy between two electrons at the site of the impurity, and ϵ_d is the energy of the singly occupied impurity level. Within the framework of the Anderson model, the binding energy E_{Kondo} and therefore the Kondo Temperature T_K are determined by the hybridization, Coulomb energy and the detailed electronic structure of the system. Since T_K shows an exponential dependence on the parameters Δ, U and ϵ_d, it can vary in a wide range.

2.2.3 The Kondo Resonance

The first scanning tunneling spectroscopy (STS) observations of the Kondo effect for single magnetic atoms on a metal surfaces were presented by V. Madhavan et al. [107] and J. Li et al. [108] independently in 1998. In these transport measurements, the Kondo resonance exhibits asymmetric shape or dip-like feature, which differ from the Lorentzian line shape described by Abrikosarov and Suhl (assuming electrons can only tunnel into the orbitals of a magnetic impurity). The varied line shape of Kondo resonance originates from the quantum interference of possible tunneling

channels in STS measurement. Figure 2.4 c) illustrates the three different tunneling paths of tip electrons to the surface with magnetic adsorbate on it.

The electrons can either tunnel directly into the empty bulk state above the Fermi energy (path 1) or can tunnel into the Kondo resonance (path 2). These two tunnelling channels will interfere. The last process displayed (path 3) is not contributing to the interference, because during the direct tunnelling into the impurity's orbital a spin flip occurs resulting in a final state with different spin.

U. Fano showed that the interference of a discrete electronic state with a continuum of states can be expressed by the equation [109]:

$$\rho(E) \propto \frac{(q+\epsilon)^2}{1+\epsilon^2} \tag{2.11}$$

where ϵ is the normalized energy:

$$\epsilon = \frac{2(E-E_K)}{\Gamma_K} \tag{2.12}$$

Here E_K is the energetic position and Γ_K is the full width at half maximum (FWHM) of the resonance. The lineshape of the Kondo resonance described by equation 2.7 is determined by the asymmetry-factor q, which is given by:

$$q = \frac{t_2}{\pi\rho_0 V t_1} \tag{2.13}$$

Here t_1 and t_2 correspond to the tunneling probabilities of the two tunnel paths 1 and 2 (see Figure 2.4 c). V refers to the hybridization matrix element of the local singly occupied atomic/molecular level and the continuum states of the surface/bulk. Figure 2.5 demonstrates the dependence of the resonance shape on the q factor. For $q \to \infty$ the Kondo resonance has a Lorentzian lineshape, meaning all electrons tunneling through the many body state. For $q = 0$ the Kondo resonance becomes a dip, corresponding to dominant direct tunneling into the metal surface. For intermediate values of q the resonance shows an asymmetric Fano shape.

The FWHM Γ_K of the Kondo resonance at $T = 0$ K is related to the Kondo temperature T_K:

$$\Gamma_K(T) = 2k_B T_K \tag{2.14}$$

For temperatures $T > 0$ K, the FWHM Γ_K is broadened as [110]:

$$\Gamma_K(T) = 2\sqrt{(\pi k_B T)^2 + 2(k_B T_K)^2} \tag{2.15}$$

where k_B is the Boltzmann constant and T_K is the intrinsic Kondo temperature of the corresponding Kondo system. Except for the thermal broadening of Kondo resonance caused by the finite temperatures for STS measurements, there are also

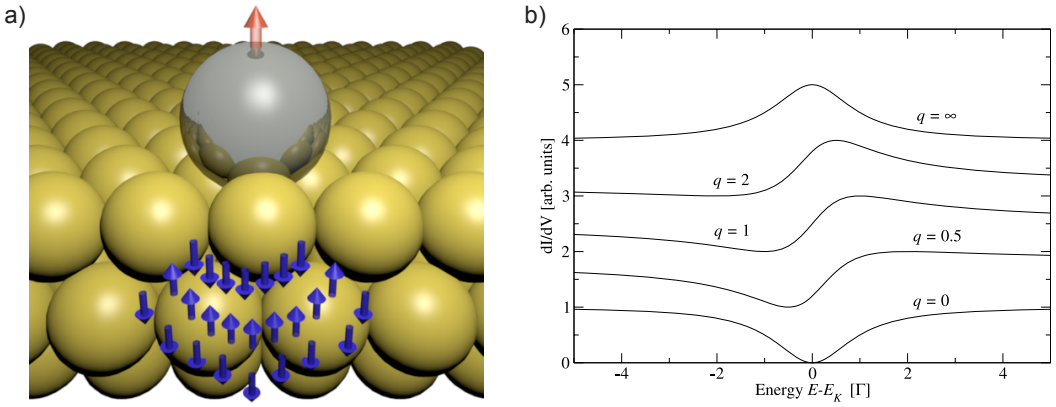

Figure 2.5: a) Screening of the magnetic impurity with antiferromagnetic exchange coupling, adapted from [41]. **b)** Dependence of Fano lineshape on the value of asymmetric factor q, adapted from [102].

two other factors which can affect the spectrum feature: i) temperature-dependent Fermi-Dirac distribution of the electronic states of the tip and sample; ii) modulation V_{rms} of the lock-in amplifier. Considering all these effect for the experimentally obtained Kondo spectra, the measured FWHM Γ_K^{exp} should be corrected for the sake of extracting the intrinsic FWHM Γ_K. This correction can be described with an empirical equation [103]:

$$\Gamma_K^{exp}(T) = 0.78\Gamma_K(T) + 3.52k_BT + V_{rms} \tag{2.16}$$

Here T is the experimental temperature for recording the Kondo spectra.

3 Structure, Electronic Properties and Conformational Change of Mn-TPyP Molecules on Cu(111)

3.1 Introduction

In the past decade, porphyrins and metalloporphyrins adsorbed on metal surfaces had been extensively studied due to their high structure symmetry, conformation flexibility, unique electronic and magnetic properties. Conformational flexibility and functional meso-substitutes have made porphyrins as widely used building blocks for constructing supramolecular architectures on metal surfaces via non-covalent intermolecular interactions (hydrogen-bonding, van der Waals forces) [111], [112], [113] or metal-ligand coordination method [114], [115], [116].

Upon adsorption on surfaces, the porphyrins adapt their conformation to the local environment (like substrate symmetry and lattice constant, neighboring atoms and molecules) [117], [118], [119], which could result into saddle, planar and dome conformers [120], [121]. The conformation adaption is accomplished by deforming their macrocycle and rearranging the terminal substitutes. As shown in Figure 3.1, three different angles are used to describe the geometry of porphyrins. While ρ represents the deformation angle of the macrocycle, θ and ϕ stand for the rotation and bending orientation of the meso-substitutes with respect to the molecule main plane. Molecule-substrate interactions reduce the dihedral angle θ with typical value of 60° for meso-substituted tetra-aryl-porphyrins in gas phase, which induces macrocycle distortions due to steric hinderance between the hydrogen atoms in the pyrroles and substitutes.

The electronic structure of porphyrin molecules adsorbed on metal surfaces is largely determined by the molecular conformations. For the delicate control of physical, chemical, and magnetic properties of molecules at the nanoscale, an understanding of the interplay between electronic properties and molecular conformation must be developed at the single-molecule level. Using scanning tunneling spectroscopy we investigate the energy alignment and spatial distribution for the orbitals of different manganese-tetra-pyridine-porphyrin (Mn-TPyP) species on the Cu(111) surface,

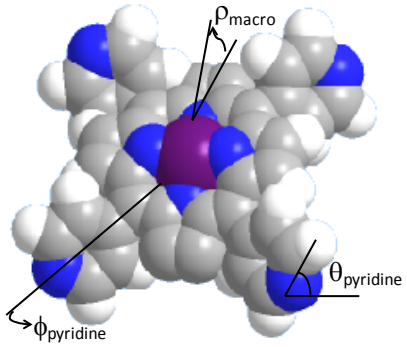

Figure 3.1: Conformational flexibility of Mn-TPyP molecule. The molecule consists of a macrocycle plane with a central Mn atom and 4 peripheral pyridine end groups. After MM2 force-field minimization in CambridgeSoft ChemOffice Ultra 2006, the molecular model has two side lengths (distances between neighboring pyridylic nitrogen atoms) of 11 Å and 10.9 Å, respectively. ρ represents the deformation angle of pyrrole rings in the macrocycle, which is around 60° for meso-substituted porphyrins in gas phase. θ and ϕ represent the rotation and bending orientation of meso-pyridine relative to the molecular core, respectively.

and NC-AFM is utilized for resolving the molecular configurations and intermolecular bonding with high resolutions [24].

Conformational flexibility promotes porphyrins as promising candidates for molecular switches through conformational changes by an external stimulus. The rotation of a di-butyl-phenyl leg in individual Cu-tetra-3,5 di-ter-butyl-phenyl porphyrin (Cu-TBPP) molecules on Cu(211) surface was achieved by the interaction between tip and sample in a reversible way [30]. Moreover, the reversible interconversion between two nonplanar conformations of single Zn(II) Etioporphyrin I molecules adsorbed on a NiAl(110) surface was induced by a STM [90]. On Cu(111) surface, bidirectional switching between the concave and convex conformations of 2H-5,10,15,20-Tetrakis-(3,5-di-tert-butyl)-phenylporphyrin (2HTTBPP) molecules in self-assembled rows at 300 K was observed, but only unidirectional conformational switching from convex to concave could be induced by a STM tip with certain sample bias at 200 K without thermal effect [122]. Although successful conformational manipulation of single metalloporphyrins on surfaces were realized with a STM tip, it is desirable to extend the switch function to porphyrin assemblies for applications of molecular electronics. For this purpose, we present irreversible and reversible pyridine ring rotation processes in self-assembled metalloporphyrin chains on Cu(111) surface. This result emphasizes the importance of local physiochemical environment for interconversion between two metastable molecular geometries.

The properties of Mn-TPyP molecules are presented in the following four sections of this chapter. In the first part, we analyze the adsorption and self-assembly behavior of Mn-TPyP molecules on the Cu(111) surface. In the second part, we show the geometries of two saddled molecular species with intramolecular resolution. Distin-

guished electronic properties of different molecular species and their conformational changes will be depicted in the third and forth parts, respectively.

3.2 Annealing Temperature and Coverage Dependent Self-Assembly of Mn-TPyP

Mn-TPyP molecules are thermally evaporated from a crucible onto the Cu(111) surface, and the Mn-TPyP/Cu(111) sample are annealed above 100 °C for the sake of ordered molecular structures. We find that the conformation and self-assembly of Mn-TPyPs on Cu(111) surface are determined by sample annealing temperature and molecular coverage (Figure 3.2).

3.2.1 Single Row Uniform Chains

For the sample in Figure 3.2 a), Mn-TPyP molecules deposited on the Cu surface with a coverage of $(3.06 \pm 0.09) \times 10^{-2}$ molecules/nm^2 are annealed at 125 °C for 4 minutes. Single row linear chains composed of uniform conformational molecules are distributed along the 3-fold high symmetric <110> directions on the surface, and chain intersections are visible. High resolution STM images show that the porphyrin molecules adopt a quadrilateral shape upon adsorption on the substrate (Figure 3.2 b). A line-profile along the chain direction demonstrates that molecules have an apparent height of 150 pm with respect to the Cu surface and center-center distance of two neighboring molecules is around 20 Å (Figure 3.2 c). In comparison with the molecular dimension $\approx$ 11 Å in gas phase (Figure 3.1), the large intermolecular distance allows incorporation of Cu adatoms between neighboring molecules, which was reported previously for the chain structure of tetra-pyridine porphyrin on Cu(111) surface [123].

The metal-ligand assembly structure of the uniform molecular chains can be recognized in the STM topography imaged with a functionalized tip (Figure 3.2 j) [123], which is obtained during image scanning. Based on the fact that carbon monoxide (CO) molecules adsorbed on a Cu(111) surface are imaged as protrusions by CO functionalized tips [124], [125], it is logical to suggest the tip used for Figure 3.2 j) having a CO apex since small protrusions are visible in the image. We can see four small particles (marked by a dashed ellipse) sandwiched between two neighboring molecules except the macrocycle and four peripheral lobes for each molecule. We suggest these particles bridging neighboring Mn-TPyP molecules in uniform chains to be Cu adatoms since the pyridine group with N lone pair electrons are known to readily bond with Cu adatoms and self-assemble into metal-ligand coordination complexes on metal surfaces [126], [116], [127]. It was claimed that metal adatoms in metal-ligand coordinated supra-structures are difficult to be resolved in STM images due to the electronic effect [128], [129], [130], [15], [131], [132], [133], larger

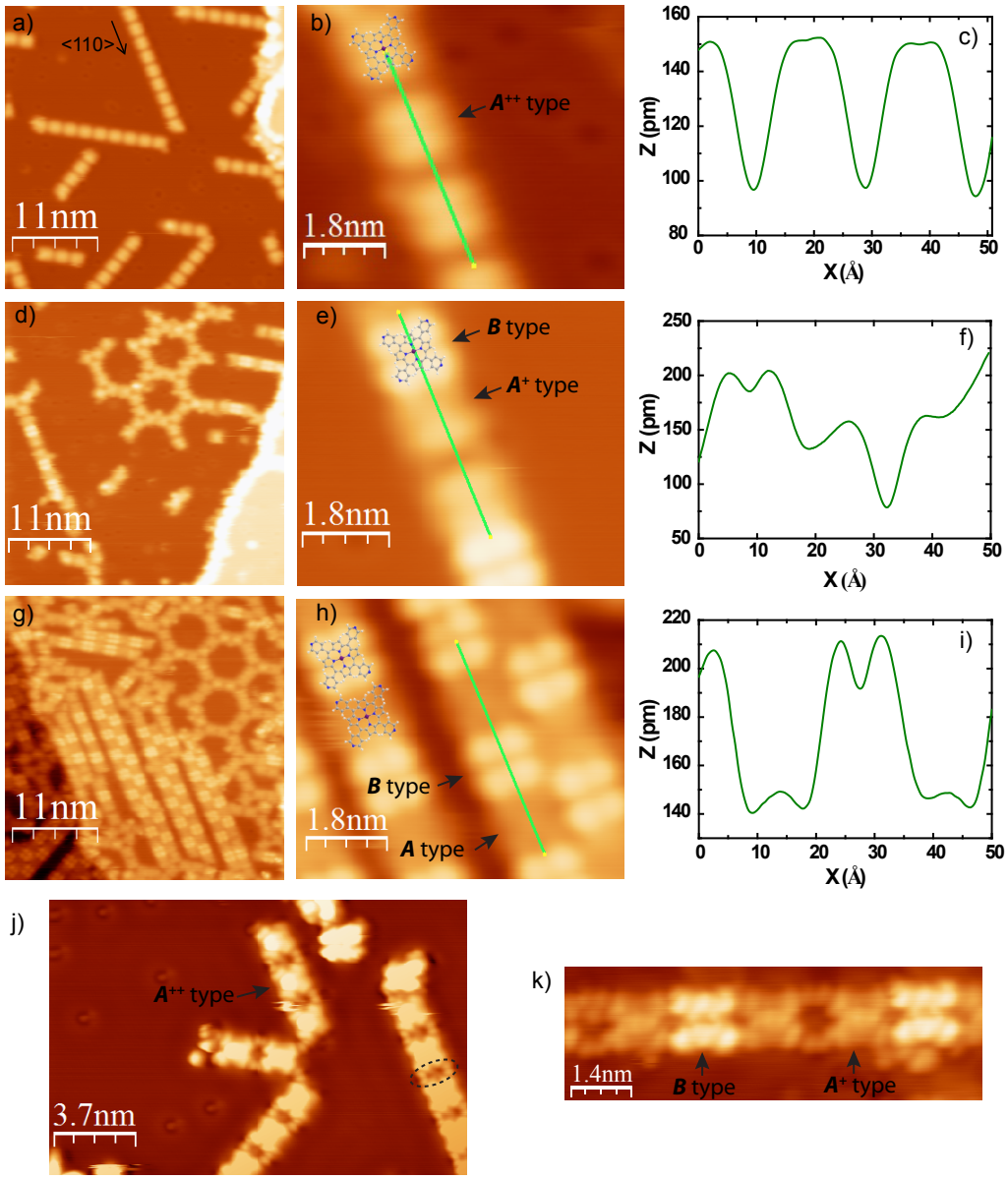

Figure 3.2: Self-assembly of Mn-TPyP molecules on Cu(111) surface. **a)** STM overview and **b)** high resolution image of Mn-TPyP molecules with a coverage of $(3.06 \pm 0.09) \times 10^{-2}$ molecules/nm^2, annealed at $125\,^{\circ}\mathrm{C}$. Single-row chains with uniform molecules (***A***$^{++}$ type) are self-assembled. **d)** STM overview and **e)** high resolution image of Mn-TPyP molecules with similar coverage to **a)**, annealed at $137\,^{\circ}\mathrm{C}$. Dark (***A***$^{+}$ type) and bright (***B*** type) molecules irregularly arrange into the mixed-phase chains, and hexagonal networks appear. **g)** STM overview and **h)** high resolution image of Mn-TPyP molecules with a coverage about 0.26 molecules/nm^2, annealed at $137\,^{\circ}\mathrm{C}$. Single or multiple row chains consist of alternating bright (***B*** type) and dark (***A*** type) molecules, and hexagonal networks (same structure as that in **d**) coexist on the surface. **c)**, **f)** and **i)** line-profile (from top to bottom) along the chain direction in image **b)**, **e)** and **h)**, the height of Cu surface is set to zero. All the images are recorded with V = 1.0 V and I = 100 pA. **j)** and **k)** are CO functionalized tip recorded STM images for Cu adatoms mediated uniform molecule (***A***$^{++}$ type) chains (V = 1.0 V, I = 110 pA) and a mixed phase chain consisting of dark (***A***$^{+}$ type) and bright (***B*** type) molecules (V = 0.1 V, I = 110 pA), respectively.

bonding motifs with two or more Cu atoms linking organic moieties were observed for ordered patterns on surfaces [134], [123], [135]. Hence, it is reasonable to ascribe the four particles to Cu adatoms located at each side of the molecules in uniform chains. In other words, each Cu adatom is coordinated by one pyridylic nitrogen atom and all of these metal-ligand units arrange into periodic Cu-coordinated Mn-TPyP chains on the surface. Since the molecules in uniform chains are bonded by Cu adatoms at both sides, we categorize them as $\boldsymbol{A}^{++}$ type molecule. Moreover, the periodicity of the uniform chains is 8 Cu lattice spacings (20 ± 0.5) Å, indicating good molecule-surface commensuration [136].

3.2.2 Single Row Mixed Phase Chains

The sample in Figure 3.2 d) is prepared with the same condition as that in Figure 3.2 a), but annealed at a slightly higher temperature of 137 °C. There are visible differences between the two samples treated by different annealing temperatures. First, in addtion to single-row molecular chains, triangular structures and hexagonal networks are formed, which are regulated by the substrate symmetry. Furthermore, bright and dark molecules can be distinguished in the chains, but not regularly arranged (Figure 3.2 e). Bright and dark molecules have apparent heights close to 203 pm and 150 pm, respectively. Bright molecules adopt a square shape, characterized by 4 protruding lobes. By superimposing the chemical model of Mn-TPyP onto its STM image, we assign each lobe to one of the pyridine rings. Dark molecules have a contrast difference between their two halves connecting to a neighboring bright and dark molecule respectively, indicating an asymmetric local bonding environment at both sides. The line-profile in Figure 3.2 f) shows that the center-center distance of two adjacent dark molecules is about 20 Å, resembling the uniform molecular chains in Figure 3.2 b). Nevertheless, the distance from a dark molecule to a nearest bright molecule is close to 15 Å. The asymmetric distances suggest that Cu adatoms only stay between two adjacent dark molecules but do not exist between neighboring bright and dark molecules. We assign the molecular chains in Figure 3.2 e) as a mixed phase of bright and dark molecules.

The image of a mixed phase chain recorded by CO tip allows us to get clearer bonding information for molecules in mixed phase chains (Figure 3.2 k). The notable difference of the bonding of dark-dark and dark-bright molecules is visible. Bonding between neighboring dark molecules is still conducted by four small particles, same as the uniform molecule chains. However, the binding site of dark-bright molecules is featureless. This indicates that the neighboring dark molecules are connected by four Cu adatoms while no adatom sits between bright and dark molecules. In this way, the dark molecules with one-side adatom coordination and the bright molecules in mixed phase chains are referred as $\boldsymbol{A}^{+}$ and $\boldsymbol{B}$ type, respectively.

3.2.3 Single Row and Multiple Row Alternating Chains

In order to check the coverage-dependent evolution of the molecular self-assembly on the Cu surface, we add more molecules onto the sample shown in Figure 3.2 d) and anneal it at 137 °C afterwards. As shown in Figure 3.2 g), molecular concentration has been largely increased to about 0.26 molecules/nm^2. Now we can see single-row and multiple-row chains composed of bright and dark conformers, and also hexagonal networks. Moreover, bright and dark molecules are alternately arranged in the chains with a ratio of 1:1, which is much better-ordered than the mixed phase chains in Figure 3.2 d). Bright molecules demonstrate the same appearance and apparent height as the $\boldsymbol{B}$ type molecule in Figure 3.2 e), suggesting that they are identical. Therefore, the bright molecules in mixed phase chains and alternating chains are uniformly labeled as $\boldsymbol{B}$ type. Dark molecules exhibit a central maximum surrounded by four broad lobes. The apparent height difference between these two species is about 60 pm under the scanning condition of V = 1.0 V and I = 0.1 nA (Figure 3.2 i). The dark molecules in alternating chains have similar apparent height as the molecules in single-row uniform chains ($\boldsymbol{A}^{++}$ type) and the dark molecules in the mixed phase chains ($\boldsymbol{A}^{+}$ type), suggesting probable conformational analogy between them. The nearest distance between neighboring bright and dark molecules is about 15 Å, indicating absence of Cu adatoms in the chains. Therefore, we assign the dark molecules in alternating chains as $\boldsymbol{A}$ type. STM image shows that the appearances of the single rows in multiple-row molecular chains and the single-row molecular chains are the same (Figure 3.2 h), suggesting a weak interaction between neighboring molecular rows which do not change the molecular conformations and assembly structure in the aggregated multiple-row chains. Hence, the single-row and multiple-row molecule chains will be treated as equal structures in the later discussion. The appearance of alternating dark-bright molecular chains could be driven by the deficiency of Cu adatoms with increasing molecular coverage. The hexagonal networks in Figure 3.2 g) have the same structure as the corresponding objects shown in Figure 3.2 d), which will not be further discussed because they are supramolecular assemblies composed of molecules arranging along the three equivalent <110> directions.

In this section, we present three different kinds of molecular chains self-assembled with varied annealing temperatures and molecular coverages. While higher temperature (137 °C) brings the emergence of bright molecules in chains and the formation of supramolecular networks, the high molecular concentration leads to the formation of alternating dark-bright molecular chains. This indicates that thermal effects can affect the molecular adsorption geometry and the molecular density has an notable influence on molecular self-assembly structures on metal surfaces.

Until now, we define 4 types of Mn-TPyP molecules arranged in 3 kinds of molecular chains. In principle, the 3 types of dark molecules $\boldsymbol{A}^{++}$, $\boldsymbol{A}^{+}$ and $\boldsymbol{A}$ have high conformational resemblances, and differ by their arrangements and bonding in various molecular chains. For an intuitive impression, table 3.1 shows the bonding infor-

mation for the 4 types of molecular species. The different molecular appearances in STM images could reflect differences of the real molecular conformations and/or electronic properties. To gain more insight into the molecular configurations and arrangements on the surface, NC-AFM measurements are performed.

dark molecules	***A***$^{++}$ type: Cu adatoms on two sides	bright molecule: ***B*** type, no Cu adatoms linked
	A^{+} type: Cu adatom on one side	
	A type: no Cu adatoms linked	

Table 3.1: Bonding information for the three types of dark molecules (***A***$^{++}$, ***A***$^{+}$ and ***A***) and the bright molecules (***B*** type) in chains.

3.3 Conformation Determination of Mn-TPyP Molecules by NC-AFM

We use CO molecule terminated STM/AFM tip for revealing the configurations of Mn-TPyP molecules in mixed phase molecular chains. We simultaneously record the tunneling current and frequency shift images of a mixed phase molecular chain at constant-height mode, i.e. without z feedback. From large tip-sample distances (3.0 Å away from the STM setpoint defined by V = 0.1 V, I = 110 pA), the tip is approached toward the sample with an interval of 0.5 Å and $\Delta f(x, y)$ maps at each chosen height are recorded, and more intense measurements are carried out with the z variation of every 0.1 Å when the short-range force regime is reached (from ΔZ = 1.1 Å to the closest tip-sample distance of ΔZ = 0.5 Å in the measurement series). The CO-functionalized tip changes at ΔZ = 0.4 Å due to strong tip-sample interaction. Twelve Δf images are recorded in this set of measurements, and three representative ones of them are presented in Figure 3.3 b) - d). From the relation between Δf and tip-sample force (Figure 1.5), we know the attractive tip-sample interaction will evolve into repulsive interaction with decrease of the tip-sample distance.

At ΔZ = 1.5 Å (attractive interaction regime), the negative Δf signal has greater absolute values (darker contrast on the scale bar) on the center of dark molecules and also on two sides of the bright molecules (Figure 3.3 b), representing stronger tip-sample attraction [137]. When the tip approaches 0.5 Å more toward the sample and reaches the height of ΔZ = 1.0 Å, a Δf contrast inversion arises for both the dark and bright molecular species. Now the dark molecule center, two pyrrole rings and the peripheral legs of the bright molecules show lighter contrast than the other parts of the two molecular species, indicating repulsive chemical force has began to play a role in the total tip-molecule interaction (Figure 3.3 c). With further decrease

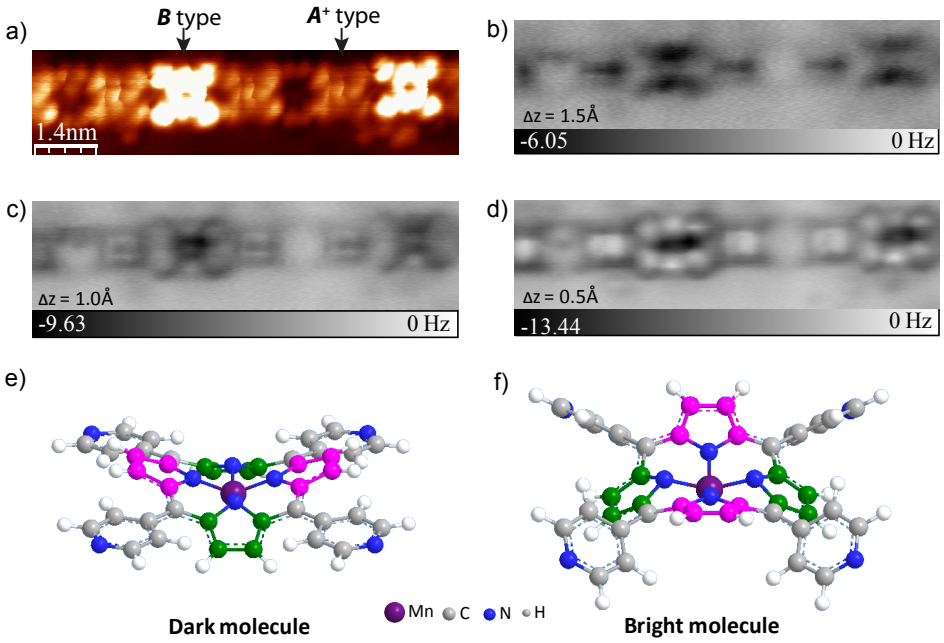

Figure 3.3: High-resolution STM and AFM images for a mixed-phase molecular chain. **a)** is current image and **b)**, **c)** and **d)** are constant-height Δf images at the tip-sample distance ΔZ of 1.5 Å, 1.0 Å and 0.5 Å, respectively. Positive value of ΔZ means the tip is far away from the sample with respect to the STM setpoint defined by V = 0.1 V, I = 110 pA on the Cu(111) surface. The attractive tip-molecule interaction at ΔZ = 1.5 Å goes through its maximum (around ΔZ = 1.0 Å) and changes into repulsive interaction at ΔZ = 0.5 Å. **e)**, **f)** Simple models deduced from the Δf images for the adsorbed dark and bright molecules. The carbon atoms in upward tilted and downward tilted pyrrole rings are colored into pink and green, respectively.

of the tip-molecule distance, the tip-molecule repulsive force dominates and gives rise to intramolecular resolution of both dark and bright molecules. For dark molecules, we just can see two pyrrole ring maxima, indicating flat pyridine legs. In contrast, two pyrrole rings bending upward and four pyridine lobes in upright configuration are revealed for the bright molecules (Figure 3.3 d). The bright molecules have 2-fold symmetry, indicating a notable saddle shape for them. Interestingly, the two pairs of pyrrole rings in dark and bright molecule adopt opposite ways to bend up and down, probably caused by the inter- and intramolecular steric hinderances of these two molecule species. According to these observations, we qualitatively suggest the saddle conformations for dark ($\boldsymbol{A}^+$ type) and bright ($\boldsymbol{B}$ type) molecules, respectively (Figure 3.3 e, f). The pyridine groups in dark molecules are more planar than that in bright molecules. The tilted upwards (α-pyr) and tilted downwards pyrroles (κ-pyr) in both molecular species are represented by distinguished pink and green colors.

For molecular connection in chains, a faint halo feature exists between two dark molecules while a boundary can hardly be defined for the densely packed bright-dark molecule unit (Figure 3.3 d). This indicates the dark molecules in mixed-phase

chains have asymmetric links to one bright molecule without Cu adatom and to one dark molecule via Cu adatoms at each side independently, further supporting the bonding information of $\boldsymbol{A}^{+}$ type molecules given in section 3.2.2.

3.4 Electronic Properties of Molecules in Chains

The electronic structures of molecules in chains are investigated by scanning tunneling spectroscopy. First, we take the spectra on molecules in uniform chains ($\boldsymbol{A}^{++}$ type, Figure 3.4 e). Differential conductance spectra acquired on the molecular center shows a broad resonance centered at 2.7 V, and the pyridine end-groups also have a broad orbital feature similar to the molecular center compared with the dI/dV spectrum of the Cu surface. This means the molecules have a strong hybridization with the substrate. When turning to the mixed phase chains, while the dark molecules ($\boldsymbol{A}^{+}$ type) still show broad peak feature at 2.7 V as the molecules in uniform chains, the bright ones ($\boldsymbol{B}$ type) clearly show three separate peaks in the positive bias range up to 3 V (Figure 3.4 f). These peak are located at 0.4 V, 1.4 V and 2.0 V, respectively. For comparative reason, spectra of molecules in alternating chains are shown in Figure 3.4 g). We can also see a step feature at 0.4 V, and two orbital resonances located at 1.3 V and 2.0 V for bright molecules ($\boldsymbol{B}$ type). The peak at 1.3 V only has high intensity on the bright leg, but the prominent resonance at 2.0 V appears for both the leg and center. In addition, a resonance at 2.8 V is visible for the bright molecule center (magenta color curve). For dark species, a broad orbital feature at 2.6 V can be speculated ($\boldsymbol{A}$ type, cyan color curve). The consistency of dI/dV spectra of bright molecules in mixed phase chains and alternating chains suggests they are the same species. And also, we notice that all the Mn-TPyP molecules do not show effective orbital information at negative bias, as an example given in Figure 3.4 h). There is one peak at V = -1.6 V for all the spectra taken on Cu surface and molecules, thus can not be assigned to molecular property. After identifying the energy alignment of the orbitals for bright and dark molecules, spatial distribution of them is characterized by dI/dV maps.

Simultaneously recorded topography image and dI/dV map at 0.4 V of a mixed phase molecule chains are shown in Figure 3.5 a) and b). In the dI/dV map, while $\boldsymbol{A}^{+}$ type molecules hardly show any notable orbital feature, $\boldsymbol{B}$ type molecule has intensive DOS on two halves with a nodal plane in between, presenting a two-lips shape. Figure 3.5 c) - e) are respective topographies of alternating bright-dark molecule chains acquired at 0.4 V, 1.4 V and 2.0 V, and the corresponding dI/dV maps are presented in Figure 3.5 f) - h). The dI/dV map sequence reveals the spatial distribution for molecular orbitals located at different energies although the STM images looks similar. At 0.4 V, STM topography (Figure 3.5 c) shows that the bright molecules have a fourfold symmetry, but a twofold symmetry exists in the dI/dV map (Figure 3.5 f), similar to that in the mixed phase chain (Figure 3.5 b). High density of state are divided into two equal parts by a gap perpendicular to

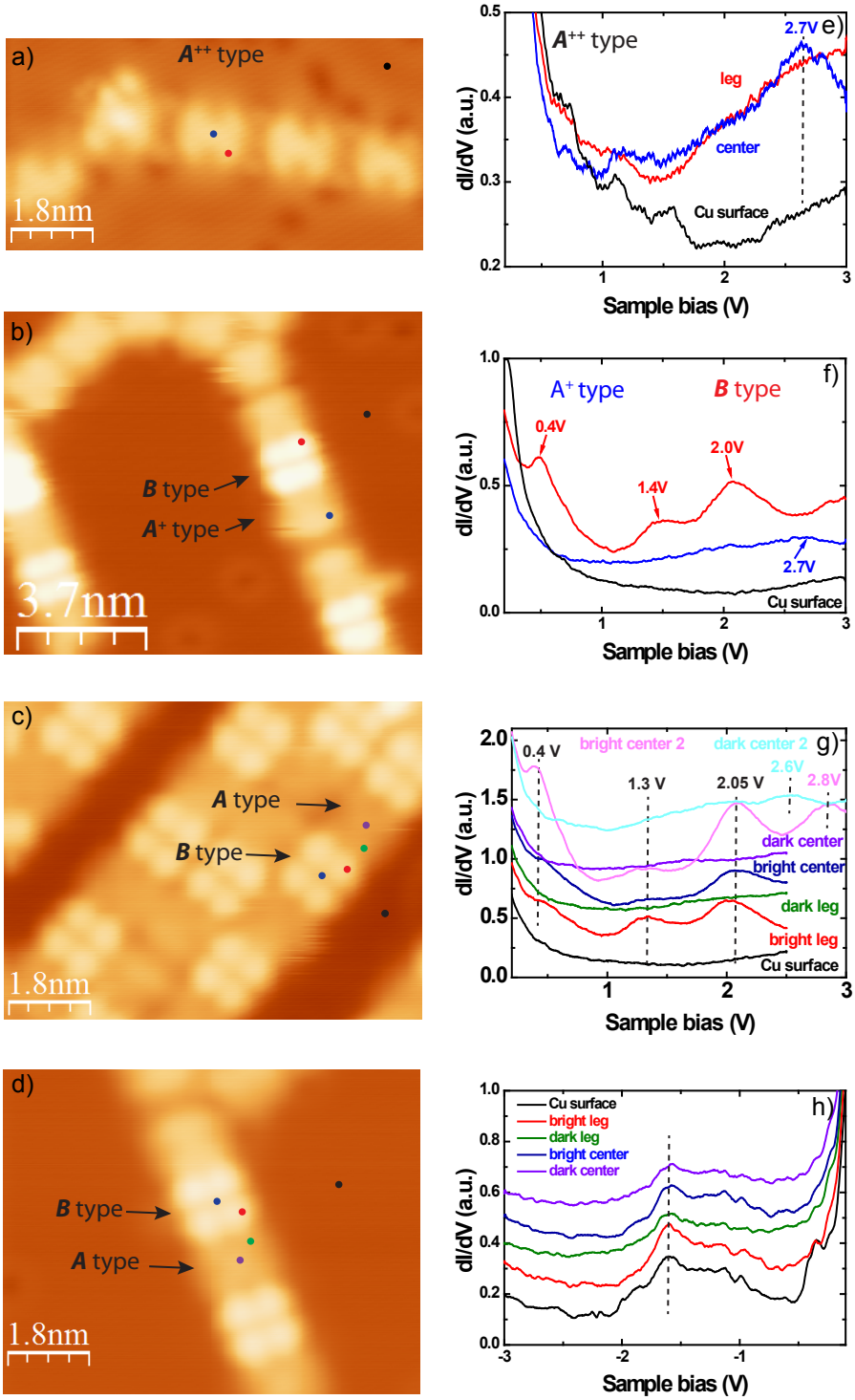

Figure 3.4: dI/dV spectra for molecules in different structures. **a)** single row uniform molecule chains (V = 0.2 V, I = 51 pA). **b)** Single row mixed phase chains (V = 1 V, I = 100 pA). **c)** Multiple row alternating chains (V = 1.0 V, I = 100 pA). **d)** Single row alternating chains (V = 1 V, I = 100 pA). **e) - h)** are dI/dV spectra corresponding to molecules in **a) - d)**, respectively. Two large bias range dI/dV spectra (magenta and cyan color) taken on another bright (***B*** type) and dark molecule (***A*** type) are added in **g)**, and the image of these two molecules for dI/dV spectra measurement is not shown here. STS are taken with a constant current feedback of I = 50 pA.

the chain direction. For the medium energy orbital (V = 1.4 V), a cloverleaf shape can be seen and the DOS mainly localizes on the pyridine end groups of the ***B*** type molecules. At the highest energy (V = 2.0 V), notable protrusions appear at the two pyrrole rings along the chain orientation. In contrast, the other two pyrroles show low intensity of DOS. Albeit bright molecules present various orbital profiles at different energies, dark molecules (***A*** type) show no orbital feature in the inspected bias range. The high similarity in dI/dV map at 0.4 V of the bright molecules in mixed-phase chains and that in alternating chains further evidences that there is only one bright molecule species in our measurement (i. e. ***B*** type molecule).

The drastically different electronic properties of bright Mn-TPyP molecules (***B*** type) and other three dark molecular species implies different molecule-substrate hybridization for them. The bright molecules show notable orbital resonances, indicating relatively weaker coupling with the Cu surface compared with the dark molecule species, whose orbitals are broadened considerably by the substrate. This is in line with the AFM-resolved adsorption geometries of bright and dark molecules in mixed phase chains, i.e. bright molecules are more decoupled from the surface (Figure 3.3). On the other hand, Cu-pyridine coordination bond could also affect the molecular electronic states of Mn-TPyP molecules, either by shifting the molecular orbitals in energy scales or inducing new combined orbitals based on the electronic states of metal adatoms and molecules [133]. Due to the strong hybridization between the $\boldsymbol{A}^{++}$, $\boldsymbol{A}^{+}$ and ***A*** type molecules and the Cu surface, which dominates the molecular electronic structures and only gives rise to a broad orbital resonances around 2.7 V, the influences of metal-ligand coordination bonds on the molecular orbitals are smeared out although the 3 dark molecular species differ in coordination with Cu adatoms.

3.5 Irreversible and Reversible Rotation of Pyridine Groups in Molecules

Mn-TPyP molecules ($\boldsymbol{A}^{++}$ type) in Cu-coordinated uniform chains can be manipulated by a STM tip (Figure 3.6). When holding the tip on a molecular leg and ramping the bias from 0.2 V up to 3.0 V, a sharp jump happens for the topography (Δz = 0.45 Å) and dI/dV channels at sample bias of 2.6 V, indicating a change of the molecule. This is confirmed by the posterior imaging of the same region. The contrast of the addressed molecule is partially altered, i.e. one half is brighter than the other. Moreover, a new resonance peak at 2.0 V arises for the bright lobes compared to dark ones. Since the bright half in the modified molecule has similar appearance and same orbital resonance at V = 2.0 V as the intact bright molecules, it is expected that the change in the molecule is related to the pyridine rotation, from a flat geometry to a metastable state with bigger tilted dihedral angle with respect to the macrocycle plane, thus decoupled from the substrate. We also note that the dI/dV spectrum on the unchanged pyridine legs is not affected. The addressed

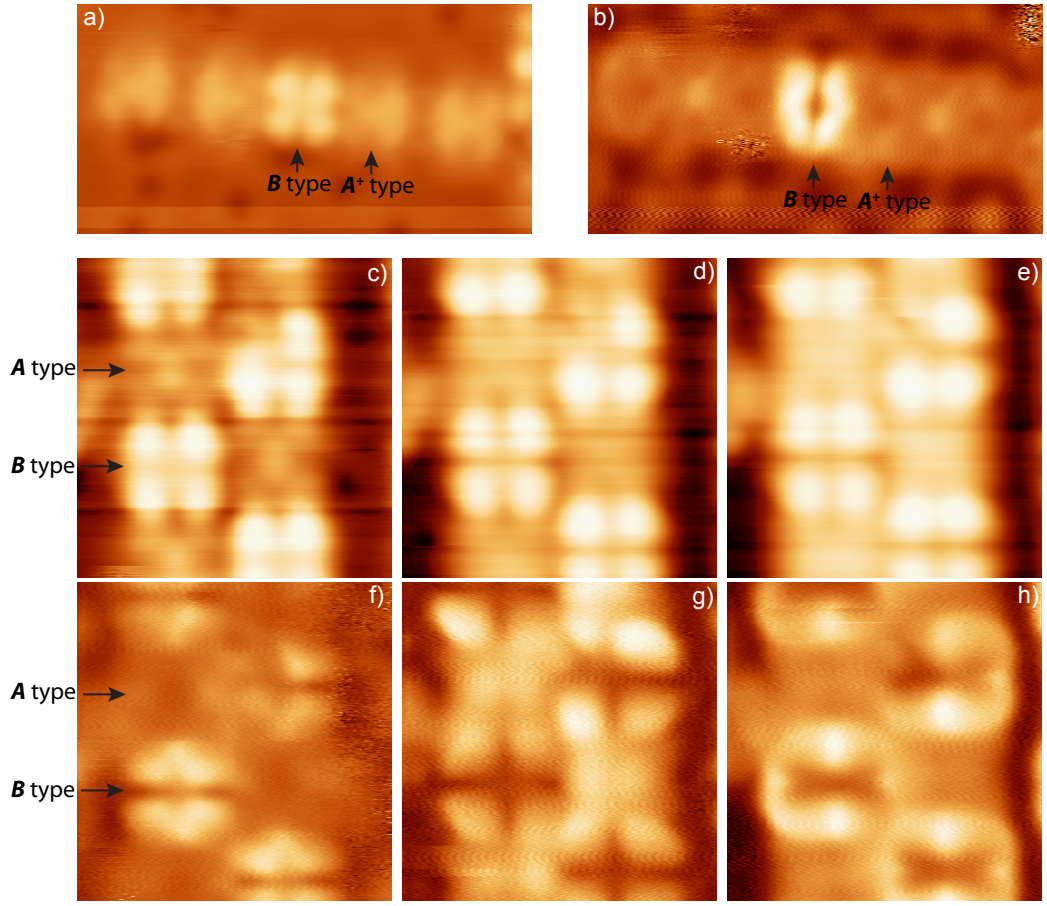

Figure 3.5: a) STM topography and **b)** dI/dV map of a mixed phase molecule chain at 0.4 V, recorded with a feedback of I = 0.25 nA. **c)**, **d)**, **e)** Respective STM topographies and **f)**, **g)**, **h)** dI/dV maps of alternating molecule chains recorded at 0.4 V, 1.4 V and 2.0 V, with feedback of I = 0.2 nA.

molecule with two upright rotated pyridine lobes represents the intermediate state and evidences the activation of an intramolecular degree of freedom [138]. With a medium current feedback of 0.2 nA, the sample biases for activating intramolecular rotation with different tips on different molecules during bias sweeping from 0.2 V to 3.0 V are listed in Figure 3.6 e) , which gives a lowest bias of 2.0 V.

The movement of pyridine rings can also be stimulated by a constant bias and current with open feedback loop (Figure 3.6 f). The current is tracked as function of time, and an abrupt change occurs for the conductance at a certain moment and can be assigned to the conformation rearrangement of the molecule sandwiched in the junction (V = 2.5 V, I = 0.3 nA). We calculate the number of electrons necessary to induce a single molecular motion (translation, rotation), and obtain statistic data for tens of events occurred for different molecules with various tips [139]. The data is fitted by an exponential function $y = A \cdot exp(-x/t) + y_0$ (A and y_0 are constants, and t is the decay constant), giving rise to a rough reaction yield Y_R (Y_R is the

inverse of the decay constant t) of 6.08×10^{-11} events/electron for this manipulation process with V = 2.5 V and I = 0.3 nA (Figure 3.6 g).

Different sample biases of both polarities and varied magnitude of currents with open or closed feedback loop are used to stimulate down-rotation of the pyridine rings after their up-rotation from the intact conformation, but this usually results into various molecular configurations or dissociation. This irreversible rotation process is reasonable if we take the complex chemical environment of this specific metal-organic chains into account. On one hand, the flexible porphyrin molecules have a large variety of freedom, which can couple to tunneling electrons and lead to different metastable molecule configurations. Also, when the pyridine legs go upright, the metal-ligand coordination bonds are broken and has little chance to recover to the intact geometry since the Cu adatoms may have movements on the surface during the pyridine rotation motion.

Conformational changes of the molecules in alternating dark-bright molecule chains can also be induced by the STM tip. For bright molecules (***B*** type), the upright pyridine rings can go down to a more flat geometry with the sample bias more than 2.0 V (Figure 3.7). For backward dI/dV curve in Figure 3.7 b), the resonance peak at 2.0 V is drastically broadened with low intensity due to the down-rotation and thus the strong hybridization with the metal surface. The dI/dV spectra taken on upright and planar pyridine rings demonstrate a strong contrast for the molecular orbital located at 2.0 V. The down-rotation behavior of the pyridine rings in bright molecules is also irreversible.

For the dark molecules (***A*** type) sandwiched by two bright molecules in the alternating chains, a reversible rotation process of the pyridine groups has been observed. We fix the STM tip on one pyridine leg of a dark molecule in the chain, and sweep the sample bias from 0.2 V to 3.0 V and back to 0.2 V (Figure 3.8 a). The dI/dV signal tracking this manipulation process shows a deviation between forward and backward spectrum (Figure 3.8 d). Then we scan the same molecular chain and find that two pyridine rings rotate up (Figure 3.8 b). In order to test interconversion possibility between these two conformers, the same bias sweeping is carried out again. Different line-shape of the forward and backward dI/dV curves are recorded (Figure 3.8 e). The final STM image after the whole manipulation series depicts that the two upright pyridine lobes go down (Figure 3.8 c). Superposition and overlap of the differential conductance spectra during the rotation up and down process supports it is a completely reversible process (Figure 3.8 f). It is notable that the dI/dV spectrum of the rotated up pyridines in the ***A*** type molecules is different from that of the altered part in the $\boldsymbol{A}^{++}$ type molecules showing a prominent resonance peak at V = 2.0 V (Figure 3.6 d), probably due to the distinguished local physiochemical environments for them. The orbital feature of the ***A*** type molecule with two up-rotated pyridine rings is unlike that of the intact bright molecules (***B*** type). An intuitive impression of the dark molecule without or with the two upright pyridine groups can be given by the scheme (Figure 3.8 g and h).

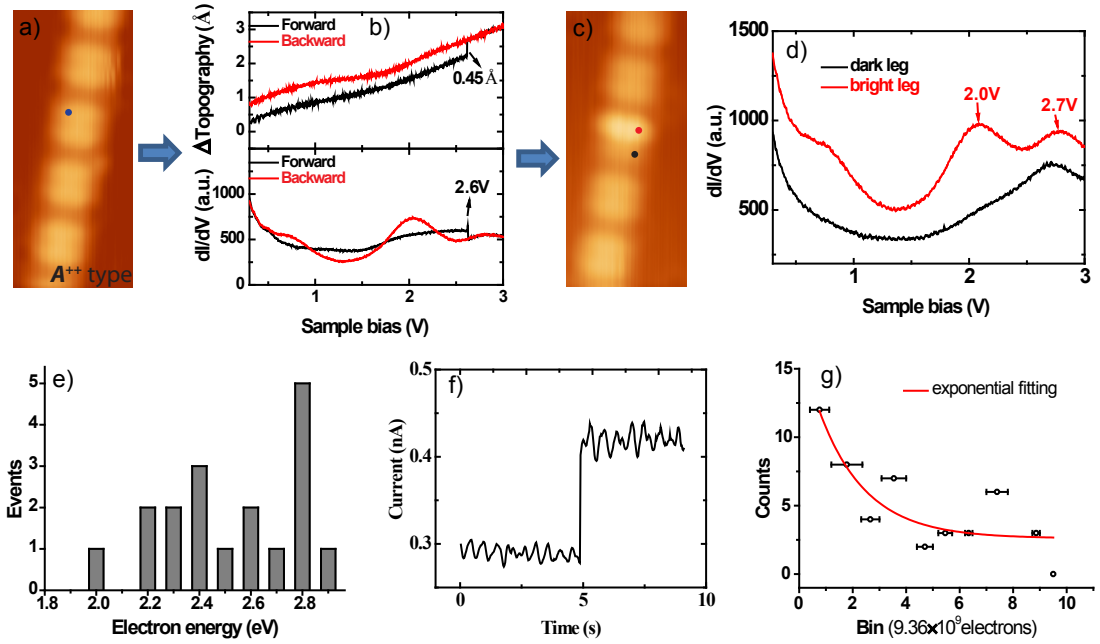

Figure 3.6: Rotation of pyridine legs in Cu-coordinated uniform molecules (A^{++} type). **a)** STM image of an intact molecule chain before and **c)** after ramping the bias to 3 V (V = 1 V, I = 110 pA). **b)** Topography and dI/dV spectra during the manipulation process with feedback on (setpoint: V = 0.2 V, I = 0.2 nA). **d)** dI/dV spectra acquired on the intact and rotated pyridine legs with feedback on (setpoint: V = 0.2 V, I = 0.2 nA). **e)** Lowest electron energy needed to induce pyridine rotation. The electron energy are statistically probed by fixing the STM tip above a molecule with sample bias of 0.2 V, and ramping the bias to 3 V, then sweeping the bias down to 0.2 V again (a constant current feedback of 0.2 nA is applied during the manipulation). A sudden jump for topography and dI/dV curve reveals the occurrence of a reaction. The panel shows the distribution of electron energy (eV) reached when the reaction occurs. **f)** Current trace for the molecule (V = 2.5 V, I = 0.3 nA). The current jump shows when the rotation occurs and the area under the current pulse gives the number of electrons (n_e) used. **g)** The binned distribution of n_e (V = 2.5 V, I = 0.3 nA), fitted by an exponential function. The error bars represent the largest deviations from the average values in the bins.

The basic reason enabling the interconversion of pyridine legs between two metastable tilting angles could be the competition of bonding of pyridine to Cu via the N lone pair to interaction between substrate and π electrons of the aromatic ring [140]. As the first stage of the ring disruption reaction of pyridine molecules on the Cu(100) surface, the adsorption orientation change from perpendicular into parallel to the surface has to overcome an adiabatic barrier of 0.5 eV [141], which is much lower than the tunneling electron energy used in our STM-experiment for inducing the pyridine rotation in Mn-TPyP on Cu(111) surface.

We also attempt to use negative sample biases with high current (up to -3 V and 3 nA) for inducing rotation of the pyridine legs, but it is not successful. Therefore, the excitation of intramolecular motion should not be caused by a pure electric-

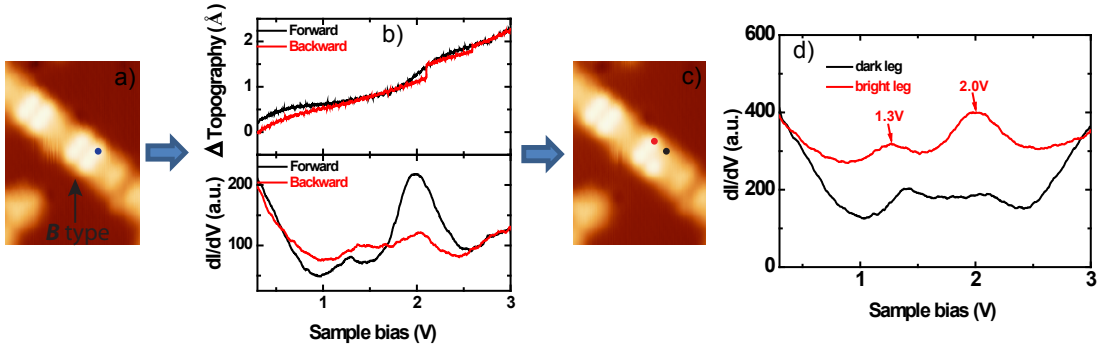

Figure 3.7: Rotation of pyridine legs of bright molecules (***B*** type) in alternative Mn-TPyP chains. **a)** STM image of an intact molecule chain before and **c)** after ramping the bias to 3 V (setpoint: V = 1 V, I = 110 pA). **b)** Topography and dI/dV spectra during the manipulation process with feedback on (setpoint: V = 0.2 V, I = 50 pA). **d)** dI/dV spectra acquired on the intact and changed pyridine legs with feedback on (setpoint: V = 0.2 V, I = 0.2 nA).

field effect. We note that the lowest voltage V = 2.0 V for inducing the rotation of pyridine groups in dark molecules resembles the onset energy of the broad resonance around 2.7 V with a high occurrence possibility (Figure 3.6 e), which suggests the intramolecular freedom activation is probably related to the resonant tunneling of electrons through the orbitals located at 2.7 V for dark molecules [142], [143].

3.6 Conclusion

In this chapter, we investigate Mn-TPyP on Cu(111) surface by a combined STM/AFM method. Mn-TPyP self-assemble into linear chains along the <110> direction on copper, reflecting a substrate template effect for molecular growth. Moreover, molecules show adaption of their conformations and bonding in response to different annealing temperatures and molecular coverages on the surface. The single row uniform chains consist of $\boldsymbol{A}^{++}$ type molecules. The single row mixed phase chains are composed of irregularly arranged dark ($\boldsymbol{A}^{+}$ type) and bright ($\boldsymbol{B}$ type) molecules, which change into alternating chains with densely packed dark ($\boldsymbol{A}$) and bright ($\boldsymbol{B}$ type) molecules with increasing molecular density on the surface probably due to deficiency of Cu adatoms. The three dark molecular species ($\boldsymbol{A}^{++}$, $\boldsymbol{A}^{+}$ type and $\boldsymbol{A}$ type) have high conformational resemblances but differ by their bonding in the chains. While the $\boldsymbol{A}^{++}$ and $\boldsymbol{A}^{+}$ type molecules are coordinated by Cu adatoms on two sides and one side, respectively, $\boldsymbol{A}$ type molecules are not connected by adatoms.

The bright molecules ($\boldsymbol{B}$ type) in chains exhibit notable saddle shape as indicated by AFM and dI/dV maps. Bright molecules with upright pyridine legs show notable orbital resonances evidencing a weaker electronic coupling to surface than dark molecules, which are strongly coupled to the Cu surface. Self-assembled molecules also show conformational flexibilities, embodied by the rotational freedom of pyri-

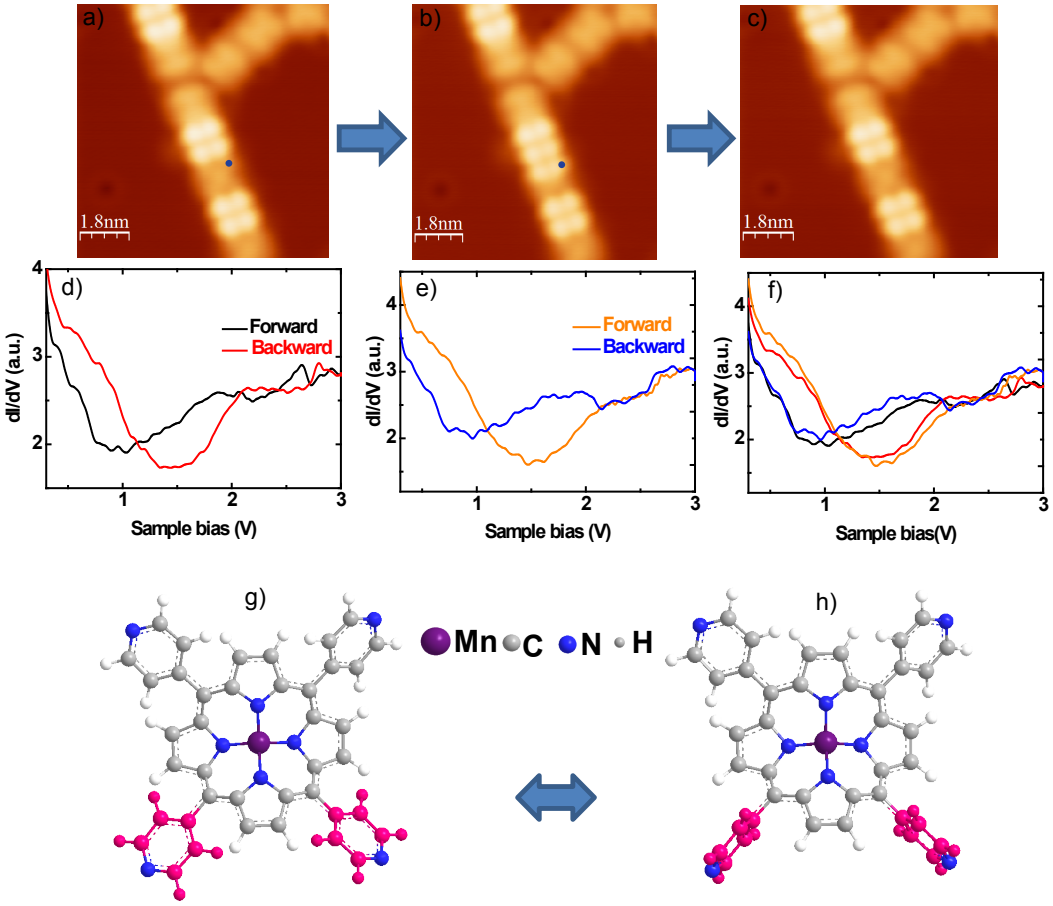

Figure 3.8: Reversible rotation of pyridine legs of dark molecules (***A*** type) in alternative chains. STM image of a molecular chain before **a)**, after one time **b)** or two times **c)** of bias sweeping (V = 1 V, I = 0.1 nA). **d)**, **e)** dI/dV spectra during the bias sweeping with feedback on (setpoint: V = 0.1 V, I = 50 pA). **f)** Superposition of the dI/dV spectra in **d)** and **e)**. **g)**, **h)** scheme of molecular conformations for dark molecule without or with upright pyridine legs.

dine functional groups activated by tunneling electrons carrying energy more than 2 eV. In uniform chains, pyridine rings of $\boldsymbol{A}^{++}$ type molecules can be rotated upwards by voltage ramps. In alternating chains, pyridine rings of bright molecules (***B*** type) can be rotated down and dark molecules (***A*** type) can be rotated reversibly by voltage ramps. The probable mechanism to induce the pyridine rotation could be related to the resonant tunneling of electrons through the molecular orbital located around 2.7 V.

4 Tip-Molecule Interaction Induced Changes for the Magnetic Properties of FeOEP-Cl and FeOEP Molecules on Au(111)

4.1 Introduction

Metalloporphyrin containing central transition metal atoms (Fe, Co, Ni), which can bear various spin configurations, have been studied intensively in recent years [144], [145], [146]. Characterizing and controlling the magnetic properties of metalloporphyrins is a crucial aspect for the future application in spintronics. The spin crossover of metalloporphyrin molecules can be accessed by different physical sources like light [147], pressure [148], magnetic field and molecule-substrate coupling [149]. Except these external stimulus, an atomic point contact between a STM tip and molecules can also tune their magnetic state. For instance, while the magnetocrystalline anisotropy of iron octaethylporphyrin chloride (FeOEP-Cl) molecules on Pb(111) surface shifts to higher energies with decreased tip-sample distance [32], the iron octaethylporphyrin (FeOEP) molecules show a slight increase and then a rapid decrease of their anisotropy energy with proximity of a Pb tip [150]. These observations imply that manipulation of the magnetic state by a STM tip strongly depends on the local configurations of the tip-molecule junctions.

Combined STM/AFM measurements provides an unique chance to probe the conductance and the short-range force between an atomically sharp tip and well defined adsorbates on surfaces [151]. Here we report a detailed experimental analysis about the correlation between the magnetic property and the chemical force in a Au tip - FeOEP-Cl junction and a Cl functionalized tip - FeOEP junction on Au(111) surface. Changes for the magnetic property of FeOEPs contacted by Au tips and Xe tips are also demonstrated.

In addition to the magnetic state manipulation of the surface-anchored FeOEP molecules by an adjacent Cl functionlized tip, their magnetism transformation was also realized by the intramolecular ring-closure reactions of their organic ligand

[152]. Although the chemical configurations of the stepwise reacted products were identified by STM images and spectroscopies, we use the NC-AFM for resolving the real structure of the final product from this series of reactions, which can provide intramolecular resolution [153].

Experimental results in this chapter are divided into four parts. While section 4.2 gives a simple description about the properties of FeOEP-Cl in gas phase, section 4.3 presents the self-assembly and magnetic properties of FeOEP-Cl and FeOEP molecules on Au(111) surface. In section 4.4, tip-molecule interaction induced modifications of the magnetic properties of FeOEP-Cl and FeOEP molecules are demonstrated, respectively. After that, AFM resolved chemical structure of the iron tetrabenzoporphyrin molecules is depicted in section 4.5.

4.2 Properties of FeOEP-Cl and FeOEP in Gas Phase

The chemical structure of iron octaethylporphyrin chloride (FeOEP-Cl) molecule is illustrated in Figure 4.1. Four interconnected pyrrole rings linked to the central Fe atom via Fe-N bonds, constitute the porphyrin macrocycle. The outside species consists of eight ethyl groups bonded to the peripheral carbon atoms in the four pyrrole rings. An extra chlorine ligand is coordinated to the central Fe atom.

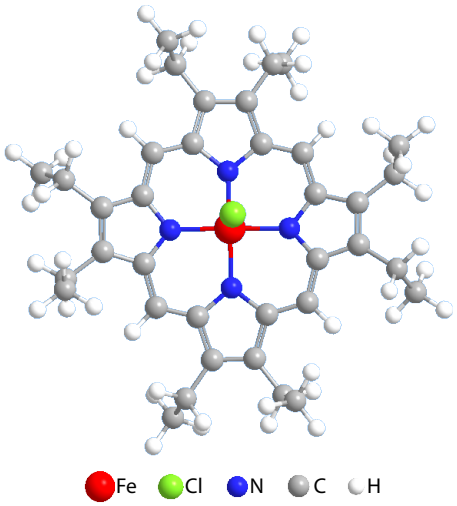

Figure 4.1: Chemical model of FeOEP-Cl. Fe, Cl, N, C and H are colored as red, green, blue, gray and white, respectively.

For FeOEP-Cl molecules in gas phase [31], their Fe center has a +3 oxidation state with a total spin of S = 5/2 (five valence electrons) and an in-plane anisotropy (anisotropy parameter $D > 0$) in a square-pyramidal ligand field. For the case of

FeOEP, it has a +2 oxidation state and six d-orbital electrons which present an intermediate spin state of S = 1 in a square planar ligand field.

The zero field splitting of FeOEP-Cl and FeOEP are shown in Figure 4.2. d orbital degeneracies of the two molecular species are lifted up by their ligand field. The FeOEP-Cl $|\pm 1/2\rangle \rightarrow |\pm 3/2\rangle$ excitations has an energy change of $2D$ and that for the $|\pm 3/2\rangle \rightarrow |\pm 5/2\rangle$ is $4D$. For FeOEP the excitation energy for $|0\rangle \rightarrow |\pm 1\rangle$ is D and in addition, the rhombicity in the ligand field splits the $|\pm 1\rangle$ by $2E$.

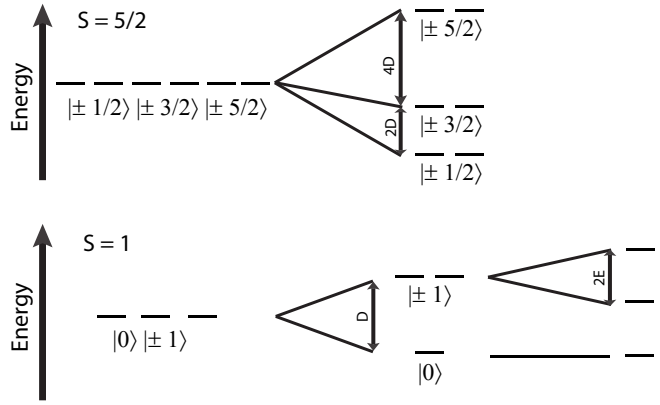

Figure 4.2: Zero field splitting for the FeOEP-Cl (high spin state S = 5/2) and FeOEP (intermediate spin state S = 1).

4.3 Properties of FeOEP-Cl and FeOEP on Au(111)

4.3.1 Self-Assembly of FeOEP-Cl on Au(111)

When adsorbed on Au(111) surface at room temperature, the FeOEP-Cl molecules self-assemble into densely packed islands with quasi-hexagonal structure (Figure 4.3 a). The majority of the molecules ($> 80\%$) appear with a central protrusion, while a few molecules showing a depression at the center, indicating the loss of the Cl ligand due to evaporation or diffusion on the surface. Therefore, these two molecular species correspond to FeOEP-Cl and FeOEP, respectively. As shown in Figure 4.3 b), a dim ring around the bright Cl atom in the center of the FeOEP-Cl molecules indicates a planar porphyrin macrocycle and upright Cl ligand [152]. In order to achieve intramolecular contrast, we prepare a Cl fuctionalized tip for imaging by approaching the Au tip toward the Cl ligand and picking it up [154]. As we can see, the spatial resolution in Figure 4.3 c) is drastically enhanced by the Cl tip compared to Figure 4.3 b). The apparent size of the Cl atoms shrinks and apparent height of them increases by 300 pm (V = 53 mV, I = 52 pA). A 4-fold symmetric configuration of the FeOEP-Cl molecule is resolved and the peripheral

eight ethyl groups can be ambiguously discerned (A molecular model is overlaid as guide for the eye in Figure 4.3 c).

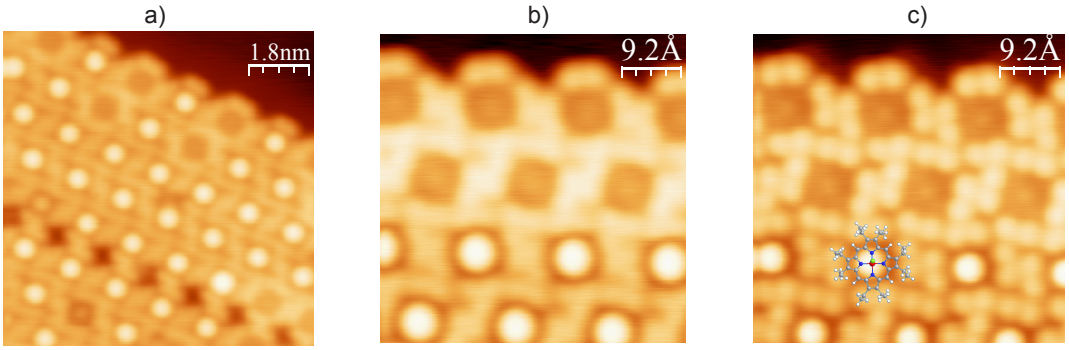

Figure 4.3: Chemical structure and STM topography of FeOEP-Cl on Au(111). **a)** An overview image of FeOEP-Cl island recorded with a Au tip (V = 1 V, I = 200 pA). **b)** and **c)** are high-resolution images of FeOEP-Cl island scanned by a Au tip and a Cl atom-terminated tip, respectively (V = 53 mV, I = 52 pA).

4.3.2 Magnetic Properties of FeOEP-Cl and FeOEP on Au(111)

For metalloporphyrins adsorbed on metal surfaces, the molecule-surface interaction may alter the molecular spin state and make it different from that in the gas phase, which is crucial for spin controlling and manipulation. Studies by Olof Peters and co-workers on FeOEP-Cl and FeOEP system at a temperature of 1.2 K have revealed inelastic spin excitation as shown in Figure 4.4 [155]. While FeOEP-Cl exhibits symmetric steps centered at V = $\pm(1.46 \pm 0.10)$ mV, FeOEP shows asymmetric line shape with higher differential conductance at negative bias side. These spectroscopic features provide information about the spin states of the two molecular species.

Previous studies claimed that FeOEP-Cl adsorbed on Au(111) and Pb(111) both adopt a high total spin S = 5/2 and in-plane magnetic anisotropy manifested by inelastic spin flip excitation on differential conductance curves [152], [32]. Furthermore, same axial anisotropy constant $D = 0.7$ meV for FeOEP-Cl was obtained on both substrates. Therefore, the symmetric steplike features for FeOEP-Cl spectrum is ascribed to $|\pm 1/2\rangle \rightarrow |\pm 3/2\rangle$ spin excitations. Albeit FeOEP-Cl molecules have degenerate spin ground state of $S_z = \pm 1/2$, no feature of Kondo screening is visible in dI/dV spectrum. The absence of Kondo effect was ascribed to the increased Fe-surface distance compared to single transition metal atoms [108], [107] or planar Fe phthalocyanine molecules [156], [157]. The axial Cl ligand slightly pulls the Fe atom out of the macrocycle plane and thus minimizes the Fe-surface coupling.

By removing the Cl ligand, the nominal oxidation state of Fe atom is expected to reduce from +3 to +2 and the Fe atom also relaxes into the molecular plane, thereby

decreasing the Fe-surface distance and enhancing molecule-substrate hybridization. The asymmetric dI/dV line profile agrees with the S = 1 intermediate spin state [31], [158], probably reflecting a competition between the magnetic anisotropy of the molecule and the Kondo screening with the conduction electrons [152]. This competetion is anticipated for magnetic centers with spin states S > 1/2 in an anisotropic environment, where the energy scale of the anisotropy and Kondo effect are comparable [159]. For FeOEP adsorbed on Pb(111), D = 10.6 meV and E = 0.7 meV were extracted directly from the dI/dV spectrum [150].

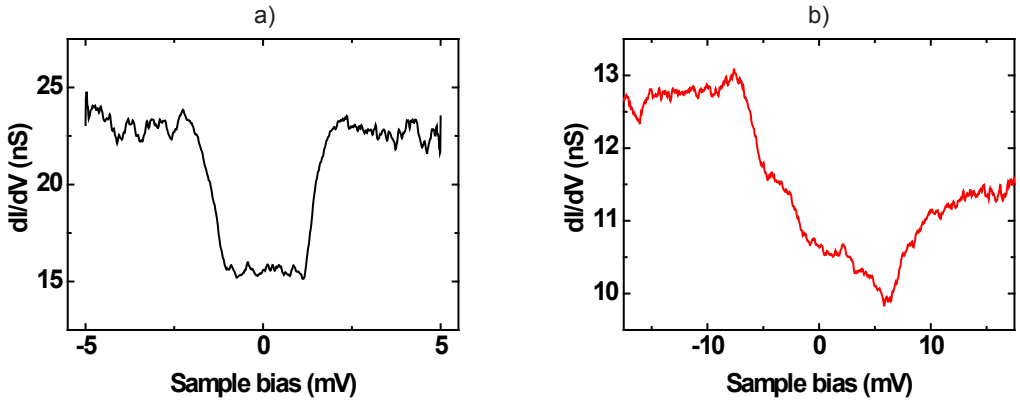

Figure 4.4: dI/dV spectra of FeOEP-Cl and FeOEP recorded by a Au tip at 1.2 K. **a)** Two steps at V = $\pm(1.46\pm0.10)$ mV in the conductance (V = 5 mV, I = 100 pA, lock-in modulation 50 μV; **b)** Asymmetric shape with a dip around the Fermi energy. The dip is sandwiched by two steps located at $\pm$6 mV (V = 25 mV, I = 300 pA, lock-in modulation 100 μV). Figures are adapted from Olof Peters' master thesis [155].

4.4 STM/AFM tip Induced Modification of Ligand Field and Magnetic Properties of FeOEP-Cl and FeOEP on Au(111)

4.4.1 Force and Conductance between a Au Tip and FeOEP-Cl Molecules

As mentioned above, dI/dV spectra of FeOEP-Cl molecules show two steps symmetric to E_F at normal tunneling conditions (V = 50 mV, I = 200 pA). However, when the Au atoms covered tip is brought close to the Cl ligand, a new peak centered at Fermi energy appears with the up-shifted symmetric step features in energy scale (Figure 4.5 a, adapted from Olof Peters' master thesis [155]). This peak is splitted in a magnetic field and ascribed to Kondo resonance with ground state of $S_z = \pm 1/2$ for FeOEP-Cl [155]. In this way, the tip-sample interaction induces a Kondo effect for FeOEP-Cl molecules and also changes their magnetic anisotropy, due to the modified square pyramidal ligand field of Fe atom with proximity of Au

tip to FeOEP-Cl molecules shown in Figure 4.5 b) [150]. This provides a unique method to consecutively control the magnetic properties of adsorbed molecules on metal surface. To gain a deeper insight into this process, we characterize the tip-molecule system by a combined STM and AFM method, which allows us to obtain both the information of tip-molecule force and conductance at varied tip-molecule distances.

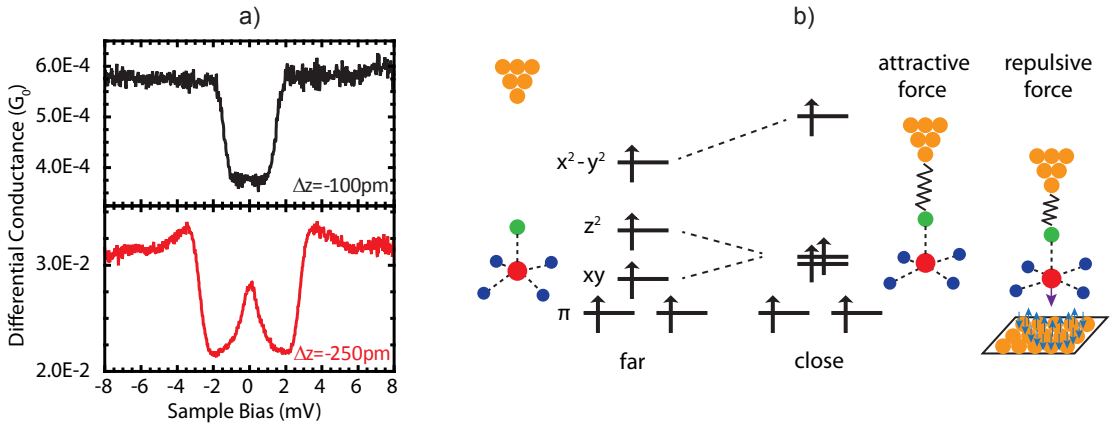

Figure 4.5: Distinguished dI/dV spectra and ligand field splitting for the FeOEP-Cl molecules at different Au tip-sample distances. **a)** Top panel: steplike feature when the tip approaches by 100 pm toward the Fe atom from the tunneling setpoint; bottom panel: a new peak arising when further decreasing the tip-sample distance by 150 pm. Setpoint is defined by V = 50 mV, I = 200 pA, and dI/dV spectra are taken at 1.2 K and with a lock-in modulation of 50 μV. Figures are adapted from Olof Peters' master thesis [155]. Conductances are given in unit of the single-channel, spin-degenerate quantum of conductance $G_0 = 2e^2/h$ = 77.5 μS, where e is the elementary charge and h is the Planck constant. **b)** Change of the ligand field splitting for FeOEP-Cl molecules by tip-sample interaction and Kondo screening of the Fe atom by the substrate electrons. Fe, N and Cl atoms are colored into red, blue and green, respectively.

The short-range force induced by a Au tip on a FeOEP-Cl molecule is estimated by using the force between the tip and the FeOEP-Cl/Au subtracting the tip-surface force when the tip is off the molecule (Figure 4.6 a). As the periodically oscillating Au tip approaches from the displacement of 10 Å above the STM setpoint (defined by V = 50 mV, I = 50 pA) toward the Au surface and FeOEP-Cl molecule by 3 Å and 3.4 Å respectively (red and green spots in Figure 4.6 b), frequency shift and tunneling current as function of the tip-sample distance are recorded (Figure 4.6 c). Retraction of the tip by 10 Å as the initial position of the approching measurement is for keeping the tip out of tunneling regime and minimizing the long-range tip-sample interaction (Van der Waals force and electrostatic force). While the Δf signal throughout the approach of the Au tip on the Au surface is negative with a minimum value of -9.7 Hz, it goes through the negative value region with a minimum of -47 Hz at ΔZ = -1.5 Å and enters the positive value region for the same Au tip approaching on a FeOEP-Cl molecule. The average current for Au tip on FeOEP-Cl molecule is converted into its corresponding conductance by dividing the sample

bias (here is 15 mV). The flat feature in the section of 7.5 Å > ΔZ > -0.89 Å in the conductance curve reflects the background noise level since too few electrons tunnel through the junction at such large tip-sample distance. Subsequently, we extract the force from Δf curve by deconvoluting the tip oscillation according to the Sader-Jarvis formalism (equation 1.13) [64]. For force deconvolution, the tip height on the Au surface is shifted by -231 pm with respect to that on the FeOEP-Cl molecule defined by the same setpoint of V = 50 mV, I = 50 pA. Likewise, instantaneous conductance is also calculated by removing the smearing induced by the tip oscillation with the Sader-Sugimoto method [160]:

$$i(z) = i_{av}(z+a) - \int_z^{\infty} \sqrt{\frac{2a}{\tau - z}} \left[\frac{di_{av}(\tau)}{d\tau} - \sqrt{\frac{2}{\pi}} \frac{di_{av}(\tau + a)}{d\tau} \right] d\tau \tag{4.1}$$

where i_{av} is the average tunneling current and a is the oscillation amplitude.

As one can see, the short-range force between the Au tip and the FeOEP-Cl reaches a minimum of -831 pN at ΔZ = -1.26 Å, and it increases to less negative values with the further reduced tip-molecule distance and finally becomes positive for ΔZ < -2.6 Å (Figure 4.6 d). That is, strong attractive tip-sample force evolves into repulsive force with the tip approach. The minimum in the force curve represents the maximal attractive interaction between the Au tip and the FeOEP-Cl molecule.

The deconvoluted conductance is plotted at a logarithmic scale, which has distinct slopes at different tip-molecule distances (Figure 4.6 e). Four characteristic regimes with label I, II, III and IV can be distinguished. In regime I (-1.0 Å > ΔZ > -1.54 Å), the conductance increases exponentially for more than one order of magnitude from $10^{-3}G_0$ to $\approx 0.017G_0$, consistent with the behavior of electron tunneling through the junction. A conductance increase by a factor of 2 to $\approx 0.037G_0$ occurs within a tip displacement interval of ≈ 0.7 Å for regime II. In regime III (-2.25 Å > ΔZ > -2.65 Å), the conductance increases from $\approx 0.037G_0$ to a maximum of $\approx 0.2G_0$ at an exponential scale. According to the previously proposed scenario for a STM tip or a oscillating STM/AFM tip contacting with atoms or molecules on surfaces [161], [162], [163], we attribute these three tip displacement sections to tunneling regime, tunneling-contact transition regime and contact regime successively. The tip-molecule contact point, defined by the intersection of linear fits in the transition and contact regimes (indicated by the vertical green line in Figure 4.6 e) [163], is located at ΔZ = -2.25 Å and corresponds to a force value of -331 pN. In regime IV, the conductance begins to decrease rapidly and reaches $\approx 0.09G_0$ at ΔZ = -3.4 Å. One should note the concurrence of conductance maximum and repulsive force kink of 185 N at ΔZ = -2.76 Å, suggesting a probable geometrical rearrangement of the junction (i.e. the tip is prone to pick up or desorb the Cl ligand from the FeOEP-Cl with even smaller tip-molecule distance). It is notable that the tip-molecule contact does not significantly increase the excitation signal of the tuning fork which varies only between 12 - 22.5 meV per oscillation cycle (Figure 4.6 f), which is very small compared to the Au tip-molecule bonding energy of ≈ 705 meV at the tip-molecule

contact point of ΔZ = -2.25 Å (the bonding energy is obtained by integration of the short-range force over the approach distance and not shown here). The spikes on the excitation signal could stem from geometric relaxations and bond formations for building the tip-molecule contact.

For the addressed FeOEP-Cl molecule in Figure 4.6, we take dI/dV spectra in the tip-molecule distance range from ΔZ = -2.6 Å to ΔZ = -3.4 Å with an interval of 0.2 Å relative to the predefined height (no measurement is carried out beyond this distance range). For all the acquired five spectra shown in Figure 4.6 g), a zero-bias peak is visible. Based on the dI/dV spectra taken at 1.2 K by Olof Peters, we suggest the zero-bias peak as a Kondo resonance. The intrinsic width Γ_K of the zero-bias peak given by a Fano function (equation 2.11) fitting of the dI/dV spectra taken at -2.6 Å, -2.8 Å and -3.0 Å is about 11.8 mV, which decreases to 8.1 mV for the dI/dV curves recorded at -3.2 Å and -3.4 Å due to increased intensity of the peak (the Fano function fitting is not shown [1]). Compared to the dI/dV spectrum measured at 1.2 K (Figure 4.5 a), the dI/dV spectra taken at 7.2 K without showing the inelastic step feature is notably broadened by the temperature.

Tip-sample force at ΔZ = -2.6 Å is -2.3 pN, which shifts to positive value with further decreased distance. In other words, Fe atom is Kondo screened by the itinerant electrons of the surface when repulsive short-range force between the Au tip and FeOEP-Cl dominates. We find a difference for the absolute force values obtained by the same Au tip approaching on different FeOEP-Cl molecules, but the evolution trend of tip-molecule force from attractive to repulsive with the stepwise reduced tip-molecule distance is the same.

In comparison with the STM study of Pb tip induced magnetic anisotropy changes of FeOEP-Cl molecules on the Pb(111) surface [32], [150], we can correlate the Au tip-molecule interaction to the magnetic property evolution of FeOEP-Cl on Au(111). In attractive tip-Cl force regime, the Cl atom moves toward the tip. Conversely, the Cl-Fe bond elongates and the Fe atom relaxes toward the molecular plane [150]. When further shortening tip-sample distance and repulsive tip-Cl force arising, the Cl ligand is pushed down toward the underneath Fe ion, which gets closer and closer to the Au surface and reinforces its hybridization with the surface. The enhanced coupling between the Fe atom and Au surface gives rise to the Kondo screening (sketch at right side of Figure 4.5 b). However, the Fe atom is not lower than the molecular plane since the Au tip mainly has interaction with the Cl ligand. The geometric rearrangement of the tip-molecule-surface junction has two main effects on the molecular magnetic property: (i) enhancement of the Kondo scattering between Fe atom and conduction electrons, giving rise to higher Kondo temperature; (ii) increasing the overall ligand field splitting and magnetocrystalline anisotropy [150]. These two effects are corroborated by the experimental observations obtained by Olof Peters (Figure 4.5 a) and Figure 5.9 in [155]), although the spin excitation

[1] Actually the dI/dV spectra should not be fitted by a single Fano function since they consist of a Kondo peak and spin excitation steps, and here it is just a rough estimation of the peak width.

steps are not visible in the dI/dV spectra taken at 7.2 K due to notable thermal broadening.

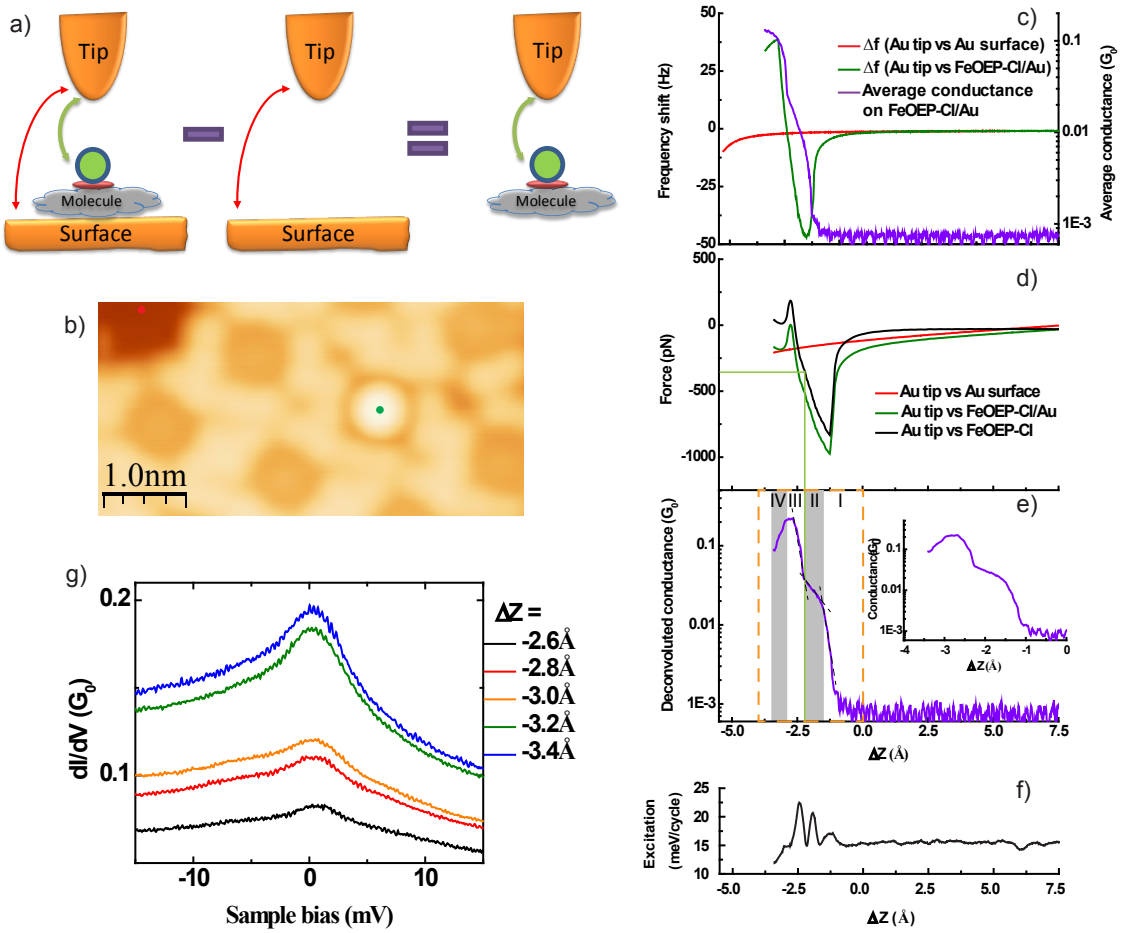

Figure 4.6: Force and conductance between a Au tip and a FeOEP-Cl molecule. **a)** Scheme for extracting the short range force between a Au tip and a FeOEP-Cl molecule. **b)** STM image showing the measuring sites for the Au tip on the Au surface and FeOEP-Cl, marked by red and green spots respectively (V = 50 mV, I = 50 pA). **c)** Frequency shift signal during the Au tip approaching on the Au surface and FeOEP molecule, and the simultaneously recorded average conductance curve for the FeOEP. The Δf curve taken for the Au tip on Au surface is shifted by -231 pm in the abscissa and plotted here. **d)** and **e)** are deconvoluted force and conductance from **c)** (inset in **e** is a zoom of the orange dotted area in the main panel). **f)** Excitation signal of the cantilever during the Au tip approaching on the FeOEP-Cl molecule. **g)** dI/dV spectra of the FeOEP-Cl molecule taken with lock-in modulation of 1 mV at 7.2 K (setpoint defined by V = 50 mV, I = 50 pA). Tip oscillation amplitude of 70 pm is used for acquiring the data shown here.

4.4.2 Force and Conductance between a Cl Functionalized Tip and FeOEP Molecules

Manipulation of the spin state can be also carried out for FeOEP molecules on the Au surface. In this case, a Cl atom terminated metal tip is utilized to exert force on FeOEP molecules and change their ligand field. As shown in Figure 4.7 a), the shapes of the dI/dV spectra measured in tunneling and contact regime at 1.2 K are drastically different (Figure is adapted from Olof Peters' master thesis [155]). The asymmetric dip feature originating from S = 1 for FeOEP changes into a symmetric line-shape, characterized by a Kondo peak and two steps aligned symmetrically to E_F, which is similar to the dI/dV spectrum of FeOEP-Cl contacted by a Au tip (red curve in Figure 4.5 a). This is a signature of increasing the total spin of Fe atom from S = 1 to S = 5/2, and also the oxidation state from +2 to +3. Since the configuration of the Cl terminated tip - FeOEP junction resembles that of the Au tip - FeOEP-Cl junction, it is expected that the Cl functionalized tip changes the square planar ligand field of Fe atom into a drastically different one analogous to FeOEP-Cl contacted by a Au tip (Figure 4.5 b). As shown in Figure 4.7 b), d orbital splitting of the Fe atom decreases with proximity of the Cl terminated tip. That is, the energy levels of d_{xy} and $d_{x^2-y^2}$ decrease while the energy of d_{z^2} increases. In order to understand how the terminated Cl ligand interacts with the FeOEPs, we quantify the force and conductance between them during tip approach.

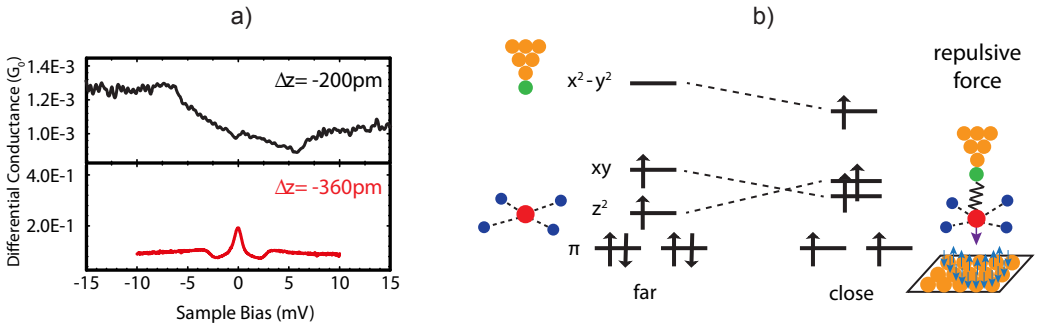

Figure 4.7: Distinguished dI/dV spectra for the FeOEP molecules taken by a Cl-terminated tip in tunneling and contact regime, and their corresponding ligand field splitting. **a)** Top panel: asymmetric dip feature when the tip approaches by 200 pm toward the molecule from the tunneling setpoint; bottom panel: a Kondo peak sandwiched by two symmetric steps when further decreasing the tip-sample distance by 160 pm. Setpoint is defined by V = 50 mV, I = 200 pA and dI/dV spectra are taken at 1.2 K and with lock-in modulation of 50 μV. Figures are adapted from Olof Peters' master thesis [155]. **b)** Change of the ligand field splitting for FeOEP molecules by contacting with a chlorinated tip and Kondo screening of the Fe atom by the substrate electrons.

Figure 4.8 a) demonstrates the procedure to extract the short-range force between a single Cl apex atom and a FeOEP molecule. There are four kinds of interactions between different objects if one considers the detailed configuration of the present molecule junction. These four forces exist between Au tip and Au surface (labeled

as $f1$), Au tip and FeOEP molecule (labeled as $f2$), terminated Cl atom and Au surface (labeled as $f3$), terminated Cl atom and FeOEP molecule (labeled as $f4$), respectively. In order to obtain $f4$, it is necessary to measure the forces induced by a Au tip and the same Au tip holding a Cl apex atom on the Au surface and on FeOEP/Au, and then subtracting the sum of the two forces for the Au tip on FeOEP/Au and the Cl functionalized tip on Au surface from the sum of the two forces for the Au tip on Au surface and the Cl functionalized tip on FeOEP/Au.

Figure 4.8 b) is the STM image recorded by a Au tip, in which the Au tip approaches on the Au surface and also one FeOEP molecule (marked by a red and black spot) by 3 Å. After taking these two spectra, the Au tip approaches on the Cl atom marked by a green cross by 3 Å from the initial height defined by V = 50 mV, I = 50 pA, for picking up the Cl atom from the FeOEP-Cl. It is visible that there is a abrupt spike in the frequency shift curve during the Au tip approaching on the Cl atom, indicating a change for the molecular junction (Figure 4.8 c). Then the same area as Figure 4.8 b) is scanned again and the corresponding image is presented in Figure 4.8 d). It exhibits enhanced resolution and absence of the manipulated Cl atom by the Au tip. According to these changes, we ascribe the new tip as a Au tip with a Cl apex. Similarly, the Cl terminated tip approaches toward the two identical sites as that in Figure 4.8 b) by 3.5 Å. For every measurement of these approaching motions, frequency shift and current signals are recorded simultaneously at a sample bias of 11 mV (Figure 4.8 e). The Δf curve of the Cl-terminated tip approaching on the FeOEP shows negative values with a minimum of -22.6 Hz at ΔZ = -1.9 Å, and then changes its sign into positive. In order to remove the effect induced by tip oscillation on the force and conductance, Δf and time-average conductance curves are processed following Sader-Jarvis formalism (equation 1.13) and Sader-Sugimoto method (equation 4.1), respectively. For force extraction, the tip heights of the Au tip on Au surface, Au tip on FeOEP/Au and Cl functionalized tip on Au surface are shifted by respective -225 pm, -76 pm and -145 pm with respect to that of the Cl functionalized tip on FeOEP/Au for compensating the initial tip height differences among them.

Figure 4.8 f) depicts the separate force curves of the Au tip and Cl functionalized tip approaching on the Au surface and FeOEP/Au, and also the short-range force ($f4$) between the single Cl atom and the FeOEP molecule. While the forces between the Au tip and Au surface, the Au tip and FeOEP/Au, the Cl functionalized tip and Au surface all have the attractive contributions, short-range repulsive interaction exists between the Cl apex atom and the probed FeOEP molecule when ΔZ is smaller than -2.86 Å.

The conductance curve can also be separated into four parts, as shown in Figure 4.8 g). In the tunneling range of -0.5 Å $>\Delta$Z$>$ -2.73 Å (gray shaded area), conductance increases from $6.5 \times 10^{-5} G_0$ to $\approx 0.05 G_0$ exponentially as a function of the tip displacement. For the transition regime of -2.73 Å $>\Delta$Z$>$ -3.06 Å, the conductance increases further and reaches $\approx 0.1 G_0$ with a slightly reduced slope. As further

minimizing the tip-molecule distance until ΔZ = -3.38 Å , the conductance shows a plateau feature and varies between $0.1G_0 - 0.12G_0$ in the contact regime. After that, it begins to decrease when possible instability comes up for the tip-molecule junction. At the tip-molecule contact point defined by the intersection of linear fits in the transition and contact regimes (indicated by the vertical green line in Figure 4.8 f and g), we obtain the tip-molecule force of 101 pN at ΔZ = -3.06 Å. Moreover, we can see the force becomes more positive with further minimized distance between the Cl tip and FeOEP molecule, originating from Pauli repulsion for electron cloud overlap. We note that the tip-molecule contact just slightly disturb the excitation signal of the cantilever which varies between 1.9 – 4.8 meV per oscillation cycle (Figure 4.8 h), which is two orders of magnitude lower than the bonding energy of $\approx$ 260 meV at the tip-molecule contact point of ΔZ = -3.06 Å (the bonding energy is obtained by integration of the short-range force over the approaching distance and not shown here).

A typical series of dI/dV spectra taken by a Cl functionalized tip on top of a FeOEP molecule at varied tip-sample distances shows that the transition of the line-shape from a asymmetric dip to a symmetric peak around E_F occurs in the range of -2.8 Å $> \Delta Z >$ -3.0 Å with respect to the initial tip height defined by V = 50 mV and I = 50 pA (Figure 4.8 i). In comparison with Olof Peter's measurement results depicted in Figure 4.7 a, this zero-bias peak can be attributed to Kondo resonance. Moreover, the tip-sample distance for dI/dV line-shape transition of FeOEP found in our simultaneous STM/AFM measurement with a periodically oscillating tip is comparable to that in the STM measurement observed by Olof Peters (transition also happened between -2.8 Å and -3.0 Å, Figure 5.14 in [155]), although the initial tip heights are slightly different (V = 50 mV, I = 50 pA in STM/AFM measurement and V = 50 mV, I = 200 pA in STM measurement at 1.2 K).

We note that the absolute value of $f4$ at the contact point varies for different Cl tips or FeOEP molecules, but the general tendency for $f4$ entering the repulsive regime is universal. In the contact regime, Fe atom is pushed down to the surface by the Cl tip (sketch at right side of Figure 4.7 b) and gives rise to dI/dV spectra consisting of two symmetric spin excitation steps and a Kondo peak, similar to that deriving from a FeOEP-Cl contacted by a Au tip. This indicates that the central Fe atom in the FeOEP molecule changes its oxidation state (total spin) from +2 (S = 1) to +3 (S = 5/2) with the Cl atom attaching on the tip all the time and no Cl ligand transfer to the underneath FeOEP. This process suggests a probable scenario that there is a charge transfer from the Fe atom to the surface (or one electron of Fe atom is trapped by the surface potential when the Fe atom is pushed toward the surface by the tip) and thus reducing the six valence electrons into five, giving rise to S = 5/2. Due to the Cl tip-derived proximity between the Fe atom and the Au surface, their electronic hybridization is strengthened and thus induces effective Kondo screening for the magnetic impurity atom.

In order to compare the influence of different tips on the magnetic property of FeOEP

molecules, Au tips and Xe atom terminated tips are also used in our measurements and the results will be presented in the following.

4.4.3 Modification of FeOEP-Surface Coupling by Au Tips

Figure 4.9 shows the evolution of dI/dV spectra for a FeOEP molecule measured by a Au tip with decreased tip-sample distances. At ΔZ = -3.2 Å, the dI/dV curve shows an asymmetric dip shape, which is the same feature as that in Figure 4.4 b). When reducing the tip-sample distance to ΔZ = -3.6 Å, a broad spectrum including two symmetric steps around E_{F} appears, and the step features become even more notable during the tip approach toward the molecule. The low energy of the steps together with the big change ($16\% - 32\%$) in differential conductance suggests inelastic spin excitation as origin of the steps [53]. This speculation is further supported by the proper fitting of the dI/dV spectra with the spin Hamiltonian for ligand field splitting $H_{eff} = DS_z^2 + E(S_x^2 - S_y^2)$ [2]. For instance, the fitting of the spectrum at ΔZ = -5.0 Å gives a D and E value of 4.9 meV and 0.7 meV respectively (violet dashed line in the middle panel of Figure 4.9 b). It is notable that E has the same energy as that of FeOEPs on a Pb(111) surface [150]. With further reduced tip-molecule distance, the symmetric step features change into a symmetric peak centered at E_{F}, which can be reproduced by a Fano function with a characteristic width $\Gamma_K \sim 10.8$ mV (gray dashed line in the top panel of Figure 4.9 b).

The modification for the magnetic properties of FeOEPs by contact with Au tips can be rationalized by considering the tip-molecule interactions and the movements of the Fe ion. In tip-molecule distance range of -3.6 Å $>$ ΔZ $>$ -6.3 Å, the Fe atom is lifted up by the Au tip thus quenching the effective Kondo screening of the Fe atom. While the tip-molecule distance reaches ΔZ = -6.6 Å, the Au tip pushes the Fe atom moving toward the substrate and a Kondo effect dominates over the magnetic anisotropy for FeOEPs with S = 1.

4.4.4 Modification of FeOEP-Surface Coupling by Xe Functionalized Tips

For the preparation of Xe functionalized tips, Xe gas is filled into the preparation chamber through a leak valve and the atoms adsorb onto the cold FeOEP-Cl/Au(111) sample placed in the STM chamber with open valve and shutter between the two chambers. After dosing the Xe atoms, small particles appear at the edge of molecular islands. A Au tip approaches on one of these particles by 3 Å (marked by the black dashed circle in Figure 4.10 a), and then retracts to the preset height (defined by V = 0.1 V, I = 33 pA). A hysteresis can be seen between the two frequency shift curves during the tip approach and retraction, indicating changes for the tip or

[2] For physical meaning of this formula please refer to 2.1.3.

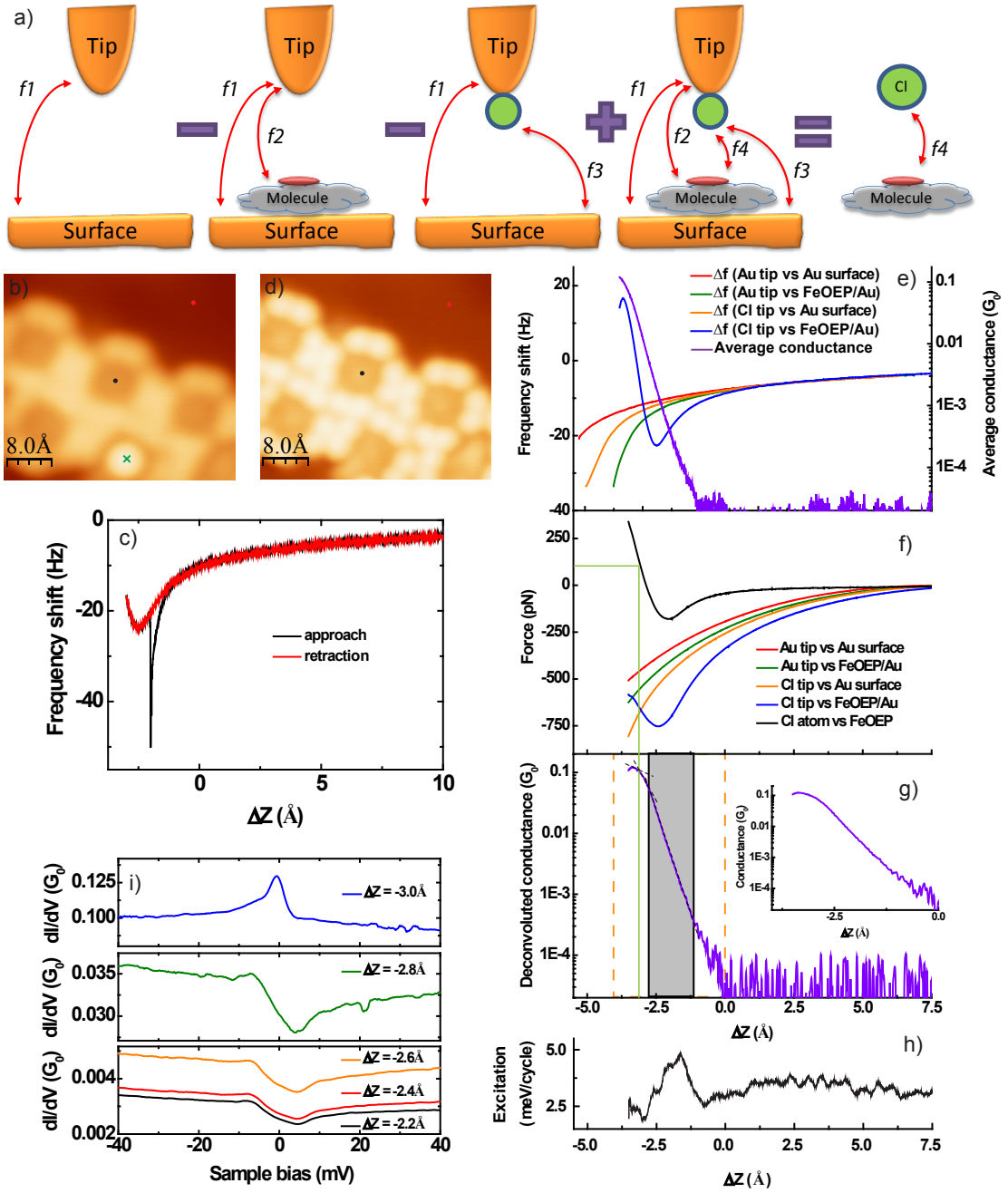

Figure 4.8: Force and conductance between a Cl-terminated tip and a FeOEP molecule. **a)** Schematic sketch of the procedure for getting the short-range force between a single Cl atom and a FeOEP molecules. **b)** STM topography of a molecular island recorded by a Au tip (V = 50 mV, I = 50 pA). **c)** Frequency shift signal during picking up the Cl atom by the Au tip. **d)** STM topography of the same molecular island as **b)** recorded by the Cl functionalized tip. **e)** Frequency shift signal recorded by a Au tip and a Cl-functionalized tip on the Au surface and on a FeOEP molecule, and the simultaneously acquired average conductance curve for the Cl-functionalized tip approach on the FeOEP. The Δf curves for the Au tip on Au surface, Au tip on FeOEP, Cl tip on Au surface are shifted by -225 pm, -76 pm and -145 pm in the abscissa respectively. **f)** Different forces between tip and sample. **g)** Deconvoluted conductance from the conductance curve in **e)**. Inset is a zoom of the orange dotted area in the main panel. **h)** Excitation signal of the cantilever during the Cl functionalized tip contacting the FeOEP molecule. **i)** Typical tip-sample distance dependent dI/dV spectra of the FeOEP molecules taken by a Cl-functionalized tip at 4.5 K with lock-in modulation of 1 mV (setpoint defined by V = 50 mV and I =50 pA). Tip oscillation amplitude of 30 pm is used for acquiring the data shown here.

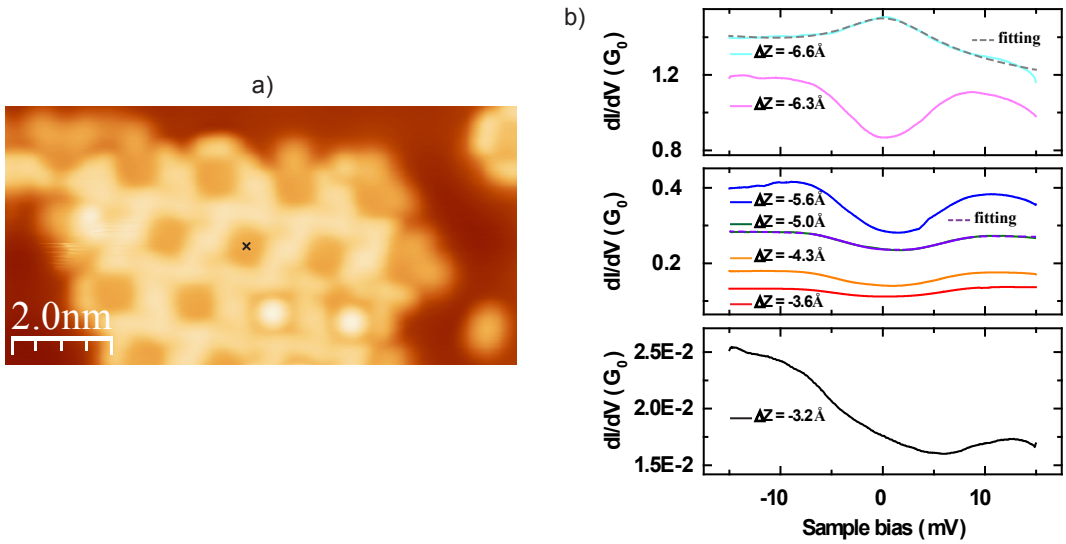

Figure 4.9: Evolution of the dI/dV spectra of a FeOEP molecule at varied Au tip-molecule distances. **a)** STM topography of a molecular island imaged by a Au tip (V = 50 mV, I = 50 pA). **b)** A series of dI/dV spectra of a FeOEP molecule (marked by a black cross in **a**) measured at gradually decreased tip-sample distances by a Au tip. dI/dV spectra are taken at 7.2 K and with a lock-in modulation of 1 mV.

the probed object (Figure 4.10 b). The posterior image of the same molecule island presents high resolution, and the addressed particle disappears (Figure 4.10 c). We propose this is a picking up event of a Xe atom by the Au tip. In contrast to the contracted size of Cl ligands imaged by a Cl-terminated tip, the Cl atoms expand in the Xe tip recorded images with the apparent size even bigger than that in Au tip scanned images, indicated by the line-profiles drawn from the two STM images (Figure 4.10 d).

Figure 4.11 a) is a molecular island imaged by a Xe-terminated tip, and the corresponding dI/dV spectra taken on a FeOEP molecule at varied tip-sample distances are depicted in Figure 4.11 b). When the tip is relatively far away from the molecule, dI/dV curves show an asymmetric dip feature, which are comparable to the dI/dV spectra measured by Au tips and Cl tips on FeOEPs (Figure 4.4 b and Figure 4.7 a). At the moment when tip moves 5.3 Å toward the molecule, the dI/dV spectrum shows symmetric steps centered at E_F. Since Xe atoms are chemically inert and unlikely to change the oxidation state of the Fe atom, the origin of the step features could be ascribed to spin excitation. Similar to the case of FeOEPs contacted by Au tips, we fit the steps in dI/dV spectra with the spin Hamiltonian for ligand field splitting. As an example, the fitting of the dI/dV curve at ΔZ = -5.6 Å with $D \sim$ 6.3 meV and $E \sim 0.7$ meV is plotted in Figure 4.11 b). This indicates an attractive force between the tip and molecule, which pulls the Fe atom away from the surface and reduces its hybridization with the surface.

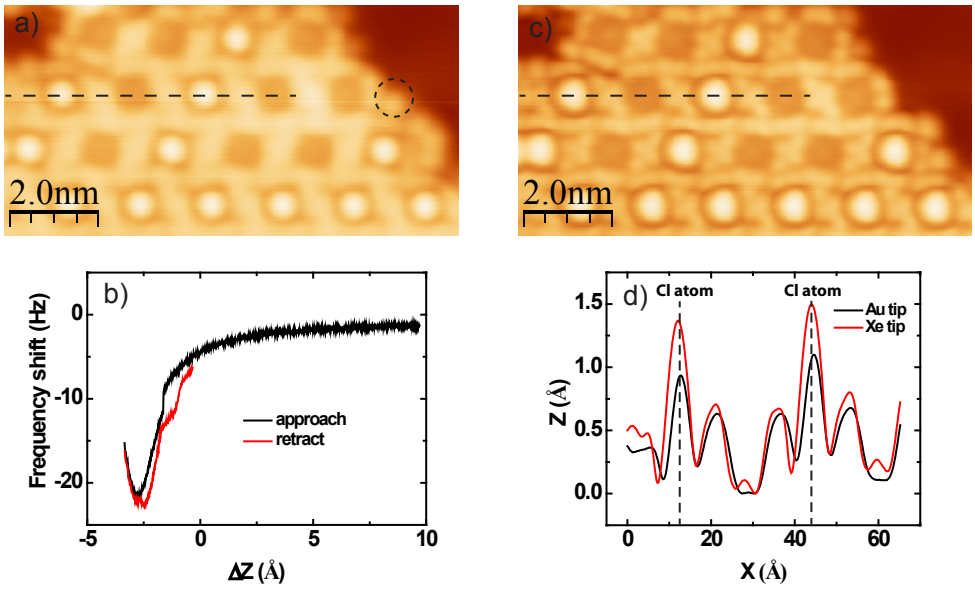

Figure 4.10: Picking up a Xe atom by a Au tip. **a)** STM image of a FeOEP-Cl island, small particles existing at the island rim after dosing Xe atoms. **b)** Frequency shift curve during approach and retraction of the Au tip on a particle at the molecular edge. **c)** High resolution STM image of the same molecule island after functionalizing the Au tip by a Xe atom. **d)** line-profiles on FeOEP and FeOEP-Cl molecules imaged by a Au tip and a Xe-functionalized tip (black dashed lines in **a** and **c**), the height of the FeOEP centers are set to zero. STM images in **a)** and **c)** are recorded with tunneling condition of V = 0.1 V and I = 33 pA.

In comparison with the dI/dV curves acquired by Cl functionalized tip (Figure 4.8 i), the Xe tip does not induce a Kondo peak. The different influences of Cl- and Xe-terminated tip on the magnetic states of FeOEPs can be rationalized by the high electron affinity of Cl atom and chemical inertness of Xe atom due to its full electron shell. The instantaneous conductance shown in Figure 4.11 c) is obtained using the Sader-Sugimoto deconvolution method (equation 4.1), and the kink on it could originate from the tip-molecule junction relaxation [151]. The short-range force between the Xe apex atom and the FeOEP molecule is not acquired due to lacking of the reference Δf curves for the Au tip approaching on the Au surface and FeOEP/Au before picking up the Xe atom.

4.5 Chemical Structure Determination of Iron Tetrabenzoporphyrin by NC-AFM

The temperature-induced stepwise transformation of iron octaethylporphyrin (FeOEP) into iron tetrabenzoporphyrin via a consecutive concentric electrocyclic ring closure, had been realized by B. W. Heinrich et al. [152]. The different intermediate reac-

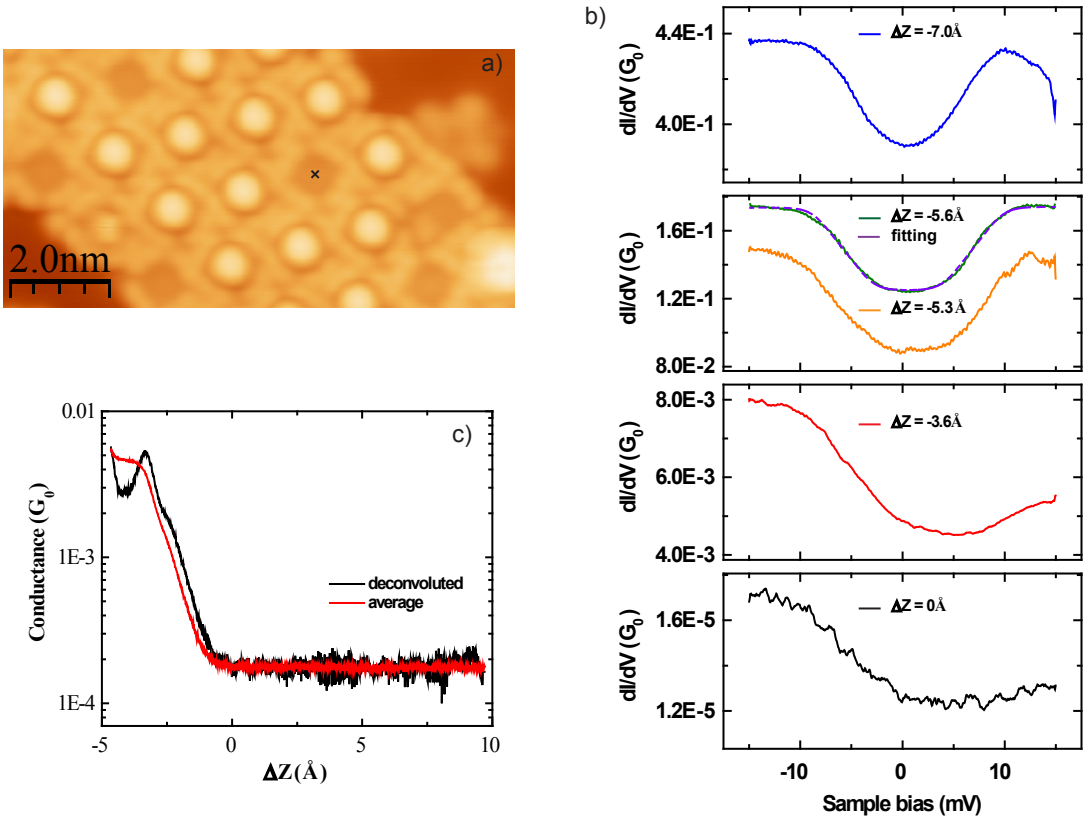

Figure 4.11: Influence of the Xe tip - FeOEP interaction on molecular magnetic properties. **a)** STM topography of a molecular island imaged by a Xe functionalized tip. **b)** A series of dI/dV spectra of a FeOEP molecule measured at gradually decreased tip-sample distances by a Xe tip. **c)** Conductance during the Xe tip approaching on the FeOEP. Setpoints for the STM image and spectra are defined by V = 50 mV, I = 50 pA. dI/dV spectra are taken at 7.2 K and with a lock-in modulation of 0.5 mV. Tip oscillation amplitude of 50 pm is used for acquiring the data shown here.

tion products are identified by scanning tunneling topography and spectroscopy and shown in Figure 4.12. As a complementary method, NC-AFM with a functionalized tip is a straightforward tool to determine molecular structures with atomic-level resolution. Here, we use Xe and Cl atom terminated tip for resolving structure of iron tetrabenzoporphyrin, which is the final product of the reaction series. Xe atoms and additional FeOEP-Cl molecules are deposited onto the ring closure reacted FeOEP/Au(111) sample for tip preparation.

The STM topography and constant-height frequency shift (Δf) images recorded by Xe and Cl atom decorated tip are shown in Figure 4.13. A high-resolution STM image of a single iron tetrabenzoporphyrin recorded by a Xe tip demonstrates a four-fold symmetric cross shape with a central circular depression (Figure 4.13 a).

When looking at the frequency shift images obtained by Xe (Figure 4.13 b, c) and

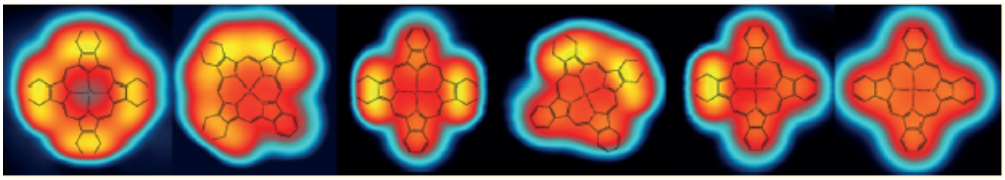

Figure 4.12: Temperature-induced stepwise transformation of iron octaethylporphyrin into iron tetrabenzoporphyrin via concentric electrocyclic ring closure reaction. Figure is adapted from [152].

Cl (Figure 4.13 d, e) tip at ΔZ = -0.5 Å with respect to the preset height (defined by V = 5.1 mV, I = 28 pA on Au surface), we find that both tips reveal detailed intramolecular information about the chemical structure [164]. It is notable that the molecule size in figure 4.13 b) is bigger than that in figure 4.13 d), and molecule also show distinguished corrugation features in these two images. Superposition of molecule model onto Δf images enables us to identify inner molecule species. From molecular center to peripheral legs, we can see the nitrogen atom, C-C double bond at the border of pyrrole and benzene ring, and the hexagonal contour of the partial benzene ring lying most outside, respectively (figure 4.13 c). In Cl tip recorded image, benzene rings and subsidiary C-H bonds are visible (figure 4.13 e). These observations confirm the proposed structure of iron tetrabenzoporphyrin produced by in-situ chemical reaction on metal surface. The iron atom at the center is not resolved, since it is lower than the macrocycle plane of the molecule. Additionally, dark contrast can be seen at the molecular rim in figure 4.13 d), indicating attractive tip-sample interaction.

4.6 Conclusion

Based on the known results that the magnetic properties of FeOEP-Cl and FeOEP molecules can be tuned by respective interaction with a Au tip and a Cl functionalized tip [155], we show the simultaneously obtained force and conductance in these two manipulation processes by combined STM/AFM measurements.

With stepwise approach of a Au tip on the FeOEP-Cl molecules, the concomitant short-range force and conductance indicate a transition from tunneling to point-contact regime during the tip motion toward the molecules. It is found that both the attractive and repulsive forces between the Au tip and FeOEP-Cl molecule can release the central Fe atom toward the Au surface. In the repulsive tip-molecule interaction regime, a new Kondo peak at E_{F} arises in the dI/dV spectra of the FeOEP-Cl molecule due to enhanced Fe-surface hybridization.

Likewise, the transition from tunneling regime to contact regime is also evidenced by the simultaneously recorded force and conductance for the Cl functionalized tips

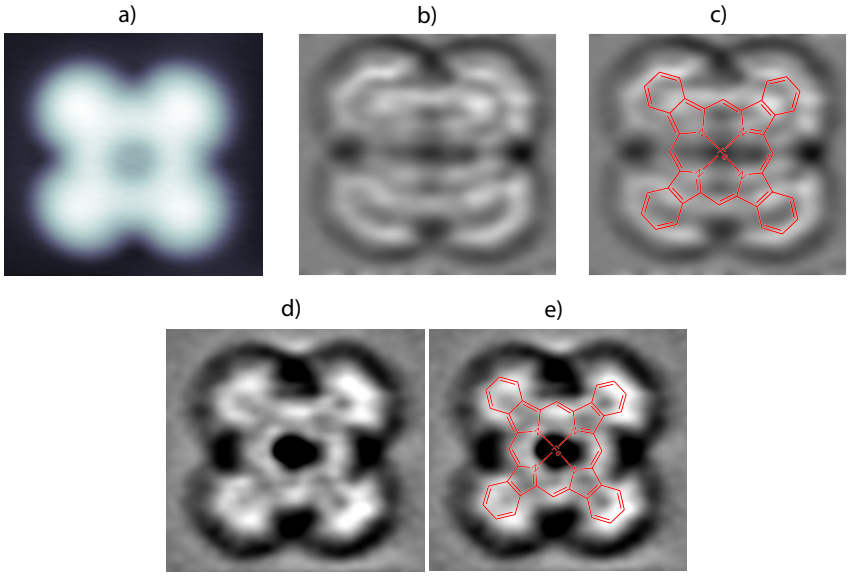

Figure 4.13: STM topography and constant height AFM images of iron tetrabenzoporphyrin. **a)** STM topography recorded by a Xe tip (V = 51 mV, I = 28 pA). **b)**, **c)** Δf image taken with a Xe tip without or with superposition of a molecular model on top (vertical distance ΔZ = -0.5 Å from the STM setpoint V = 51 mV, I = 28 pA above the substrate). **d)** and **e)** Δf image taken with a Cl tip without or with superposition of a molecular model on top (vertical distance ΔZ = -0.5 Å from the STM setpoint V = 0.5 V, I = 50 pA above the substrate. Δf images are Laplace and low-pass filtered.

moving close to the FeOEP molecules. Short-range repulsion force exists between the Cl apex atom and FeOEP molecules in contact regime, suggesting pushing down of Fe atom toward the surface. dI/dV curves characterized by a Kondo resonance at E_{F} are observed for FeOEP molecules contacted by an Cl-terminated tip, indicating change of the spin state (oxidation state) from S = 1 (+2) to S = 5/2 (+3) for the Fe atom, while the Cl atom remains attached to the tip. For FeOEPs in contact with Au tips, the molecular dI/dV spectra evolve from an asymmetric dip into spin excitation related steps and then to a Kondo peak, induced by the attractive and repulsive tip-molecule interaction respectively. Moreover, dI/dV spectra of FeOEPs show symmetric step features but not Kondo peak under the stimulation of Xe functionalized tips, suggesting chemical identification of apex atoms on STM tip for manipulating magnetic states of FeOEPs.

The conformation of iron tetrabenzoporphyrin originated from the temperature-induced ring closure reaction of FeOEPs is confirmed by the constant-height Δf images recorded with a Xe and Cl functionalized tip, respectively.

5 Reversible Change of the Spin State in a Mn-TPTBP on Au(111) by Coordination of a CO Molecule

5.1 Introduction

Controlling spin states of magnetic molecules and their interaction with a substrate at the single molecule level is essential for the emerging field of molecular spintronics. Coordinatively unsaturated metal ions in metal-porphyrins and metal-phthalocyanines present a local reactive site, which offers a unique opportunity of controlling the magnetic moment by external chemical stimuli. The axial coordination of small gaseous molecules like CO, NO or O_2 to these complexes substantially alters their electronic and magnetic properties [165], [34], [166], [167], [168], [169]. The real scenario of the coordination reaction is more complex, since the chemical bond to the reactant molecule causes the redistribution of charge in the d orbitals of the metal center and modifies the ligand field of the metal ion, determining the magnetic ground state of the organometallic complexes. In the case of an adsorbed metal complex on a metal surface, the formation of a new ligand bond may additionally alter the hybridization of molecular and substrate states, thus affecting the electronic and magnetic coupling of the metal ion to the substrate [169], [170].

When metal-porphyrins and metal-phthalocyanines are attached to nonmagnetic metal substrates, the exchange coupling between the molecular unpaired spins and substrate conduction electrons may give rise to a Kondo state [171], [172], [173], [157], [174]. Base on the observed Kondo effect, it is possible for us to get a hint for the spin state of the magnetic molecules, which can be further verified by spin-polarized density-function theory calculation.

In this chapter, we study the electronic structure and magnetic properties of manganese tetra-phenyl-tert-butyl-porphyrin (Mn-TPTBP) molecules adsorbed on a Au(111) surface. Moreover, a reversible control of the spin state of Mn-TPTBP on Au(111) by binding and desorption of a CO molecule will be demonstrated.

5.2 Properties of Mn-TPTBP Molecules in Gas Phase

Figure 5.1 a) show the chemical structure of a free Mn-TPTBP molecule, which is optimized by density functional theory (DFT) calculation (the method is described in section 5.4.2). The molecular macrocycle consists of a central Mn ion coordinately bond to four neighboring nitrogen atoms in the surrounding pyrrole rings, and the peripheral meso-substitutes are four phenyl rings with tert-butyl groups.

For free manganese porphyrins, their Mn(II) center has five d-orbital electrons which possess a high spin state of S = 5/2 in a square planar ligand field [175], [176]. Due to different interactions between the Mn sublevel d orbitals and the surrounding organic ligands, the d orbital degeneracy is lifted up as shown in Figure 5.1 b). The $d_{x^2-y^2}$ and d_{xy} orbitals are highest and lowest in energy respectively, and the d_{xz}/d_{yz} orbitals are degenerate [175]. Mn(II) porphyrins have a positive axial anisotropy D [177], which gives rise to a zero-field splitting of their spin states with the highest energy spin of $S_z = \pm 5/2$ (Figure 5.1 c).

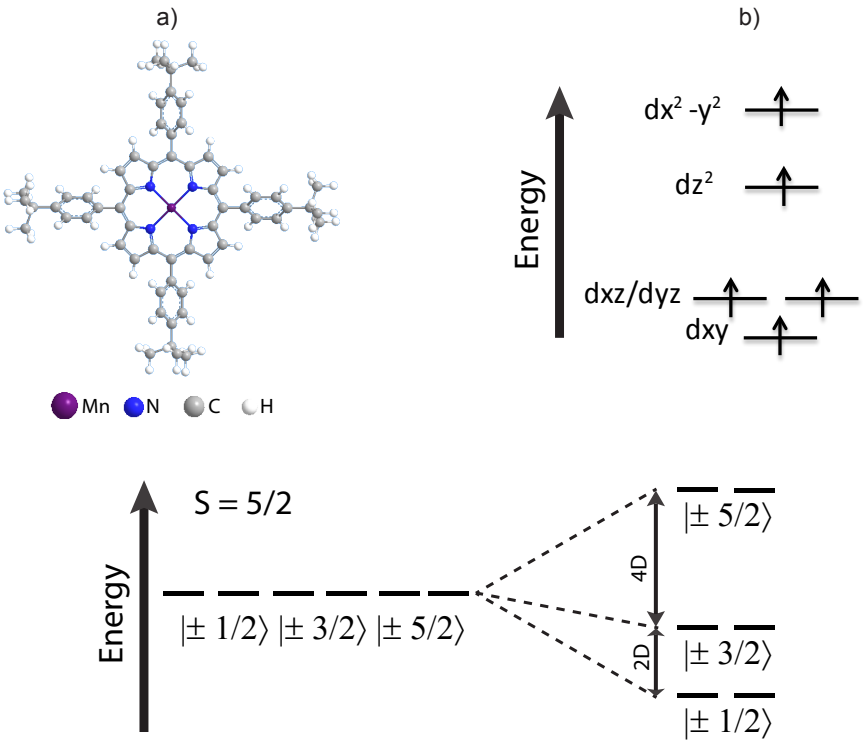

Figure 5.1: a) Chemical model of a free Mn-TPTBP optimized by DFT calculation. The Mn, N, C and H atom are colored into purple, blue, gray and white, respectively. **b)** Ligand-field splitting of the d orbital of Mn porphyrins. **c)** Zero-field splitting for the high spin state S = 5/2 of the Mn porphyrins.

5.3 Self-Assembly of Mn-TPTBP Molecules on Au(111)

Mn-TPTBP molecules self-assemble into uniform islands on Au(111) surface held at room temperature, indicating a dominant intermolecular coupling over molecule-substrate interaction (Figure 5.2 a). Four tert-butyl arms in four neighboring molecules aggregate and form a cross shape, allowing the dense packing of molecules in islands. The two dimensional molecular island shows a periodicity, characterized by the unit cell (black rectangle) with the two side lengths of $a = 15 \pm 1$ Å and $b = 18 \pm 1$ Å. The unequal side lengths are probably due to a saddle shape adopted by the molecules on the surface. High-resolution STM images show that each molecule has a visible Mn center with four notable protrusions corresponding to the terminal tert-butyl groups (see superimposed molecular model in 5.2 b).

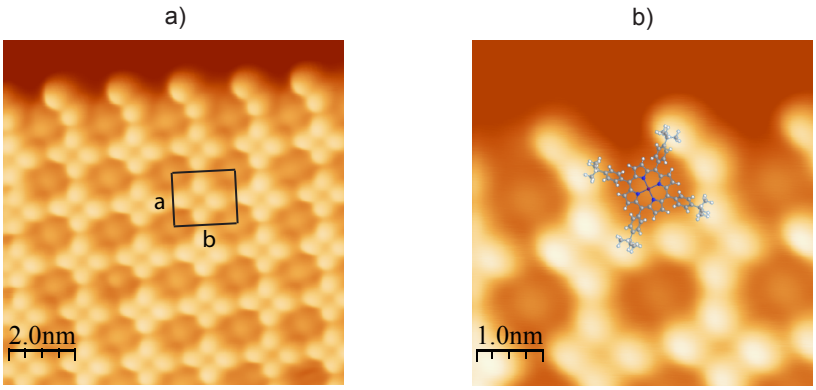

Figure 5.2: STM topography of Mn-TPTBP molecules on Au(111). **a)** An overview image of Mn-TPTBP island (V = 50 mV, I = 31 pA). **b)** High-resolution image of Mn-TPTBP island with a superimposed molecular model (V = 50 mV, I = 31 pA).

5.4 Electronic Properties of Mn-TPTBP Molecules on Au(111)

5.4.1 Molecular Orbitals and Their Spatial Distribution

For metal surface anchored molecules, their electronic structures can be altered by the molecule-surface interaction and thus affecting the transport properties. Electronic states of Mn-TPTBP molecules are manifested by STS in Figure 5.3. The dI/dV spectrum shown in Figure 5.3 b) is taken on a central Mn ion with open feedback loop, and three shoulders appear at positive biases but no feature at negative bias. In order to gain better resolution for these molecular orbitals, we also record the dI/dV signal when ramping the sample bias from 0.2 V to 3.0 V with feedback on. As depicted in Figure 5.3 c), two discrete resonance peaks are resolved at V =

1.1 V and 1.7 V, with a shoulder centered at 1.3 V. Moreover, we can also see an extra resonance close to V = 2.5 V.

Spatial distribution of molecular orbitals at V = 1.1 V and 1.7 V are illustrated in Figure 5.4. dI /dV maps are taken simultaneously with the STM topographies at constant height mode. A comparison of the STM topographies recorded at 1.1 V and 1.7 V demonstrates a strongly bias dependent appearance of intramolecular features (Figure 5.4 a, b). dI/dV map at 1.1 V shows bright lobes mainly localized over the four meso bridge carbon atoms and connected phenyl rings, and a local central depression. However, a clover shape for the central molecule part with a pronounced protrusion on the Mn ion are visible in the dI/dV map at 1.7 V. One can also see the influence of molecular topography in the dI/dV maps, reflected by the four bright spots surrounding the central porphyrin, which correspond to the bulky tert-butyl legs.

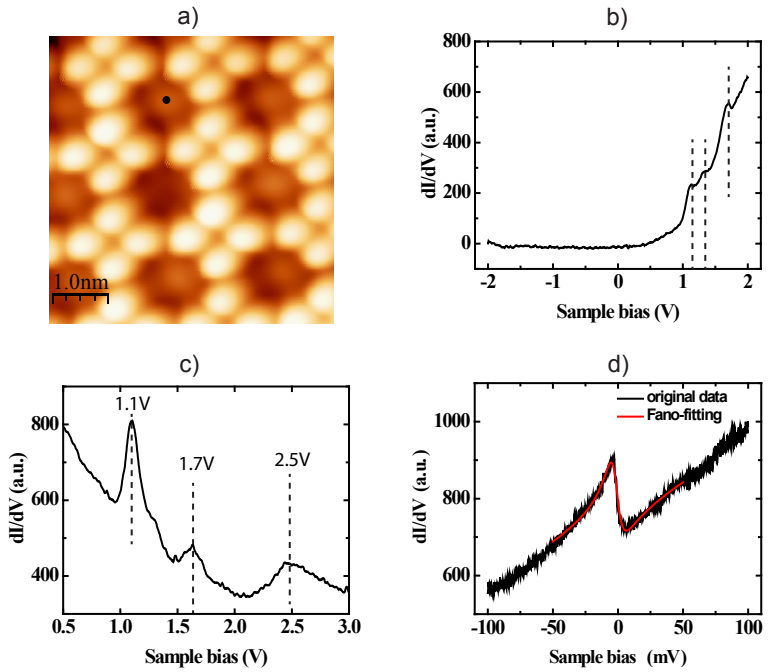

Figure 5.3: dI/dV spectra of Mn-TPTBP on Au(111). **a)** STM image with the location for taking the dI/dV spectra indicated by a black dot. **b)** dI/dV spectra on Mn ion with feedback off (setpoint defined by V = 2 V, I = 0.5 nA). **c)** dI/dV spectra on the same Mn ion with feedback on (setpoint defined by V = 0.2 V, I = 0.2 nA). **d)** Asymmetric peak feature at E_F in dI/dV spectra and its fitting by a Fano function with a linear background (setpoint defined by V = 0.1 V, I = 1 nA, lock-in modulation of 0.97 mV).

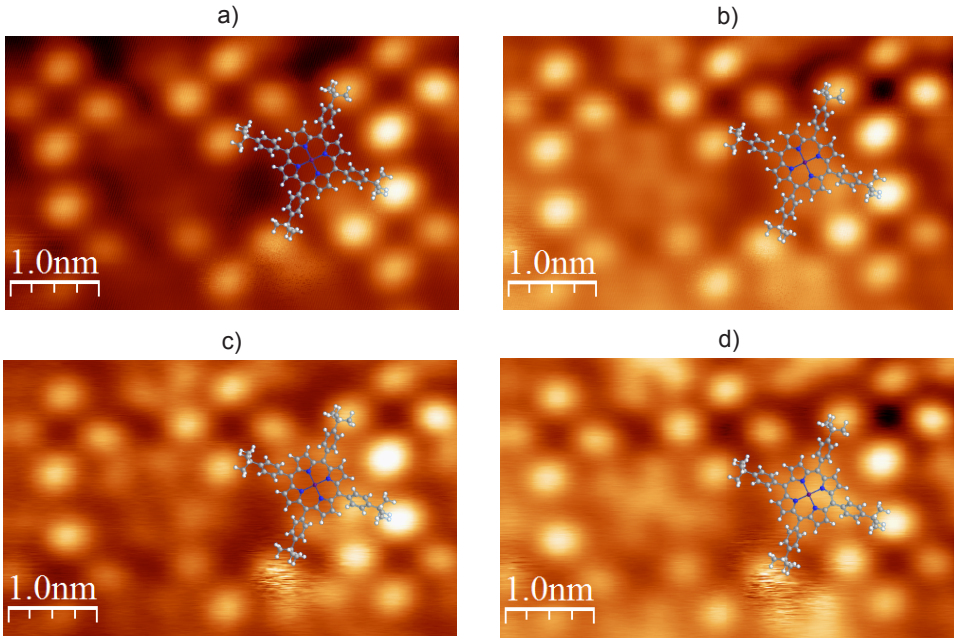

Figure 5.4: STM topographies and dI/dV maps of Mn-TPTBP at constant height mode. **a)** and **b)** STM topographies at V = 1.1 V and 1.7 V, respectively. **c)** and **d)** are pertinent dI/dV maps of **a)** and **b)**.

5.4.2 Density Functional Theory Calculated Molecular Orbital of Mn-TPTBP

The spectroscopic signature and selective mapping of the Mn-TPTBP frontier orbitals suggest that the molecular electron system is largely decoupled from that of the Au substrate [178], [86]. In order to understand the observed orbital features, we use first-principle calculation based on density functional theory to simulate Mn-TPTBP in gas phase and treat the electronic density of state as an approximation to the experimentally detected electronic structures. DFT calculation is carried out by Dr. Shulai Lei from the chemistry department of Freie Universität Berlin.

Spin-polarized DFT calculations are performed using the Vienna ab-initio simulation package (VASP) [179], [180] with the projector augmented waves method [181] and associated pseudopotentials [182]. The kinetic energy cutoff for wave functions is set to 400 eV. Electron-electron exchange and correlation interactions are described within the generalized gradient approximation (GGA) by employing the Perdew-Burke-Ernzerhof (PBE) functional [183]. The strong correlation effects in the d-electron states of the Mn atom are treated by the GGA+U method with U = 4.0 and J = 1.0 eV. These values were shown to provide the correct spin state for manganese porphyrins in gas phase or on surfaces [149], [184]. An energy convergence criterion of 10^{-4} eV for each atomic configuration is enforced. Atomic positions are fully relaxed using a conjugate gradient scheme until atomic residual forces are less than 0.01 eV/Å. The calculation of an isolated Mn-TPTBP molecule is performed using

$30 \times 30 \times 15$ Å^3 simulation cells.

Figure 5.5 a) is the DFT optimized geometry of Mn-TPTBP molecule. The molecule adopts a saddle shape with an upright pyrrole pair (α-pyr) tilted by 17° and a downward pyrrole pair (κ-pyr) tilted by 7°, leading to a twofold macrocycle symmetry. The rotation angle θ of the outside phenyl-tert-butyl legs is about 60° with respect to the the molecular macrocycle plane, induced by the steric repulsion between the hydrogen atoms from the pyrrole rings and the phenyl-based substituents [185]. The central Mn ion is about 0.15 Å above the plane formed by the four pyrrolic nitrogen atoms.

For molecular electronic structure, four DOS peaks can be seen in the energy range from Fermi energy to +3 V, which are centered at 0.25 V, 1.4 V, 2.0 V and 2.5 V, respectively (Figure 5.5 b). Moreover, an occupied orbital at -0.25 V is visible. E_{F} is set to the center of the gap between the highest occupied molecular orbital (HOMO) and lowest unoccupied molecular orbital (LUMO), and the DOS peaks are calculated with a broadening of 0.1 eV. Upon adsorption onto metal surfaces, the molecular HOMO-LUMO gap can be reduced due to surface polarization effects when compared to free molecule, causing unoccupied levels shifting toward lower energies [186], [86]. When relating the calculation results to our experiment resolved molecule orbitals, the DOS peak at 0.25 V from simulation is not discovered in dI/dV spectra, which is probably quenched by the substrate. However, the electronic density distributions of calculated molecular orbitals at V = 1.4 V and 2.0 V (Figure 5.5 c and d) are highly resembling to the dI/dV maps obtained with sample biases of 1.1 V and 1.7 V (Figure 5.4 c and d), respectively. Therefore, the resonances at 1.1 V and 1.7 V in dI/dV spectrum of Mn-TPTBP can be assigned to the LUMO+1 and LUMO+2 orbitals.

5.5 Magnetic Properties of Mn-TPTBP Molecules on Au(111)

Metalloporphyrins can bear various possible spin configurations depending on their ligand field. Previous studies showed that manganese(II) tetraphenylporphine (Mn-TPP) in the crystal (toluene solvate) has high spin state (S = 5/2) with the Mn(II) atom out of the porphyrin plane [187], [188]. Additionally, calculations using DFT+U method obtained energetically preferred S = 5/2 spin state for free Mn porphine molecules, whereas it changed into S = 2 by adsorption onto Au(111) [176]. Mn porphine can be physisorbed or chemisorbed on cobalt surface, possessing S = 2 and S between 2 and 5/2, respectively [149]. Liao et al. presented that the electronic properties of metal porphyrins are insensitive to the nature of their peripheral substitutes in gas phase [189]. These researches act as a prerequisite of our study here, and it is reasonable to speculate the spin S = 5/2 or S = 2 for Mn-TPTBP molecules adsorbed on Au(111) surface.

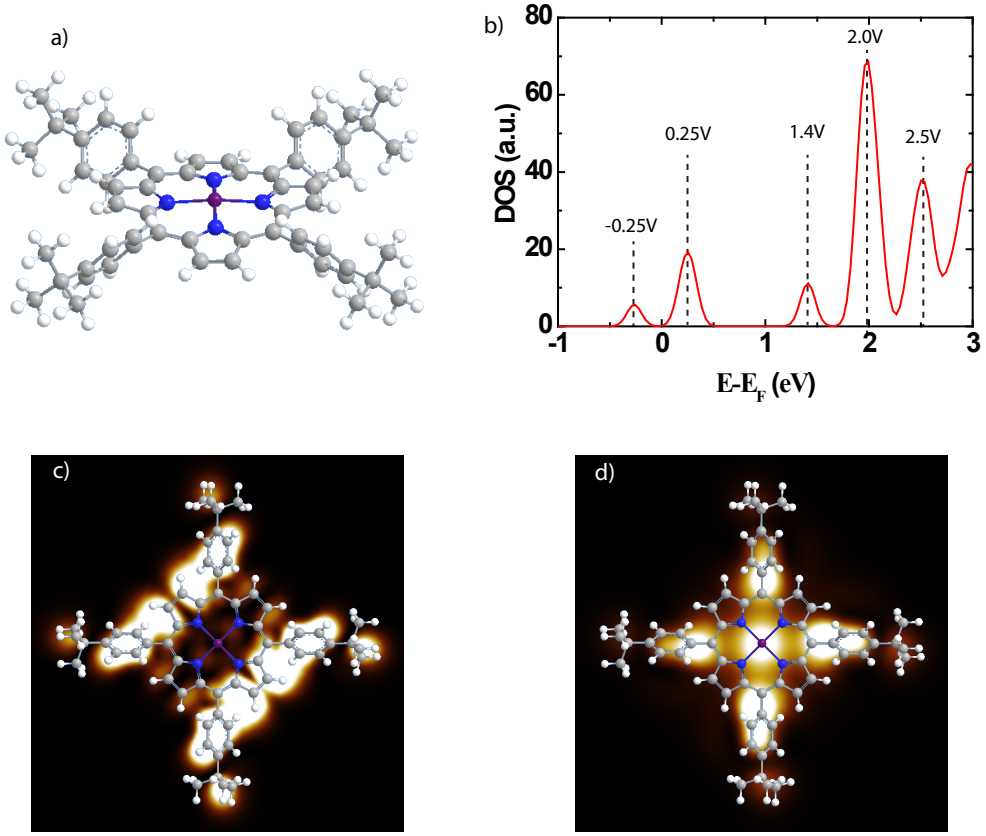

Figure 5.5: DFT calculated geometry and orbitals of Mn-TPTBP molecule. **a)** Optimized geometry (side view). **b)** DOS curve of Mn-TPTBP calculated with a broadening of 0.1 eV. **c)** and **d)** are electron density distributions of the plane lying 5 Å above the molecular plane at V = 1.4 V and 2.0 V, respectively. The corresponding molecular model is superposed on them.

5.5.1 Zero-Bias Peak of Mn-TPTBP

dI/dV spectroscopy of Mn ion acquired at a small sample bias range demonstrates an asymmetric peak feature close to E_F (Figure 5.3 d). The zero-bias anomaly had been discovered for magnetic atoms and molecules adsorbed on surfaces, which were identified as Kondo resonance in most cases [108], [107], [190], [157], [173]. Therefore, the intuitive impression allows us to assign this zero-bias peak (ZBP) to a fingerprint of Kondo effect for Mn-TPTBP, and it can also be properly fitted by a Fano-function with a linear background as:

$$\frac{dI}{dV} = A_K \cdot \frac{(q \cdot \Gamma_K/2 + eV - E_K)^2}{(\Gamma_K/2)^2 + (eV - E_K)^2} + s \cdot V + c \tag{5.1}$$

A_K is the amplitude of the Kondo resonance, q the asymmetry factor, Γ_K the intrinsic full width at half maximum (FWHM), e the elementary charge, V the sample bias, E_K the energy position of the resonance center, s the slope of the background, and c is a constant. In order to verify the assignment of this ZBP, we explore its character at various temperatures.

5.5.2 Temperature-Dependent Evolution of Zero-Bias Peak

We use two methods to control the sample temperature for our measurement. Firstly, we warm up the sample by shining light inside the STM shield with a lamp working at maximum power of 20 Watt. After 12 hours, the temperature increases from lowest 4.5 K to 6.5 K and stabilizes there. For higher temperatures, we lift up the shutter of the helium and nitrogen shields to different positions and fix it, then wait at least 8 hours for each stable T value. Data are acquired until the temperature fluctuation is smaller than 0.5 K in 30 minutes.

dI/dV spectra taken at 4.5 K, 6.5 K, 24 K and 46 K are shown in Figure 5.6 a), and we can see a notable thermal-broadening for the ZBP. We note that, while the observed spectral line shapes reveal intrinsic molecular character, the relative amplitude between spectra does not reflect an intrinsic molecular property due to the use of different tips at varied temperatures and different STM setpoints for recording dI/dV spectra on molecules. All the dI/dV spectra have been fitted by the Fano-function with a linear background (equation 5.1), indicated by the dashed blue lines on top of measured spectra. The intrinsic full-width at half maximum (Γ_K) of the spectra excluding the thermal broadening and lock-in modulation effect is extracted from the fitting results through the relation $\Gamma_K^{exp}(T) = 0.78\Gamma_K(T) + 3.52K_BT + V_{rms}$ (equation 2.16). In Figure 5.6 b), one can see the fitting of the FWHM as a function of T following a Fermi-liquid approach as $\Gamma_K(T) = 2\sqrt{(\pi k_B T)^2 + 2(k_B T_K)^2}$ (equation 2.15) [110], [191], [192] giving the Kondo temperature of 62.8 ± 6.1 K. Comparing with other paramagnetic metalloporphyrin molecules on metal surfaces [120], [171], [193], [178], the Kondo temperature of this system is reasonable. The average values of the fitting parameters Γ_K, q and s over four molecules are shown in Figure 5.6 c). The deviations between molecules for the q and s are probably due to different adsorption sites for molecules in islands on the Au surface considering its herringbone patterns.

For a S $> 1/2$ half-integer spin system, the Kondo effect could coexist with zero-field splitting (ZFS) when the sublevels of $S_z = \pm 1/2$ are the ground state. In the integer spin systems with ZFS, the Kondo effect is unlikely to occur because the spin degeneracy in the ground state needed for Kondo screening is removed, although a few examples of underscreened Kondo state for S $= 1$ molecular systems had been demonstrated [194], [165], [195]. According to this, we propose that the high spin state S $= 5/2$ is preserved for Mn-TPTBP molecules upon adsorption on Au(111) surface, with the degenerate $S_z = \pm 1/2$ states serving as the ground state in an easy-plane anisotropic environment (anisotropy constant $D > 0$) [177]. The preservation of high spin configuration S $= 5/2$ of Mn-TPTBP adsorbed on Au(111) surface probably originate from the fact that the bulky butyl groups can act as stereoscopic spacers which decouple the aromatic π system of the macrocycle with the central Mn ion to the Au surface.

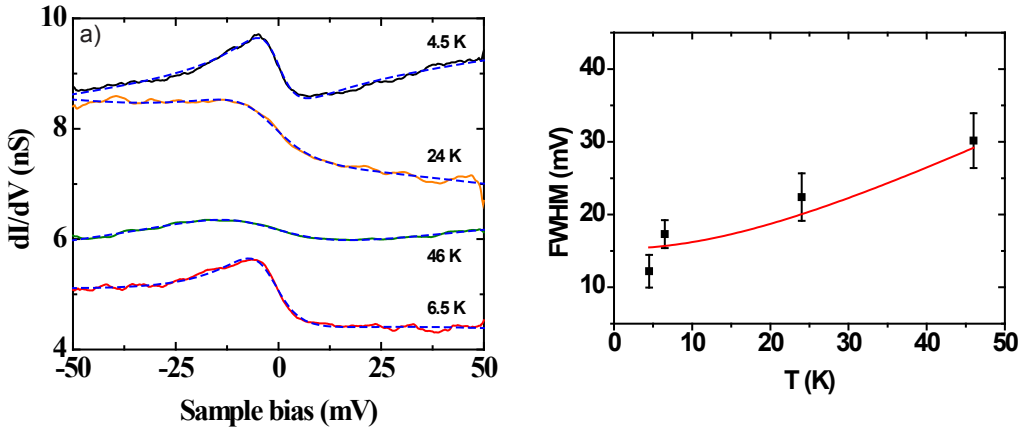

c)

parameters / temperature	Γ_K (mV)	q	s (nS/V)
4.5 K	12.2 ± 1.7	-1.4 ± 0.1	8.9 ± 6.8
6.5 K	17.3 ± 1.3	-1.7 ± 0.3	-4.2 ± 3.4
24 K	22.4 ± 2.6	-1.8 ± 0.5	-11.1 ± 5.6
46 K	30.2 ± 3.3	-2.2 ± 1.1	8.3 ± 5.1

Figure 5.6: Temperature-dependent evolution of the zero-bias peak. **a)** ZBP at various temperatures and their fitting (dashed blue lines) by a Fano function with a linear background as described by equation 5.1. dI/dV spectra are recorded with lock-in modulation of 0.91 mV at different tip-sample distances defined by sample bias and tunneling current of 0.1 V and 1.0 nA at 4.5 K, 0.1 V and 0.5 nA at 6.5 K, 0.1 V and 1.0 nA at 24 K, 0.1 V and 0.8 nA at 46 K. The original data is smoothed and plotted here. The dI/dV spectra taken at 24 K and 46 K are offset by -0.1 nS and -0.2 nS for clarity. **b)** Intrinsic full-width at half maximum (Γ_K) of the ZBP as a function of the temperature. **c)** Fitting parameters of the ZBP at different temperatures. The background slope (s) is counted with the unit of nano-Siemens per volt (nS/V). All the fitting parameter values are averaged over four molecules at each temperature, and the standard errors are calculated with the formula $\bar{\sigma} = \sqrt{\frac{1}{n-1}\sum_{n=1}^{n}(x_i - \bar{x})^2}$ with n the number of measurements and $\bar{x}$ the mean value of the measured parameters.

5.5.3 Spatial Distribution of Kondo Resonance inside Molecules

In case of metalloporphyrins in contact to a metal surface, molecule-substrate hybridization may realign the molecular orbitals and cause charge redistribution inside molecules. In this way, spin polarized DOS may not only locate at the central metal ion but also on organic ligands [145]. The Kondo resonance, as a mark of unpaired spins screened by conduction electrons, can monitor the interfacial charge transfer between molecule and substrate [190]. Here we took dI/dV spectra along a molecular main axis to explore the spatial variation of the Kondo effect. Figure 5.7 shows

the evolution of the Kondo resonance from one pyrrole ring to its opposite counterpart crossing the central Mn ion. An intensive Kondo peak is found on the magnetic atom, but it weakens or even vanishes toward the pyrrole rings. This result implies a localized d orbital of the Mn ion for Kondo screening and no obvious scattered spin state for peripheral ligands.

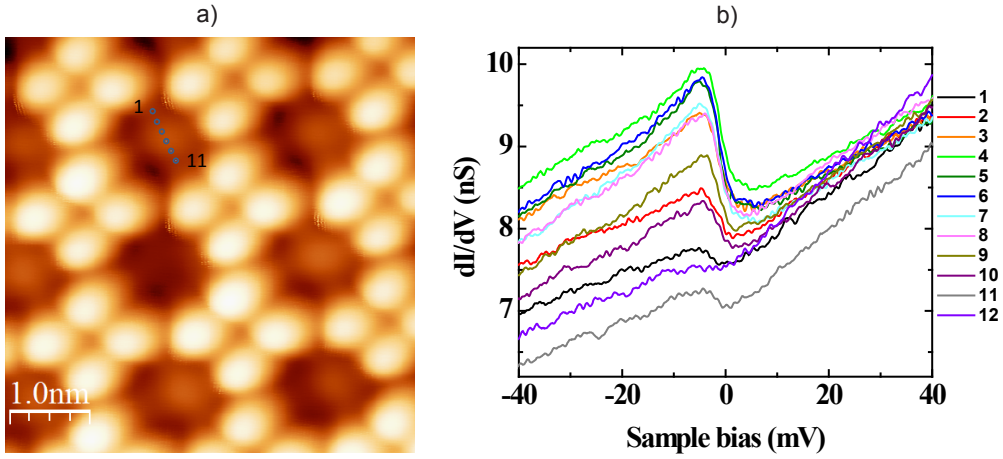

Figure 5.7: dI/dV line-spectra of Mn-TPTBP molecules. **a)** STM image in which dI/dV spectra are taken along a molecular main axis indicated by the dotted blue line. Distance between spectra is 0.62 Å. **b)** Evolution of Kondo resonance along the line (setpoint defined by V = 0.1 V, I = 1.0 nA, lock-in modulation of 0.97 mV).

5.6 Reversible Change of Spin State for Mn-TPTBP by CO Coordination

5.6.1 Bidirectional Controlling the Spin State of Mn-TPTBP by CO Attachment and Detachment

For metalloporphyrins and metallophthalocyanines on metal surfaces, coordination of small gaseous molecules to them is a reliable way for *in situ* controlling their magnetic states. We use CO molecules as an extra ligand to control the spin configuration of Mn-TPTBP molecules. The Mn-TPTBP covered sample is kept at 143 K and exposed to CO gas at partial pressure of 5.1×10^{-10} mbar for 35 s (background pressure is 2.5×10^{-10} mbar). After CO exposure the structure of the molecular island is unchanged, but some molecules ($\approx 20\%$) now exhibit a bright species on top of them (Figure 5.8 a). We identify these new molecules as CO-ligated Mn-TPTBP. Figure 5.8 b) shows a high resolution STM image of the new species embedded in the Mn-TPTBP island. The CO-coordinated molecules exhibit similar geometry as Mn-TPTBP, with a central protrusion appearing 1.2 Å higher than Mn-TPTBP (V = 1.1 V, I = 30 pA), indicating that a single CO molecule bonds directly to the transition metal ion.

Figure 5.8 c) depicts the dI/dV spectra taken on Mn-TPTBP molecules coordinated or uncoordinated by a CO ligand. There is a drastic contrast for the electronic properties of these two molecule species close to E_F, as the asymmetric Kondo peak of intact Mn-TPTBP changing into a novel line shape formed by a dip on top of a peak after CO adsorption on Mn ion (Figure 5.8 d). The notable change for the zero-bias resonance indicates that the coordination to CO modifies the magnetic state of the molecule. This modification is reversible and can be controlled by selective removal of CO molecules using a STM tip. As shown in Figure 5.9 a) and c), a CO molecule is detached from its coordination site, by placing the STM tip over CO-Mn-TPTBP molecule and ramping the sample bias to 0.6 V with open feedback loop (Figure 5.9 b). In contrast with the sharp jump in the current signal for desorbing a CO molecule from a Mn phthalocyanine [165], no abrupt current change is observed except a visible deviation between the forward and backward curves in the bias range below 0.25 V in the process of removing the CO ligand from Mn-TPTBP. The resulting species recovers the usual shape and an asymmetric zero-bias peak characteristic for a bare Mn-TPTBP molecule (Figure 5.9 d).

To better understand the influence of CO ligand on the magnetic state of Mn-TPTBP molecules, we analyze the possible physical origin of the zero-bias anomaly of CO-Mn-TPTBP complexes by dI/dV spectra fitting in combination with the DFT calculated spin-dependent electronic structures of the Mn-TPTBP and CO-Mn-TPTBP complex in gas phase (DFT calculation is done by Dr. Shulai Lei).

5.6.2 Possible Physical Origin of the Zero-Bias Anomaly of CO Ligated Mn-TPTBP Molecule

As a strong ligand field, CO molecule has the π-acceptor character and affects the the spin state of Mn-TPTBP in two aspects: (i) it enhances the energy splitting of the d orbitals, and thus trigger low spin configuration in the complex [196]; (ii) it withdraws the electron density between Mn ion and Au surface and hence reduces the coupling of the Mn d orbitals to the substrate [169], [170]. The line shape of the zero-bias anomaly for the CO coordinated Mn-TPTBP molecules indicates that it is probably a convolution of Kondo resonances and IETS features (spin excitation or vibration).

Figure 5.10 a) depicts a typical dI/dV spectrum of CO ligated Mn-TPTBP molecules and its fitting with two Fano functions as:

$$\frac{dI}{dV} = A_{K1} \cdot \frac{(q_1 \cdot \Gamma_{K1}/2 + eV - E_{K1})^2}{(\Gamma_{K1}/2)^2 + (eV - E_{K1})^2} + A_{K2} \cdot \frac{(q_2 \cdot \Gamma_{K2}/2 + eV - E_{K2})^2}{(\Gamma_{K2}/2)^2 + (eV - E_{K2})^2} + c \tag{5.2}$$

The zero-bias anomaly can be properly fitted by a Fano peak and a dip in the bias range from -20 mV to +20 mV, giving rise to respective Kondo temperatures of 71.0 ± 17.0 K and 11.3 ± 7.1 K. This means two unpaired spins of the Mn ion are

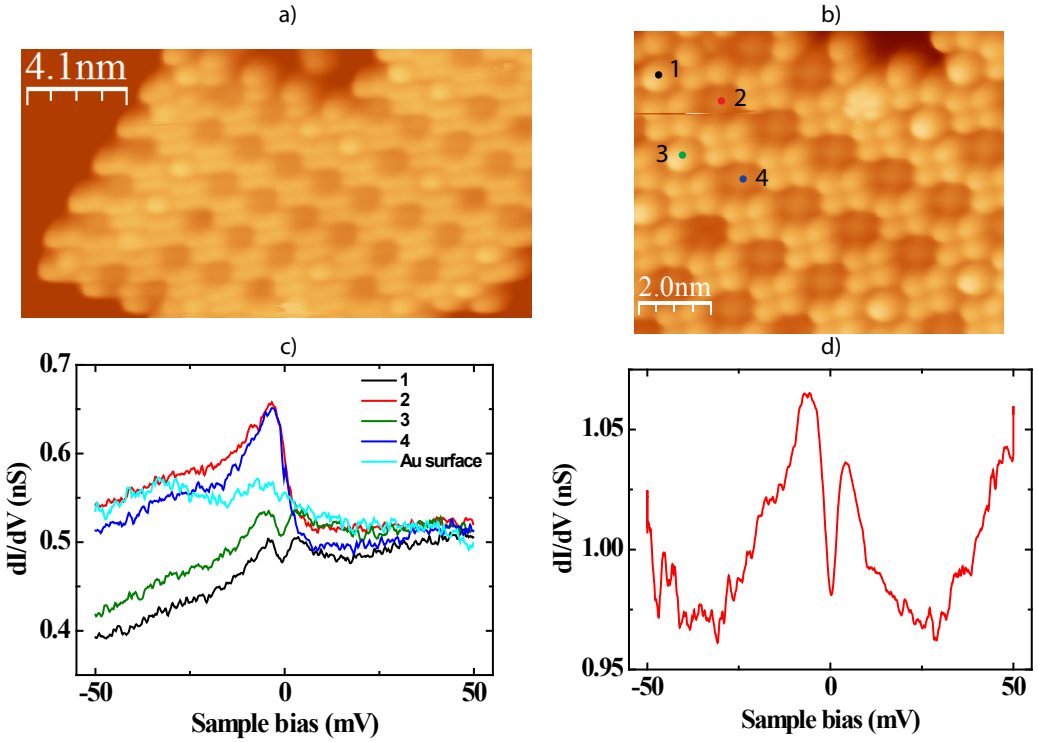

Figure 5.8: STM images and dI/dV spectra of Mn-TPTBP islands exposed to CO gas. **a)** Overview of a molecule island (V = 1.1 V, I = 30 pA). Some molecules show central protrusion rather than depression. **b)** High resolution image of the same island in **a)** (V = 1.1 V, I = 30 pA). **c)** dI/dV curves taken on CO coordinated or bare Mn-TPTBP molecules embedded in island (setpoint defined by V = 0.1 V, I = 0.5 nA). The sites for recording dI/dV spectra are marked by different color spots in **b)**. **d)** High resolution dI/dV spectrum of a CO-Mn-TPTBP molecule (setpoint defined by V = 50 mV, I = 0.5 nA). All the dI/dV spectra are taken with lock-in modulation of 0.91 mV.

separately scattered by the itinerant electrons of the substrate, which generate two Kondo resonances with different coupling strengths and thus distinguished Kondo temperatures. Actually, two Kondo channels for Fe phthalocyanine (Pc) molecules on Au(111) surface had been reported recently [195]. The dI/dV spectrum at bigger bias range (out of ±20 mV) does not match the fitting curve, suggesting some other contributions from the molecule for the differential conductance, which are not clear yet.

Another possible origin of the zero-bias anomaly in dI/dV spectra of CO-Mn-TPTBPs is the coexistence of Kondo scattering and inelastic tunneling. As one can see in Figure 5.10 b), the feature around E_F (from -20 mV to 20 mV) can also be well reproduced by a Fano function and two symmetric Fermi-Dirac step

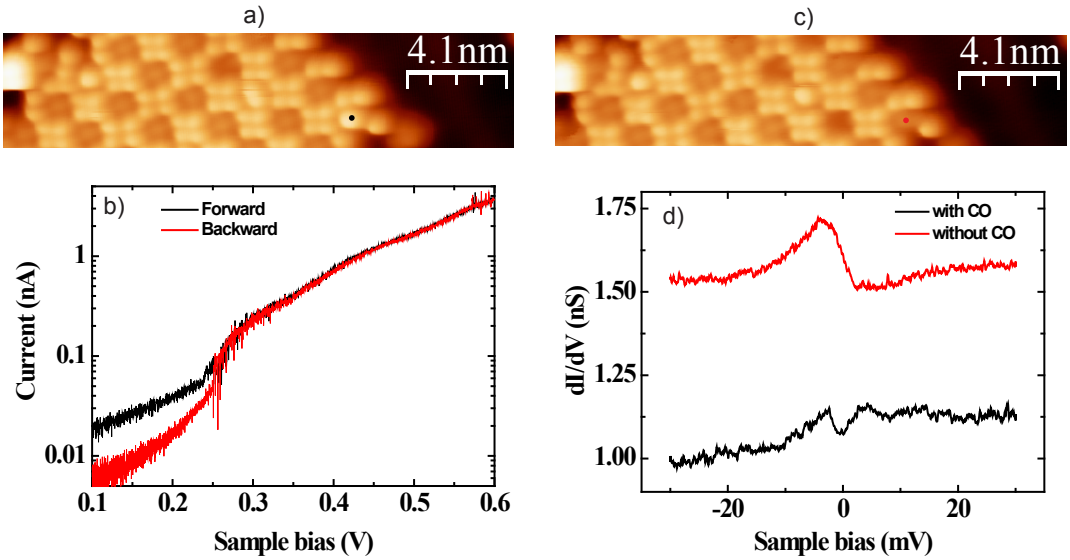

Figure 5.9: Desorption of CO ligand from CO coordinated Mn-TPTBP species. **a)** and **c)** are the STM image before and after detachment of the CO molecule (V = 1.0 V, I = 30 pA). The tip position is marked by a black and a red dot in **a)** and **c)**, respectively. **b)** Tunneling current during ramping the sample bias from 0.1 V to 0.6 V for removing the CO ligand (current is shown at a logarithmic scale to highlight the difference between forward and backward current). Setpoint is defined by V = 0.1 V, I = 20 pA. **d)** Corresponding dI/dV spectra of the CO coordinated or uncoordinated Mn-TPTBP molecule. Setpoint is defined by V= 30 mV, I = 0.5 nA, and lock-in modulation of 0.49 mV is used.

functions as:

$$\frac{dI}{dV} = A_K \cdot \frac{(q \cdot \Gamma_K/2 + eV - E_K)^2}{(\Gamma_K/2)^2 + (eV - E_K)^2} + A_s \cdot \left(\frac{1}{Exp((eV - E_s)/\Gamma_s) + 1} - \frac{1}{Exp((eV + E_s)/\Gamma_s) + 1}\right) + c \tag{5.3}$$

Here A_s, E_s and Γ_s are the amplitude, step energy and width of the Fermi-Dirac step function, respectively. The extracted Kondo width is 26.7 ± 4.5 mV corresponding to a Kondo temperature of 109.2 ± 18.4 K, and the symmetric steps are located at $\pm(1.7 \pm 0.4)$ meV with a characteristic width of 0.6 ± 0.2 meV. The step width is comparable to the thermal broadening $K_BT \approx 0.39$ meV in our measurement at $T = 4.5$ K. Recently, D. Jacob et al. studied the competition between quantum spin tunneling and Kondo screening for integer spin impurity (S = 1 and S = 2) on a surface and predicted that the Kondo peak can be splitted by quantum spin tunneling at zero magnetic field [197]. This physical scenario may be related to the case of CO-Mn-TPTBP complexes since their dI/dV spectra looks like a splitted Kondo peak.

Based on the line shape analysis of the zero-bias anomaly of CO-Mn-TPTBP complex, we study the change of electron occupation in $3d$ orbitals of Mn ion upon CO

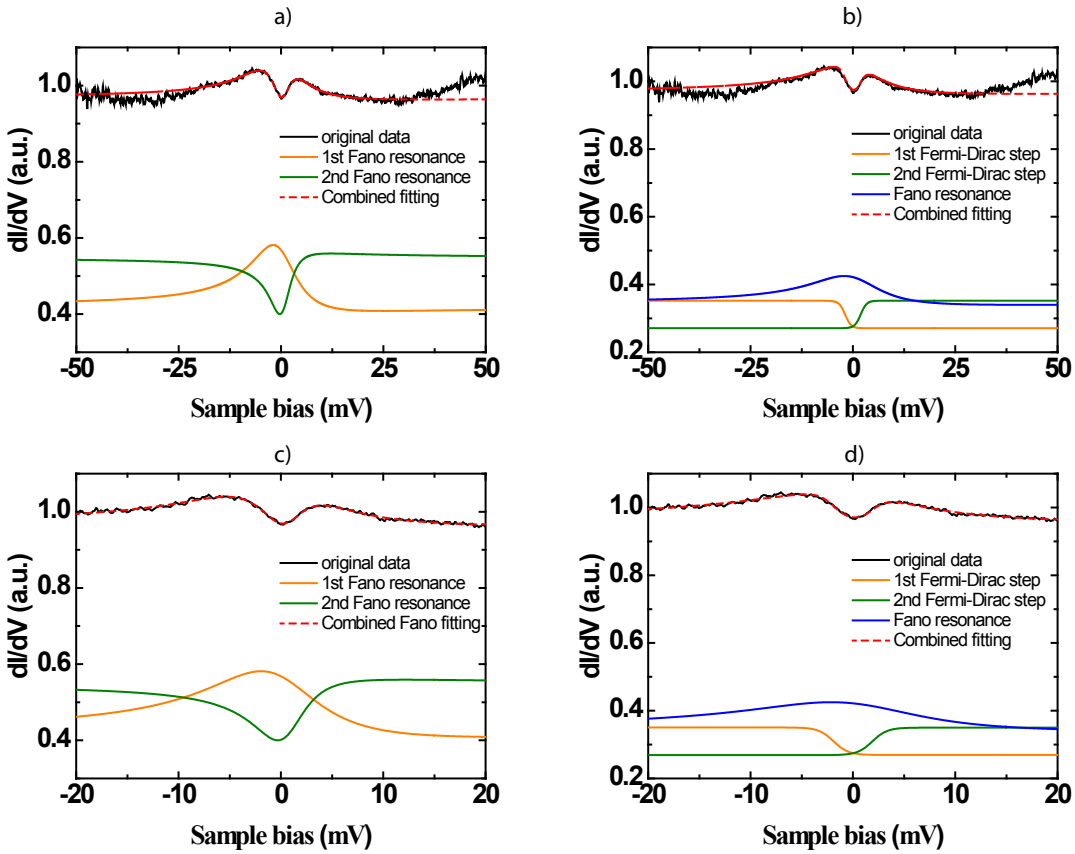

Figure 5.10: a) A typical dI/dV spectrum of a CO ligated Mn-TPTBP molecule with its fitting by two Fano functions. The values of the fitting parameters are as following: $q_1 = -6.0 \pm 2.3$, $\Gamma_{K1} = 17.3 \pm 4.1$ mV, $q_2 = 0.4 \pm 0.2$, $\Gamma_{K2} = 3.7 \pm 1.2$ mV. **b)** The same dI/dV spectrum as **a)** fitted by a Fano function and two symmetric Fermi-Dirac step functions. The values of the fitting parameters are as following: $q = -6.9 \pm 2.6$, $\Gamma_K = 26.7 \pm 4.5$ mV, $\Gamma_s = 0.6 \pm 0.2$ mV. **c)** and **d)** are the zoom-in graphs of **a)** and **b)** in the bias range from -20 mV to 20 mV, respectively. The fitting parameter values are averaged over four molecules, and the standard errors are calculated with the formula $\bar{\sigma} = \sqrt{\frac{1}{n-1}\sum_{n=1}^{n}(x_i - \bar{x})^2}$ with n the number of measurements and $\bar{x}$ the mean value of the measured parameters.

ligation by DFT calculation. The simulation method is the same as that elaborated in section 5.4.2 of this thesis.

Figure 5.11 a) shows the DFT simulated spin configuration of free Mn-TPTBP molecule. The Mn ion has a spin state of S = 5/2 due to five unpaired electrons in the manganese $3d$ sub-orbitals with degenerate d_{xz}/d_{yz}. The spin up states are mainly above the Fermi energy without occupation, while the spin down states are located below the Fermi energy and filled by electrons. Intense DOS peaks of these orbitals are predominantly lying at energies of > 2 V away from the E_F, with only a single peak of $d_{x^2-y^2}$ located at -0.2 V.

Figure 5.11 b) shows that the CO ligand coordinates perpendicularly to the molecular plane with a dihedral angle of 173°, which is similar to the configuration of CO ligated to metal-phthalocyanines adsorbed on surfaces [165], [167]. The relative height of the Mn ion with respect to the pyrrolic nitrogen atom plane is 0.15 Å, the same as that in Mn-TPTBP. However, it is expected that the Mn atom in the surface anchored Mn porphyrins would be lifted up from the surface by the oppositely coordinated axial ligand, which is know as *surface trans effect* [169], [170]. The CO molecule connects to the Mn ion via its carbon atom through a synergic π^* backbonding, which drastically alters the electron population and the spin of the Mn d orbitals. The d_{xz} and d_{yz} orbitals overlap each other, suggesting they are still degenerate upon the coordination of CO. This indicates that the upright configuration of CO maintains the 4-fold symmetry locally around the Mn ion [167]. The d_{xy} orbital has one branch lying above E_F and the other one staying below E_F, thus holding an unpaired spin. For the degenerate d_{xz}/d_{yz} orbitals, they have large spectral weight at about -0.77 V with same intensity of the two opposite spin orientations, indicating a fully occupied status with electrons. The d_{z^2} orbital has a spin up DOS peak and a spin down DOS peak lying around 1.3 V above E_F. These two peaks are equivalent and hence cancel the spin polarization in the d_{z^2} orbital. Likewise, the empty $d_{x^2-y^2}$ orbital lose its magnetic moment due to the identical DOS distribution of majority and minority spin with a peak located at 1.1 V and 2.9 V, respectively. The electron occupation of the $3d$ orbitals is well approximated as $(d_{xy})^1(d_{xz}/d_{yz})^2(d_{z^2})^1(d_{x^2-y^2})^1$ for Mn-TPTBP from the PDOS spectra, which is drastically changed into $(d_{xy})^1(d_{xz}/d_{yz})^4(d_{z^2})^0(d_{x^2-y^2})^0$ by the CO coordination. Therefore, the total spin S = 5/2 is reduced to S = 1/2 due to the impact induced by CO adduct (Figure 5.11 c).

The influence of CO coordination on the electron redistribution and spin polarization of Mn-TPTBP molecule can be understood via the hybridization of CO molecular orbitals (5σ and $2\pi^*$) with Mn $3d$ orbitals. Considering the symmetries of these orbitals, the d_{z^2} orbital is strongly hybridized with the 5σ orbital and the d_π orbitals are dominantly coupled with the $2\pi^*$ orbital (Figure 5.11 d). The bonding and antibonding state formed by d_{z^2} and 5σ is fully occupied and unoccupied, respectively. According to the relative energy levels of d_{z^2} and 5σ orbitals, the bonding state is dominated by the 5σ orbital while the antibonding state has a major weight from the d_{z^2} orbital. Therefore, the d_{z^2} orbital of CO-Mn-TPTBP molecule is emptied. However, the fully filled bonding state composed of d_π and $2\pi^*$ orbitals mainly exhibits the character of d_π orbitals, thus resulting into the occupation of d_π orbitals for CO-Mn-TPTBP. For the left two orbitals d_{xy} and $d_{x^2-y^2}$, they do not overlap with the CO molecular orbitals notably due to their arrangements in the xy plane and maintain their own energy levels and spatial distributions, namely nonbonding states. For CO ligand coordinated to metalloporphyrin, charge donation from metal ion to CO and vise versa charge backdonation from CO to the metal-organic molecule can usually happen. This charge donation and backdonation processes would induce charge redistribution in the CO ligated metalloporphyrins, but the charge balance between the CO ligand and the metalloporphyrins is often satisfied. In other words,

there is no obvious charge transfer between CO ligand and metal-organic molecules [166].

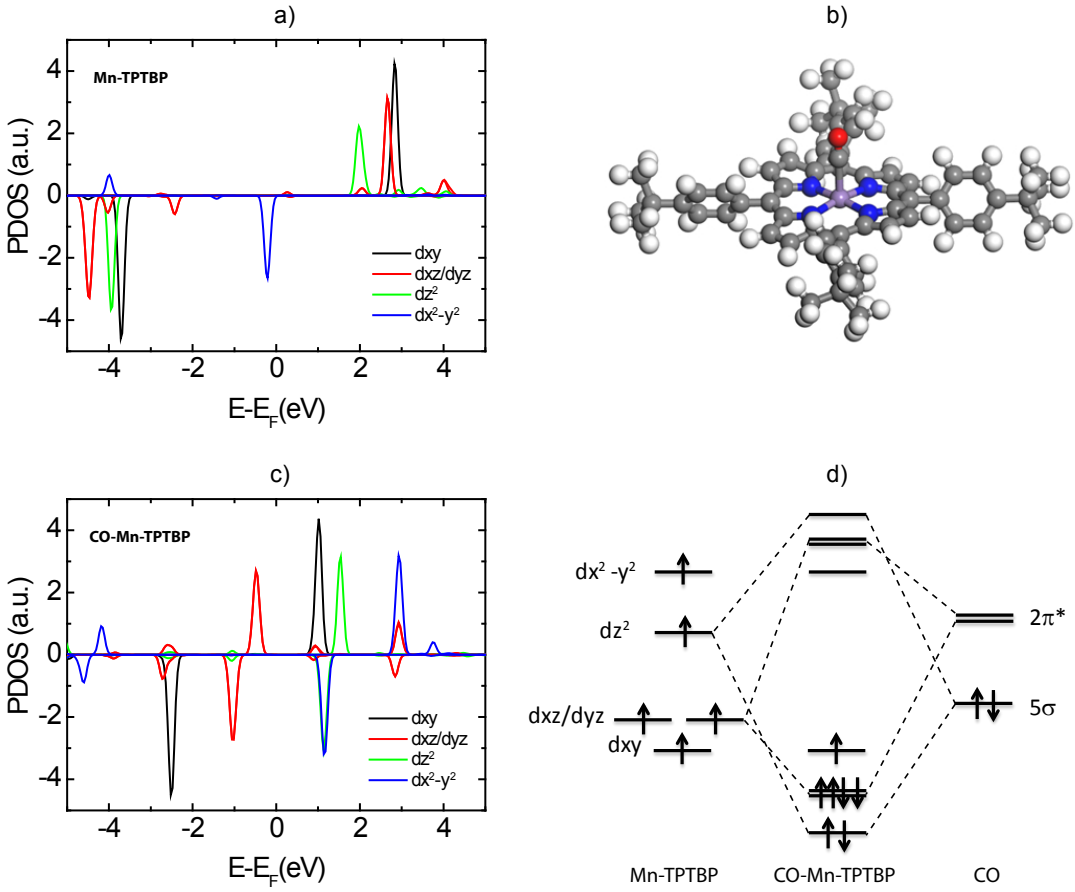

Figure 5.11: a) Projected density of state (PDOS) on $3d$ orbitals of Mn ion in Mn-TPTBP molecule. **b)** DFT optimized geometry of CO-Mn-TPTBP complex in gas phase. **c)** Projected density of state (PDOS) on $3d$ orbitals of Mn ion in CO-Mn-TPTBP complex. **d)** Molecular orbital (MO) diagram of CO-Mn-TPTBP complex.

5.6.3 Interpretation of the Zero-Bias Anomaly in dI/dV Spectra of CO-Mn-TPTBP Molecules

From the PDOS spectra of CO-Mn-TPTBP molecule provided by DFT calculation, it is possible to speculate about the physical mechanism from which the zero-bias anomaly in dI/dV spectra of CO-Mn-TPTBP originates. Firstly, this zero-bias anomaly is not likely to be a convolution of two Kondo resonances since there is only one single spin located in the d_{xy} orbital. Moreover, the idea that the zero-bias anomaly is a combination of a Kondo resonance and two symmetric inelastic tunneling steps also encounters a difficulty. Due to the total spin S = 1/2 of Mn ion in CO-Mn-TPTBP, spin excitation of Mn ion can be excluded and the possible inelastic

tunneling may only stem from hindered translation motion of the CO adduct [198]. The main problem for this explanation is that there is a higher Kondo temperature of CO-Mn-TPTBP complex than the bare Mn-TPTBP molecules, which contradicts with the general scenario that the central metal ion in metal-organic molecules is lifted up by the axial ligand away from the substrate and thus the ion-substrate hybridization is weakened [165], [199]. Therefore, the Kondo screening of the unpaired spin in d_{xy} of CO-Mn-TPTBP has to be considered.

As a similar metal tetrapyrrole macrocycle species, manganese phthalocyanine (MnPc) molecules on metal/semiconductor surfaces has been intensively studied in the past several years. Y. S. Fu et al. found the MnPc/Pb(111)/Si(111) system showing a Mn $3d_{xy}$ orbital derived Kondo resonance with a varied Kondo temperature ranging from 23 K to 419 K, depending on the thickness determined DOS of the underneath Pb thin film substrate [172]. For MnPc molecules adsorbed on Pb(111) single crystal surface, double Kondo spectral features originating from the independent screening of the two remaining localized spins in the d_{xy} and d_{π} orbitals had been discovered [173]. Moreover, respective research of spin control over MnPc with the binding of CO on Bi(110) and atomic H on Au(111) were carried out [165], [199]. For MnPc, Mn has two unpaired spins in d_{xy} and d_{z^2} orbitals on Bi(110) and three unpaired spins in d_{xy}, d_{xz}/d_{yz} and d_{z^2} orbitals on Au(111). The d_{z^2} orbital hybridizes with the $2\pi^*$ orbital of CO and s orbital of atomic H to reduce the net spin from 1 to 1/2 and from 3/2 to 1, respectively. Hence, both CO-MnPc and H-MnPc still has magnetic moment with nonzero spins, which is similar to our CO-Mn-TPTBP case. The broad dip feature in dI/dV spectra of CO ligated MnPc was recognized to be not a Kondo resonance but a mixed-valence state, due to the weak coupling of spin-active d_{xy} orbital to bismuth substrate [165]. Likewise, no dI/dV signal was detectable for H-MnPc on Au(111) surface at 0.4 K, indicating probably underscreened Kondo effect at very low energy scale or no Kondo screening between the d_{xy}, d_{xz}/d_{yz} orbitals and the Au surface [199]. Since in our case the hybridization of d_{xy} orbital with the substrate is unknown, we can only propose that the zero-bias anomaly of CO-Mn-TPTBP probably stem from a mixed-valence state with a vibronic feature of the molecule. Further investigation with external magnetic field and varied temperatures would be helpful to get a clearer picture for the magnetic properties of CO-Mn-TPTBP molecules on Au(111) substrate.

5.7 Conclusion

The Mn-TPTBP molecules self-assemble into densely packed islands consisting of units with two side lengths about 15 ± 1 Å and 18 ± 1 Å, respectively. Molecules have two separate orbital resonances located at sample biases of 1.1 V and 1.7 V, and also a small shoulder feature centered at 1.3 V. The dI/dV map at 1.1 V shows four lobes and a central depression for the molecular macrocycle, which changes into a clover shape with a protrusion on the Mn ion under 1.7 V. In comparison

with the electron distribution of molecular orbitals resolved by DFT calculation, the molecular resonances at 1.1 V and 1.7 V can be assigned to the LUMO+1 and LUMO+2 orbitals.

Differential conductance spectra of the Mn-TPTBP molecules show an asymmetric peak around E_F, which can be recognized as Kondo resonance with temperature-dependent measurement. This indicates that the Mn atom has a total spin S = 5/2 with a ground state of $S_z = |\pm 1/2\rangle$ and an easy-plane magnetic anisotropy. The Kondo effect of Mn-TPTBP molecules is mainly localized on the central Mn atom, implying a localized d orbital of Mn ion and no effective scattered polarized DOS on peripheral ligands.

By attachment of a carbon monoxide molecule on top of the Mn central atom in Mn-TPTBP molecule, the asymmetric Kondo peak changes into an asymmetric line shape composed of a dip on top of a peak. On the contrary, the original spin state of Mn ion can be recovered by detaching the CO ligand using the STM tip with certain sample biases (i.e. 0.6 V with a tip height defined by V = 0.1 V, I = 20 pA). Therefore, a reversible manipulation of the magnetic state of the Mn-TPTBP molecule is achieved.

Gas phase GGA+U calculations of Mn-TPTBP and CO-Mn-TPTBP complex suggest that the total spin S = 5/2 of Mn-TPTBP is reduced to S = 1/2 of CO ligated Mn-TPTBP. On the other hand, the asymmetric zero-bias anomaly of CO-Mn-TPTBP can be well reproduced by two Fano functions or one Fano function with two Fermi-Dirac step functions. From the spin state of Mn ion in CO coordinated Mn-TPTBP, it is not proper to relate this zero bias anomaly to two independent Kondo scattering events. And it should also not be attributed to be a convolution of a Kondo resonance and two symmetric steps originating from the vibration of CO ligand when considering the weakened molecule-substrate coupling induced by the CO ligand. Without knowing the hybridization between the singly occupied d_{xy} orbital and the metal surface, we can only speculate that the origin of the zero bias anomaly could be a combination of a mixed-valence state and a vibronic feature of the molecule. Nevertheless, more investigation for the complex line shape at E_F of CO coordinated Mn-TPTBP has to be conducted with external magnetic field and different temperatures for the sake of getting a better understanding of the experimental observations.

6 Summary

In this thesis, we investigate three kinds of metalloporphyrin molecules (Mn-TPyP, FeOEP-Cl and Mn-TPTBP) adsorbed on noble metal surfaces by low temperature STM/AFM methods. The structural, electronic, and magnetic properties of these metalloporphyrins at the organic/metal interfaces are mainly dealt with in our studies.

We studied the self-assembly, electronic structure and conformational change of Mn-TPyP molecules on Cu(111) surface. The molecules show adaption of their conformations and bonding in response to different annealing temperatures and coverages on the surface. Mn-TPyP molecules self-assemble into chains along the three-fold symmetric <110> direction on Cu(111), and also hexagonal rings are formed when the molecular chains in the three equivalent crystal orientations intersect. Dark molecules (with flat pyridine groups) and bright molecules (with tilted pyridine groups) are found on the Cu surface, and the appearance of bright molecules are triggered by temperature. For molecular chains, the neighboring dark molecules are mediated by four Cu adatoms but no Cu adatom sits between adjacent bright and dark molecules. While dark molecules show broad orbital features, bright molecules have three narrow orbital resonances, indicating a weaker coupling with the substrate. The pyridine rings of bright molecules and dark molecules coordinated to Cu adatoms can be rotated unidirectionally. The pyridine groups in the dark molecules uncoordinated with Cu adatoms show a reversible rotation behavior. This study shows the influences of temperature, molecular density, molecule-substrate interaction on molecular conformation and bonding in self-assemblies, and also demonstrates the role of local physiochemical environment on the molecular structures and functionalities, which is critical for the design and fabrication of molecular devices.

We also showed the force and conductance for the Au(111) surface supported FeOEP-Cl and FeOEP molecules contacted by different STM/AFM tips. Repulsive short-range forces are found between the Au tips and the FeOEP-Cl molecules in the contact regime, which pushes the Fe atom toward the Au surface and gives rise to an effective Kondo screening of the Fe atom by the substrate electrons. In the case of the FeOEP molecules contacted by a Cl-functionalized tip, repulsive forces between the Cl apex atom and the FeOEP also results in a Kondo peak in the dI/dV spectra, suggesting that the spin state (oxidation state) of FeOEPs is changed from S = 1 (+2) to S =5/2 (+3). By contacting the FeOEP molecules with a Au tip, the asymmetric dip shape in molecular dI/dV spectra are modified into spin excitation steps and then to a Kondo peak due to tip-molecule attraction and repulsion

respectively. The proximity of Xe-terminated tips also induce spin excitation but not Kondo effect for FeOEPs. The different responses for the magnetic properties of FeOEP to diverse tip apex atoms indicates the importance of their chemical identities for magnetic state manipulation. The building-up of tip-molecule contact with an oscillating STM/AFM tip provides a effective way to tune the properties of molecular magnets consecutively and allow the acquirement of force and (differential) conductance simultaneously. In addition, the high-resolution Δf images recorded by Xe and Cl functionalized tips confirm the chemical structure of iron tetrabenzoporphyrin, showing the capability of NC-AFM for identifying adsorbates on surfaces at a single-molecule level.

Furthermore, we demonstrated a reversible manipulation of the spin state in a Mn-TPTBP molecule on Au(111) surface by adsorption and desorption of a CO molecule. Mn-TPTBP molecules adsorbed on Au surface show an asymmetric Kondo peak around E_F with a high spin state of S = 5/2. However, the molecules coordinated by a single CO molecule show a novel line shape composed of a dip on top of a peak in the dI/dV spectra with a low spin state S = 1/2. We attribute the novel dI/dV spectrum of the CO-Mn-TPTBP complexes to be a probable combination of a mixed-valence state and a vibronic feature of the molecule. Further investigation of this molecular system with external magnetic field and varied temperatures is expected to get a clearer picture of the present scenario. This study probably proposes new physical mechanisms for the reversible spin state control of the metal-organic complexes by axial ligand coordination method.

The above studies not only reveal the fundamental properties of three metalloporphyrins on metal surfaces, but also explore their functionalities via conformational adaptation and magnetic state modification induced by tunneling electrons, tip-molecule interactions and chemical adduct adsorption. On one hand, it enhances the understanding of molecular adsorption and assembly behaviors on surfaces, which are valuable for the building of supramolecular architectures in future; On the other hand, the achievements of reversible changes of conformation and magnetic state for individual molecules in self-assembled structures provide possibilities for fabricating new devices of molecular electronics and spintronics.

Abbreviations

(LT-)STM: (low temperature) scanning tunneling microscopy

STS: scanning tunneling spectroscopy

DOS: density of state

differential conductance: dI/dV

IETS: inelastic electron tunneling spectroscopy

(nc-)AFM: (no-contact) atomic force microscopy

TF: tuning fork

Δf: frequency shift

Mn-TPyP: manganese-tetra-pyridine-porphyrin

FeOEP-(Cl): iron octaethylporphyrin (chloride)

Mn-TPTBP: manganese-tetra-phenyl-tert-butyl-porphyrin

vdW: van der Waals

CPD: contact potential difference

UHV: ultra high vacuum

PLL: phase locked loop

fcc: face centered cubic

RT: room temperature

CFT: crystal field theory

LFT: ligand field theory

ZFS: zero field splitting

$\boldsymbol{E_F}$: Fermi energy

ZBP: zero bias peak

$\boldsymbol{T_K}$: Kondo temperature

FWHM: full width at half maximum

CO: carbon monoxide

DFT: density functional theory

LDOS: local density of states

HOMO: highest occupied molecular orbital

LUMO: lowest unoccupied molecular orbital

Pc: phthalocyanine

PDOS: projected density of state

Bibliography

[1] Victor V Zhirnov, et al. Limits to Binary Switch Scaling-A Gedanken Model. *Proceedings of the IEEE*, 91(11):1934–1939, 2003.

[2] Richard P. Feynman. There's plenty of room at the bottom. *Engineering and science*, pages 22–36, 1960.

[3] Martin Fuechsle, et al. A single-atom transistor. *Nature Nanotechnology*, 7(4):242–246, 2012.

[4] Hyunwook Song, et al. Observation of molecular orbital gating. *Nature*, 462(7276):1039–1043, December 2009.

[5] Binning G., et al. Surface Studies by Scanning Tunneling Microscopy. *Physical Review Letters*, 49(1):57–61, 1982.

[6] G. Binnig and C. F. Quate. Atomic Force Microscope. *Physical Review Letters*, 56(9), 1986.

[7] M. F. Crommie, C. P. Lutz, and D. M. Eigler. Confinement of electrons to quantum corrals on a metal surface. *Science*, 262:218–20, October 1993.

[8] Alexander Ako Khajetoorians, et al. Atom-by-atom engineering and magnetometry of tailored nanomagnets. *Nature Physics*, 8(6):497–503, 2012.

[9] Sebastian Loth, et al. Bistability in atomic-scale antiferromagnets. *Science*, 335:196–9, January 2012.

[10] Kenjiro K. Gomes, et al. Designer Dirac fermions and topological phases in molecular graphene. *Nature*, 483:306–310, 2012.

[11] C. Rogero, et al. Resolution of site-specific bonding properties of C_{60} adsorbed on Au(111). *Journal of Chemical Physics*, 116(2):832–836, 2002.

[12] James a Theobald, et al. Controlling molecular deposition and layer structure with supramolecular surface assemblies. *Nature*, 424:1029–1031, 2003.

[13] Leonhard Grill, et al. Nano-architectures by covalent assembly of molecular building blocks. *Nature nanotechnology*, 2:687–91, November 2007.

[14] Nikolas A. A. Zwaneveld, et al. Organized formation of 2D extended covalent organic frameworks at surfaces. *Journal of the American Chemical Society*, 130(21):6678–6679, 2008.

[15] U. Schlickum, et al. Metal-Organic Honeycomb Nanomeshes with Tunable Cavity Size. *Nano Letters*, 7(12):3813–3817, 2007.

[16] Pietro Gambardella, et al. Supramolecular control of the magnetic anisotropy in two-dimensional high-spin Fe arrays at a metal interface. *Nature materials*, 8:189–193, March 2009.

[17] T. R. Umbach, et al. Ferromagnetic coupling of mononuclear Fe centers in a self-assembled metal-organic network on Au(111). *Physical Review Letters*, 109:267207, 2012.

[18] L. Lafferentz, et al. Controlling on-surface polymerization by hierarchical and substrate-directed growth. *Nature Chemistry*, 4(3):215–220, 2012.

[19] Felix Hanke and Jonas Björk. Structure and local reactivity of the Au(111) surface reconstruction. *Physical review B*, 87:235422, 2013.

[20] Hisao Ishii, et al. Energy level alignment and interfacial electronic structures at organic/metal and organic/organic interfaces. *Advanced Materials*, 11(8):605–625, 1999.

[21] Yusuke Tanaka, et al. Role of interfacial dipole layer for energy-level alignment at organic/metal interfaces. *Organic Electronics: physics, materials, applications*, 10:990–993, 2009.

[22] Isabel Fernández Torrente, Katharina J Franke, and Jose Ignacio Pascual. Single Molecules: the Role of Screening on Energy Level Alignment. *Journal of Physics: Condensed Matter*, 20:184001, 2008.

[23] Franz J. Giessibl. Advances in atomic force microscopy. *Reviews of Modern Physics*, 75(3):949–983, 2003.

[24] Leo Gross, et al. The chemical structure of a molecule resolved by atomic force microscopy. *Science*, 325:1110, August 2009.

[25] Niko Pavliček, et al. Atomic Force Microscopy Reveals Bistable Configurations of Dibenzo[a,h]thianthrene and their Interconversion Pathway. *Physical Review Letters*, 108(8):086101, February 2012.

[26] John T. Groves. The bioinorganic chemistry of iron in oxygenases and supramolecular assemblies. *Proceedings of the National Academy of Sciences of the United States of America*, 100(7):3569–3574, 2003.

[27] Gérard Simonneaux, et al. Asymmetric heterogeneous catalysis by metalloporphyrins. *Coordination Chemistry Reviews*, 250:2212–2221, 2006.

[28] Willi Auwärter, et al. Site-specific electronic and geometric interface structure of Co-tetraphenyl-porphyrin layers on Ag(111). *Physical Review B*, 81:245403, June 2010.

[29] Sergey A. Krasnikov, et al. Formation of Extended Covalently Bonded Ni Porphyrin Networks on the Au(111) Surface. *Nano Research*, 4(4):376–384, 2011.

[30] Francesca Moresco, et al. Conformational Changes of Single Molecules Induced by Scanning Tunneling Microscopy Manipulation: A Route to Molecular Switching. *Physical Review Letters*, 86(4):672–675, January 2001.

[31] H. Wende, et al. Substrate-induced magnetic ordering and switching of iron porphyrin molecules. *Nature materials*, 6:516–520, July 2007.

[32] B. W. Heinrich, et al. Protection of excited spin states by a superconducting energy gap. *Nat. Phys.*, 9:765–768, 2013.

[33] Christian F. Hermanns, et al. Huge magnetically coupled orbital moments of Co porphyrin molecules and their control by CO adsorption. *Physical Review B*, 88(10):104420, 2013.

[34] Christian Wäckerlin, et al. Controlling spins in adsorbed molecules by a chemical switch. *Nature communications*, 1:61, January 2010.

[35] G. Binnig, et al. Tunneling through a controllable vacuum gap. *Applied Physics Letters*, 40(2):178–180, 1982.

[36] G Binnig, et al. Atomic Resolution with Atomic Force Microscope. *Europhysics Letters (EPL)*, 3(12):1281–1286, 1987.

[37] Franz J. Giessibl. Atomic Resolution of the Silicon (111)-(7 x 7) Surface by Atomic Force Microscopy. *Science*, 267:68, 1995.

[38] Hal Edwards, et al. Fast, high-resolution atomic force microscopy using a quartz tuning fork as actuator and sensor. *Journal of Applied Physics*, 82(3):980, 1997.

[39] Franz J. Giessibl. Atomic resolution on Si(111)-(7 x 7) by noncontact atomic force microscopy with a force sensor based on a quartz tuning fork. *Applied Physics Letters*, 76(11):1470, 2000.

[40] G. Binnig and D. P. E. Smith. Single-tube three-dimensional scanner for scanning tunneling microscopy. *Review of Scientific Instruments*, 57(8):1688–1689, 1986.

[41] Tobias R. Umbach. *Magnetic and Electronic Properties of Supramolecular Architectures on Metal Surfaces*. PhD thesis, Freie universität Berlin, 2013.

[42] Isabel Fernández Torrente. *Local Spectroscopy of bi-molecular assemblies: screening, charge transfer, and magnetism at the molecular scale*. PhD thesis, Freie universität Berlin, 2008.

[43] J. Tersoff and D. R. Hamann. Theory and Application for the Scanning Tunneling Microscope. *Physical Review Letters*, 50(25):1998–2001, 1983.

[44] J. Bardeen. Tunnelling from a many-particle point of view. *Physical Review Letters*, 6(2):57–59, 1961.

[45] A. Selloni, et al. Voltage-dependent scanning-tunneling microscopy of a crystal surface: Graphite. *Physical Review B*, 31(4):2602–2605, 1985.

[46] N. D. Lang. Spectroscopy of single atoms in the scanning tunneling microscope. *Phys. Rev. B*, 34(8):5947–5950, 1986.

[47] Lucia Vitali, et al. Portrait of the potential barrier at metal-organic nanocontacts. *Nature materials*, 9(4):320–323, 2010.

[48] R. M. Feenstra. Tunneling spectroscopy of the (110)surface of direct-gap III-V semiconductors. *Phys. Rev. B*, 50(7):4561–4570, 1994.

[49] C. Wagner, R. Franke, and T. Fritz. Evaluation of I(V) curves in scanning tunneling spectroscopy of organic nanolayers. *Physical Review B*, 75:235432, 2007.

[50] M. Ziegler, et al. Local density of states from constant-current tunneling spectra. *Physical Review B*, 80:125402, 2009.

[51] B. C. Stipe. Single-Molecule Vibrational Spectroscopy and Microscopy. *Science*, 280(5370):1732–1735, June 1998.

[52] Shaowei Li, et al. Rotational and Vibrational Excitations of a Hydrogen Molecule Trapped within a Nanocavity of Tunable Dimension. *Physical Review Letters*, 111(14):146102, October 2013.

[53] A. J. Heinrich, et al. Single-atom spin-flip spectroscopy. *Science*, 306:466–469, October 2004.

[54] J. I. Pascual. Single molecule vibrationally mediated chemistry: Towards state-specific strategies for molecular handling. *European Physical Journal D*, 35(2):1–14, 2005.

[55] Katharina J Franke and Jose Ignacio Pascual. Effects of electron–vibration coupling in transport through single molecules. *Journal of Physics: Condensed Matter*, 24:394002, 2012.

[56] James G. Kushmerick, et al. Vibronic Contributions to Charge Transport Across Molecular Junctions. *Nano Letters*, 4(4):639–642, 2004.

[57] Jean-Pierre Gauyacq, Nicolás Lorente, and Frederico Dutilh Novaes. Excitation of local magnetic moments by tunneling electrons. *Progress in Surface Science*, 87:63–107, May 2012.

[58] Sebastian Loth, et al. Measurement of fast electron spin relaxation times with atomic resolution. *Science*, 329(5999):1628–1630, 2010.

[59] Y. Martin, C. C. Williams, and H. K. Wickramasinghe. Atomic force microscope-force mapping and profiling on a sub 100-Å scale. *Journal of Applied Physics*, 61(10):4723–4729, 1987.

[60] T. R. Albrecht, et al. Frequency modulation detection using high-Q cantilevers for enhanced force microscope sensitivity. *Journal of Applied Physics*, 69(2):668–673, 1991.

[61] Christian Lotze. *Fundamental Processes in Single Molecule Junctions : Interplay of Forces and Electronic Effects*. PhD thesis, Freie universität Berlin, 2013.

[62] Andre Schirmeisen, Boris Anczykowski, and Harald Fuchs. Dynamic modes of atomic force microscopy. *Nanotribology and Nanomechanics (Second Edition): An Introduction*, pages 235–277, 2008.

[63] Franz Giessibl. Forces and frequency shifts in atomic-resolution dynamic-force microscopy. *Physical Review B*, 56(24):16010–16015, 1997.

[64] John E. Sader and Suzanne P. Jarvis. Accurate formulas for interaction force and energy in frequency modulation force spectroscopy. *Applied Physics Letters*, 84(10):1801, 2004.

[65] J. E. Jones. On the Determination of Molecular Fields. II. From the Equation of State of a Gas. *Proceedings of the Royal Society A: Mathematical, Physical and Engineering Sciences*, 106:463–477, 1924.

[66] H.C. Hamaker. The london-van der Waals attraction between spherical particles. *Physica*, 4(10):1058–1072, 1937.

[67] Zhixiang Sun, et al. Quantitative Atomic Force Microscopy with Carbon Monoxide Terminated Tips. *Physical Review Letters*, 106:046104, January 2011.

[68] Fabian Mohn, et al. Imaging the charge distribution within a single molecule. *Nature Nanotechnology*, 7(4):227–231, February 2012.

[69] F. J. Giessibl. Theory for an electrostatic imaging mechanism allowing atomic resolution of ionic crystals by atomic force microscopy. *Physical Review B*, 45(23):13815–13818, 1992.

[70] Maximilian Schneiderbauer, et al. CO Tip Functionalization Inverts Atomic Force Microscopy Contrast via Short-Range Electrostatic Forces. *Physical Review Letters*, 112(16):166102, 2014.

[71] G. Meyer. A simple low-temperature ultrahigh-vacuum scanning tunneling microscope capable of atomic manipulation. *Review of Scientific Instruments*, 67(8):2960–2965, 1996.

[72] K. Besocke. An easily operable scanning tunneling microscope. *Surface Science Letters*, 181:145–153, 1987.

[73] J. Frohn, et al. Coarse tip distance adjustment and positioner for a scanning tunneling microscope. *Review of Scientific Instruments*, 60(6):1200–1201, 1989.

[74] I. Horcas, et al. WSXM: A software for scanning probe microscopy and a tool for nanotechnology. *Review of Scientific Instruments*, 78:013705, 2007.

[75] Michael Ruby. http://spectrafox.com/.

[76] Robin Ohmann, et al. Influence of subsurface layers on the adsorption of large organic molecules on close-packed metal surfaces. *ACS Nano*, 5(2):1360–1365, 2011.

[77] J. V. Barth, et al. Scanning tunneling microscopy observation on the reconstructed Au(111) surface: Atomic structure, long-range superstructure, rotational domains, and surface defects. *Phys. Rev. B*, 42(15), 1990.

[78] W. Chen, et al. Scanning Tunneling Microscopy Observation of an Electronic Superlattice at the Surface of Clean Gold. *Physical Review Letters*, 80(7):1469–1472, 1998.

[79] M. J. Comstock, et al. Manipulation of azobenzene molecules on Au(111) using scanning tunneling microscopy. *Physical Review B - Condensed Matter and Materials Physics*, 72(15):153414, 2005.

[80] W. H. Soe, et al. Direct observation of molecular orbitals of pentacene physisorbed on Au(111) by scanning tunneling microscope. *Physical Review Letters*, 102:176102, 2009.

[81] Federico J Williams, et al. First observation of capping/uncapping by a ligand of a Zn porphyrin adsorbed on Ag(100). *Chemical communications (Cambridge, England)*, 44(15):1688–1689, 2004.

[82] Burema Shiri R., et al. Probing Nitrosyl Ligation of Surface-Confined Metalloporphyrins by Inelastic Electron Tunneling Spectroscopy. *ACS nano*, 7(6):5273–5281, 2013.

[83] M E Kosal and K S Suslick. Microporous porphyrin and metalloporphyrin materials. *Journal of Solid State Chemistry*, 152(1):87–98, 2000.

[84] Johannes V Barth, Giovanni Costantini, and Klaus Kern. Engineering atomic and molecular nanostructures at surfaces. *Nature*, 437(7059):671, September 2005.

[85] M. Abel, et al. Designing a New Two-Dimensional Molecular Layout by Hydrogen Bonding. *ChemPhysChem*, 7:82–85, 2006.

[86] Alexander Weber-Bargioni, et al. Visualizing the frontier orbitals of a conformationally adapted metalloporphyrin. *ChemPhysChem*, 9:89–94, January 2008.

[87] Knud Seufert, et al. Cis-dicarbonyl binding at cobalt and iron porphyrins with saddle-shape conformation. *Nature chemistry*, 3:114, February 2011.

[88] Thorsten Wölfle, Andreas Görling, and Wolfgang Hieringer. Conformational flexibility of metalloporphyrins studied by density-functional calculations. *Physical Chemistry Chemical Physics*, 10:5739–5742, October 2008.

[89] Ch. Loppacher, et al. Direct Determination of the Energy Required to Operate a Single Molecule Switch. *Physical Review Letters*, 90(6):066107, February 2003.

[90] X. H. Qiu, G. V. Nazin, and W. Ho. Mechanisms of Reversible Conformational Transitions in a Single Molecule. *Physical Review Letters*, 93(19):196806, November 2004.

[91] Willi Auwärter, et al. Porphyrins at interfaces. *Nature chemistry*, 7:105–120, 2015.

[92] A. H. Morrish. *The Physical Principles of Magnetism*. John Wiley & Sons, Inc., 1966.

[93] W. Robert Scheidt and Christopher A. Reed. Spin-State/Stereochemical Relationships in Iron Porphyrins: Implications for the Hemoproteins. *Chem. Rev.*, 81:543–555, 1981.

[94] Cyrus F. Hirjibehedin, et al. Large magnetic anisotropy of a single atomic spin embedded in a surface molecular network. *Science*, 317(5842):1199, August 2007.

[95] A. F. Otte, et al. Spin Excitations of a Kondo-Screened Atom Coupled to a Second Magnetic Atom. *Physical Review Letters*, 103(10):107203, September 2009.

[96] Noriyuki Tsukahara, et al. Adsorption-Induced Switching of Magnetic Anisotropy in a Single Iron(II) Phthalocyanine Molecule on an Oxidized Cu(110) Surface. *Physical Review Letters*, 102(16):167203, April 2009.

[97] Dante Gatteschi, Roberta Sessoli, and Jacques Villain. *Molecular Nanomagnets*. Oxford university press, 2006.

[98] D. Dai, H. Xiang, and M. H. Whangbo. Effects of Spin-Orbit Coupling on Magnetic Properties of Discrete and Extended Magnetic Systems. *Journal of computational chemistry*, 29(13):2187–2209, 2008.

[99] W. J. DE Haas, J. de Boer, and G. J. Van dën Berg. The electrical resistance of gold, copper and lead at low temperatures. *Physica*, 1(7-12):1115–1124, 1934.

[100] M. P. Sarachik, E. Corenzwit, and L. D. Longinotti. Resistivity of Mo-Nb and Mo-Re alloys containing 1% Fe. *Physical Review*, 135(4A):A1041, 1964.

[101] J. Kondo. Effect of ordinary scattering on exchange scattering from magnetic impurity in metals. *Physical Review*, 169(2):437–440, 1968.

[102] Markus Ternes, Andreas J Heinrich, and Wolf-Dieter Schneider. Spectroscopic manifestations of the Kondo effect on single adatoms. *Journal of Physics: Condensed Matter*, 21:053001, 2009.

[103] D. Goldhaber-Gordon, et al. From the Kondo Regime to the Mixed-Valence Regime in a Single-Electron Transistor. *Physical Review Letters*, 81(23):5225, 1998.

[104] A. C. Hewson. *The Kondo Problem to Heavy Fermions*. Cambridge University Press, 1997.

[105] J. R. Schrieffer and P. A. Wolff. Relation between the Anderson and Kondo Hamiltonians. *Physical review*, 149(2):491–492, 1966.

[106] W. G. van der Wiel, et al. The Kondo Effect in the Unitary Limit. *Science*, 289:2105, 2000.

[107] V. Madhavan. Tunneling into a Single Magnetic Atom: Spectroscopic Evidence of the Kondo Resonance. *Science*, 280(5363):567–569, April 1998.

[108] Jiutao Li, et al. Kondo Scattering Observed at a Single Magnetic Impurity. *Physical Review Letters*, 80(13):2893–2896, March 1998.

[109] U. Fano. Effects of Configuration Interaction on Intensities and Phase Shifts. *Physical review*, 124(6):1866, 1961.

[110] K. Nagaoka, et al. Temperature Dependence of a Single Kondo Impurity. *Physical Review Letters*, 88(7):077205, February 2002.

[111] T Yokoyama, et al. Selective assembly on a surface of supramolecular aggregates with controlled size and shape. *Nature*, 413(6856):619–621, 2001.

[112] Nikolai Wintjes, et al. A supramolecular multiposition rotary device. *Angewandte Chemie - International Edition*, 46(22):4089–4092, 2007.

[113] David Ecija, et al. Hierarchic Self-Assembly of Nanoporous Chiral Networks with Conformationally Flexible Porphyrins. *ACS nano*, 4(8):4936–4942, 2010.

[114] Daniel Heim, et al. Surface-assisted assembly of discrete porphyrin-based cyclic supramolecules. *Nano Letters*, 10(1):122–128, 2010.

[115] Daniel Heim, et al. Self-Assembly of Flexible One-Dimensional Coordination Polymers on Metal Surfaces. *Journal of the American Chemical Society*, 132:6783–6790, 2010.

[116] Yang Li, et al. Coordination and Metalation Bifunctionality of Cu with 5, 10, 15, 20- Tetra (4-pyridyl) porphyrin : Toward a Mixed-Valence Two- Dimensional Coordination Network. *Journal of the American Chemical Society*, 134:6401–6408, 2012.

[117] W Auwärter, et al. Self-assembly and conformation of tetrapyridyl-porphyrin molecules on Ag(111). *The Journal of chemical physics*, 124(19):194708, May 2006.

[118] Willi Auwärter, et al. Conformational Adaptation and Selective Adatom Capturing of Tetrapyridyl-porphyrin Molecules on a Copper (111) Surface. *Journal of the American Chemical Society*, 129:11279–11285, 2007.

[119] Willi Auwärter, et al. Controlled metalation of self-assembled porphyrin nanoarrays in two dimensions. *ChemPhysChem*, 8:250–254, February 2007.

[120] Violeta Iancu, Aparna Deshpande, and Saw-wai Hla. Manipulating Kondo Temperature via Single Molecule Switching. *Nano letters*, 6(4):820–823, 2006.

[121] Jens Brede, et al. Adsorption and conformation of porphyrins on metallic surfaces. *Journal of Vacuum Science and Technology B: Microelectronics and Nanometer Structures*, 27(2):799, 2009.

[122] Stefanie Ditze, et al. On the Energetics of Conformational Switching of Molecules at and Close to Room Temperature. *Journal of the American Chemical Society*, 2014.

[123] F Klappenberger, et al. Temperature dependence of conformation, chemical state, and metal-directed assembly of tetrapyridyl-porphyrin on Cu(111). *The Journal of chemical physics*, 129(21):214702, December 2008.

[124] L. Bartels, G. Meyer, and K.-H. Rieder. Controlled vertical manipulation of single CO molecules with the scanning tunneling microscope: A route to chemical contrast. *Applied Physics Letters*, 71(2):213, 1997.

[125] Martina Corso, et al. Charge Redistribution and Transport in Molecular Contacts. *Physical Review Letters*, 115:136101, 2015.

[126] Ziliang Shi, et al. Thermodynamics and selectivity of two-dimensional metallosupramolecular self-assembly resolved at molecular scale. *Journal of the American Chemical Society*, 133(16):6150–6153, 2011.

[127] T. R. Umbach, et al. Site-specific bonding of copper adatoms to pyridine end groups mediating the formation of two-dimensional coordination networks on metal surfaces. *Physical Review B*, 89:235409, 2014.

[128] Sylvain Clair, et al. Mesoscopic metallosupramolecular texturing by hierarchic assembly. *Angewandte Chemie - International Edition*, 44:7294–7297, 2005.

[129] Sylvain Clair, et al. Monitoring two-dimensional coordination reactions: Directed assembly of Co - Terephthalate nanosystems on Au(111). *Journal of Physical Chemistry B*, 110(11):5627–5632, 2006.

[130] Sebastain Stepanow, et al. Surface-assisted assembly of 2D metal-organic networks that exhibit unusual threefold coordination symmetry. *Angewandte Chemie - International Edition*, 46(5):710–713, 2007.

[131] N. Henningsen, et al. Site-dependent coordination bonding in self-assembled metal-organic networks. *Journal of Physical Chemistry Letters*, 2:55–61, 2011.

[132] Thomas Classen, et al. Hydrogen and coordination bonding supramolecular structures of trimesic acid on Cu(110). *Journal of Physical Chemistry A*, 111(49):12589–12603, 2007.

[133] Zechao Yang, et al. Orbital Redistribution in Molecular Nanostructures Mediated by Metal-Organic Bonds. *ACS nano*, 8(10):10715–10722, 2014.

[134] Thomas Classen, et al. Templated growth of metal-organic coordination chains at surfaces. *Angewandte Chemie (International ed. in English)*, 44:6142, September 2005.

[135] Sam Haq, et al. Clean coupling of unfunctionalized porphyrins at surfaces to give highly oriented organometallic oligomers. *Journal of the American Chemical Society*, 133(31):12031–12039, August 2011.

[136] S. L. Tait, et al. One-Dimensional Self-Assembled Molecular Chains on Cu(100): Interplay between Surface-Assisted Coordination Chemistry and Substrate Commensurability. *Journal of Physical Chemistry C*, 111(29):10982–10987, July 2007.

[137] Leo Gross, et al. Measuring the charge state of an adatom with noncontact atomic force microscopy. *Science*, 324(5933):1428–1431, June 2009.

[138] N. Henningsen, et al. Trans to cis isomerization of an azobenzene derivative on a Cu(100) surface. *Applied Physics A*, 93(2):241–246, August 2008.

[139] J. I. Pascual, et al. Selectivity in vibrationally mediated single-molecule chemistry. *Nature*, 423(6939):525–528, 2003.

[140] J.-G. Lee, J. Ahner, and J. T. Yates. The adsorption conformation of chemisorbed pyridine on the Cu(110) surface. *The Journal of Chemical Physics*, 114(3):1414, 2001.

[141] H Lesnard, N Lorente, and M-L Bocquet. Theoretical study of benzene and pyridine STM-induced reactions on copper surfaces. *Journal of Physics: Condensed Matter*, 20(22):224012, 2008.

[142] M Lastapis, et al. Picometer-scale electronic control of molecular dynamics inside a single molecule. *Science*, 308:1000, May 2005.

[143] Francesca Matino, et al. Single azopyridine-substituted porphyrin molecules for configurational and electronic switching. *Chemical communications (Cambridge, England)*, 46(36):6780–6782, 2010.

[144] Tao Lin, et al. Two-Dimensional Lattice of Out-of- Plane Dinuclear Iron Centers Exhibiting Kondo Resonance. *ACS nano*, 8(8):8310–8316, 2014.

[145] Weihua Wang, et al. Intramolecularly resolved Kondo resonance of high-spin Fe (II) -porphyrin adsorbed on Au(111). *Physical Review B*, 91:045440, 2015.

[146] Saranyan Vijayaraghavan, et al. Restoring the Co Magnetic Moments at Interfacial Co-Porphyrin Arrays by Site-Selective Uptake of Iron. *ACS nano*, 9(4):3605–3616, 2015.

[147] Shin-Ichi Ohkoshi, et al. Light-induced spin-crossover magnet. *Nature chemistry*, 3(7):564–569, July 2011.

[148] K. Tarafder, et al. Pressure and Temperature Control of Spin-Switchable Metal-Organic Coordination Polymers from Ab Initio Calculations. *Physical Review Letters*, 109(7):077203, August 2012.

[149] Md. Ehesan Ali, Biplab Sanyal, and Peter M. Oppeneer. Tuning the Magnetic Interaction between Manganese Porphyrins and Ferromagnetic Co Substrate through Dedicated Control of the Adsorption. *The Journal of Physical Chemistry C*, 113(32):14381–14383, August 2009.

[150] Benjamin W. Heinrich, et al. Tuning the Magnetic Anisotropy of Single Molecules. *Nano Letters*, 15:4024–4028, 2015.

[151] Markus Ternes, et al. Interplay of Conductance, Force, and Structural Change in Metallic Point Contacts. *Physical Review Letters*, 106(1):016802, January 2011.

[152] Benjamin W. Heinrich, et al. Change of the magnetic coupling of a metal-organic complex with the substrate by a stepwise ligand reaction. *Nano letters*, 13:4840–4843, October 2013.

[153] Dimas G. de Oteyza. Direct Imaging of Covalent Bond Structure in Single-Molecule Chemical reactions. *Science*, 340:1434–1437, 2013.

[154] Thiruvancheril G. Gopakumar, et al. Transfer of Cl ligands between adsorbed iron tetraphenylporphyrin molecules. *Journal of the American Chemical Society*, 134(29):11844–11847, 2012.

[155] Olof Peters. *Environmental Influences on the Magnetic Properties of Metal-Organic Complexes*. Master thesis, Freie universität Berlin, 2014.

[156] L. Gao, et al. Site-Specific Kondo Effect at Ambient Temperatures in Iron-Based Molecules. *Physical Review Letters*, 99(10):106402, September 2007.

[157] Noriyuki Tsukahara, et al. Evolution of Kondo Resonance from a Single Impurity Molecule to the Two-Dimensional Lattice. *Physical Review Letters*, 106(18):187201, May 2011.

[158] M. Bernien, et al. Fe-porphyrin monolayers on ferromagnetic substrates: Electronic structure and magnetic coupling strength. *Physical Review B*, 76(21):214406, December 2007.

[159] R. Žitko, R. Peters, and Th. Pruschke. Properties of anisotropic magnetic impurities on surfaces. *Physical Review B*, 78:224404, 2008.

[160] John E. Sader and Yoshiaki Sugimoto. Accurate formula for conversion of tunneling current in dynamic atomic force spectroscopy. *Applied Physics Letters*, 97(4):043502, 2010.

[161] N. Néel, et al. Controlled Contact to a C_{60} Molecule. *Physical Review Letters*, 98(6):065502, February 2007.

[162] N Néel, et al. Conductance of single atoms and molecules studied with a scanning tunnelling microscope. *Nanotechnology*, 18(4):044027, January 2007.

[163] Nadine Hauptmann, et al. Force and conductance during contact formation to a C_{60} molecule. *New Journal of Physics*, 14:073032, 2012.

[164] Fabian Mohn, et al. Different tips for high-resolution atomic force microscopy and scanning tunneling microscopy of single molecules. *Applied Physics Letters*, 102(7):073109, 2013.

[165] A. Stróecka, et al. Reversible Change of the Spin State in a Manganese Phthalocyanine by Coordination of CO Molecule. *Physical Review Letters*, 109:147202, 2012.

[166] Howon Kim, et al. Switching and Sensing Spin States of Co-Porphyrin in Bimolecular Reactions on Au(111) Using Scanning Tunneling Microscopy. (10):9312–9317, 2013.

[167] Noriyuki Tsukahara, et al. Controlling orbital-selective Kondo effects in a single molecule through coordination chemistry. *The Journal of chemical physics*, 141(5):054702, August 2014.

[168] Christian Wäckerlin, et al. Ammonia coordination introducing a magnetic moment in an on-surface low-spin porphyrin. *Angewandte Chemie (International ed. in English)*, 52(17):4568–4571, April 2013.

[169] Ken Flechtner, et al. NO-Induced Reversible Switching of the Electronic Interaction between a Porphyrin-Coordinated Cobalt Ion and a Silver Surface. *Journal of the American Chemical Society*, 129:12110–12111, 2007.

[170] Wolfgang Hieringer, et al. The Surface Trans Effect : Influence of Axial Ligands on the Surface Chemical Bonds of Adsorbed Metalloporphyrins. *Journal of the American Chemical Society*, 133:6206–6222, 2011.

[171] Violeta Iancu, Aparna Deshpande, and Saw-Wai Hla. Manipulation of the Kondo Effect via Two-Dimensional Molecular Assembly. *Physical Review Letters*, 97(26):266603, December 2006.

[172] Ying-Shuang Fu, et al. Manipulating the Kondo Resonance through Quantum Size Effects. *Physical Review Letters*, 99(25):256601, December 2007.

[173] K. J. Franke, G. Schulze, and J. I. Pascual. Competition of superconducting phenomena and Kondo screening at the nanoscale. *Science*, 332:940, May 2011.

[174] Emi Minamitani, et al. Symmetry-Driven Novel Kondo Effect in a Molecule. *Physical Review Letters*, 109(8):086602, August 2012.

[175] L. J. Boucher. Manganese Porphyrin Complexes. III. Spectroscopy of Chloroaquo Complexes of Several Porphyrins. *Journal of the American Chemical Society*, 92(9):2725–2730, 1970.

[176] Kevin Leung, et al. Density functional theory and DFT+U study of transition metal porphines adsorbed on Au(111) surfaces and effects of applied electric fields. *Journal of the American Chemical Society*, 128:3659–3668, March 2006.

[177] Seth C. Hunter, Andrey A. Podlesnyak, and Zi Ling Xue. Magnetic excitations in metalloporphyrins by inelastic neutron scattering: Determination of zero-field splittings in iron, manganese, and chromium complexes. *Inorganic Chemistry*, 53(4):1955–1961, 2014.

[178] Howon Kim, et al. Mapping the electronic structures of a metalloporphyrin molecule on Au(111) by scanning tunneling microscopy and spectroscopy. *Physical Review B*, 80(24):245402, December 2009.

[179] G. Kresse. Efficient iterative schemes for ab initio total-energy calculations using a plane-wave basis set. *Physical Review B*, 54(16):11169–11186, 1996.

[180] G. Kresse and J. Furthmüller. Efficiency of ab-initio total energy calculations for metals and semiconductors using a plane-wave basis set. *Computational Materials Science*, 6(1):15–50, 1996.

[181] P. E. Blöchl. Projector augmented-wave method. *Physical Review B*, 50(24):17953–17979, 1994.

[182] G. Kresse. From ultrasoft pseudopotentials to the projector augmented-wave method. *Physical Review B*, 59(3):1758–1775, 1999.

[183] John P. Perdew, et al. Generalized Gradient Approximation Made Simple. *Physical Review Letters*, 77(18):3865–3868, 1996.

[184] Christian Wäckerlin, et al. On-surface coordination chemistry of planar molecular spin systems: novel magnetochemical effects induced by axial ligands. *Chemical Science*, 3(11):3154, 2012.

[185] Takashi Yokoyama, et al. Nonplanar adsorption and orientational ordering of porphyrin molecules on Au(111). *The Journal of Chemical Physics*, 115(8):3814, 2001.

[186] J. B. Neaton, Mark S. Hybertsen, and Steven G. Louie. Renormalization of molecular electronic levels at metal-molecule interfaces. *Physical Review Letters*, 97(21):216405, 2006.

[187] Barbara Gonzalez, et al. Manganese(II) Porphyrins. Synthesis, Structure, and Preference for Five-Coordination. *Journal of the American Chemical Society*, 97(11):3247–3249, 1975.

[188] John F. Kirner, Christopher A. Reed, and W. Robert Scheidt. Stereochemistry of Manganese Porphyrins. 2. *Journal of the American Chemical Society*, 99(4):1093–1101, 1977.

[189] Meng-sheng Liao and Steve Scheiner. Electronic structure and bonding in metal phthalocyanines, metal = Fe, Co, Ni, Cu, Zn. *Chemical Physics*, 114:9780–9791, 2001.

[190] U. G. E. Perera, et al. Spatially Extended Kondo State in Magnetic Molecules Induced by Interfacial Charge Transfer. *Physical Review Letters*, 105(10):106601, September 2010.

[191] Alexander F. Otte, et al. The role of magnetic anisotropy in the Kondo effect. *Nature Physics*, 4(11):847–850, September 2008.

[192] Q Dubout, et al. Controlling the Spin of Co Atoms on Pt(111) by Hydrogen Adsorption. *Physical Review Letters*, 114:106807, 2015.

[193] Qing Li, et al. Initial Adsorption and Kondo Resonance of 5,10,15,20-Tetrakis(4-bromophenyl)porphyrin–Co Molecules on Ag/Si(111) Surface Studied by Low-Temperature Scanning Tunneling Microscopy/Spectroscopy. *Japanese Journal of Applied Physics*, 48(8):08JB01, August 2009.

[194] J. J. Parks, et al. Mechanical Control of Spin States in Spin-1 Molecules and the Underscreened Kondo Effect. *Science*, 328:1370–1373, 2010.

[195] Emi Minamitani, et al. Symmetry-Driven Novel Kondo Effect in a Molecule. *Physical Review Letters*, 109(8):1–5, August 2012.

[196] Cristina Isvoranu, et al. Comparison of the carbonyl and nitrosyl complexes formed by adsorption of CO and NO on monolayers of iron phthalocyanine on Au(111). *Journal of Physical Chemistry C*, 115(50):24718–24727, 2011.

[197] D. Jacob and J. Fernández-Rossier. Competition between quantum spin tunneling and Kondo effect. *arXiv*, 1507(08474v2), 2015.

[198] Chi-lun Chiang, et al. Real-space imaging of molecular structure and chemical bonding by single-molecule inelastic tunneling probe. *Science*, 344(6186):885–888, 2014.

[199] Liwei Liu, et al. Reversible single spin control of individual magnetic molecule by hydrogen atom adsorption. *Scientific reports*, 3(111):1210, January 2013.

Acknowledgments

First of all, I would like to thank Prof. Dr. Katharina J. Franke for giving me the opportunity of my PhD study in her group. She gave me a lot of help and support on both physics and life in the last four years .

I also thank Prof. Dr. Stephanie Reich for supervising this thesis as the second referee.

I want to express my special gratitude to Prof. Dr. José I. Pascual for his help on my study.

A lot of thanks go to Prof. Dr. Constantin Czekelius in Heinrich-Heine-Universität Düsseldorf for providing the two manganese porphyrins inverstigated in this thesis.

I also want to thank Dr. Shulai Lei and Prof. Dr. Beate Paulus from Institut für Chemie und Biochemie in Freie Universität Berlin. They carried out the DFT calculation presented in this thesis.

I feel very grateful to Dr. Christian Lotze, who gave a direct supervision for my experiments and taught me the measurement skills hand by hand, also helped me out of many difficulties in my research. My thanks also go to the AFM members, Nils Krane and Fabian Schulz for their honest help. I appreciate the beneficial discussions with Dr. Benjamin W. Heinrich, Olof Peters, Michael Ruby, Paul Stoll, Nino Hatter and Gelavizh Ahmadi in my study. I also want to thank my chinese colleagues Jingcheng Li, Zechao Yang and Bo Chen, who are always pleased to chat with. I thank all the present and former members in AG Franke and AG Pascual for the great working atmosphere and good memories of the cakes and barbeques, parties, group excursions and ....

In particular, I want to express my great gratitude to my wife Ming Song and my lovely daughter Yuexi Chen, who inspire me a lot and bring me endless happiness. My parents and sister spare no effort to give me their support all the time, and my parents-in-law provide their largest passion and patience for taking care of my young family. The continuous support and understanding from my family members accompany me going through the whole study in Berlin. I applaud for all the care and love I get from my family and I feel very proud of them.

The financial support from the Chinese Scholarship Council (CSC) is gratefully acknowledged.

List of Publications

Xianwen Chen, Christian Lotze, Katharina J. Franke
Reversible Conformational Switching in Manganese-tetra-pyridine-Porphyrin Molecules on Cu(111) Surface
in preparation

Xianwen Chen, Christian Lotze, Katharina J. Franke
Reversible Change of the Spin State in a Manganese-tetra-phenyl-tert-butyl-Porphyrin by Coordination of CO Molecule on Au(111) Surface
in preparation

Contributions to Conferences

2013 Oral Contribution:
Workshop of the SFB 658-Integrated Research Training Group in Zeuthen, 16.05 - 17.05.2013
Reversible conformational switching in manganese porphyrin molecules

Poster:
DPG-Frühjahrstagung der Sektion Kondensierte Materie (SKM) in Dresden 30.03. - 04.04.2014
Reversible conformational switching in manganese-tetra-pyridine-porphyrin molecules

Selbständigkeitserklärung

Ich erkläre, dass ich die vorliegende Arbeit selbständig und nur unter Verwendung der angegebenen Literatur und Hilfsmittel angefertigt habe. Diese Arbeit ist nicht schon einmal in einem früheren promotionsverfahren angenommen oder als ungenügend beurteilt worden.

Own Work Declaration

Hereby I declare to have made this thesis on my own only by use of the denoted literature and resources. Contents taken over from external sources, directly or indirectly, are denoted as such. This dissertation has not been accepted or rejected as insufficient within the context of previous doctoral studies.

Berlin, 08. October 2015